University of Alberta

Metallic thin films for NEMS/MEMS: from fundamental behaviour to microstructural design and fabrication

by

Erik Luber

A thesis submitted to the Faculty of Graduate Studies and Research
in partial fulfillment of the requirements for the degree of

Doctor of Philosophy

in

Materials Engineering

Chemical and Materials Engineering

Fall 2011
Edmonton, Alberta

This thesis is dedicated to
My loving parents, Ansgard and Jürgen

Abstract

The main focus of this thesis is the study of thin metal films in microelectromechanical/nanoelectromechanical systems (MEMS/NEMS), ranging from application to fundamental behaviour. The use of metallic structural components is desirable since they are electrically conductive, optically reflective and ductile. However, polycrystalline metallic thin films typically exhibit low strength and hardness, high surface roughness and significant incremental stress, making them unusable for NEMS/MEMS. By co-sputtering Ni-Mo thin films we are able to tailor the microstructure and surface morphology such that these limitations are overcome. As such, uncurled NEMS cantilevers possessing enhanced hardness, metallic conductivity and sub-nanometer roughness are fabricated with resonant frequencies in the MHz regime, and quality factors ranging from 200-900. Following this, the use and design of all-metal atomic force microscope (AFM) probes is investigated. This is motivated by the growing number of AFM applications which make use of metal-coated probes, and as a result of the metallization suffers from stress-induced cantilever bending, thermal expansion mismatch, increased tip radius and limited device lifetime due to coating wear. To this end, monostructural all-metal AFM probes hav-

ing 1 µm thickness, lengths of 100-400 µm, and tip radii ranging from 10 to 40 nm are fabricated. This is accomplished through microstructural design of Cu-Hf thin films, where an optimal combination of resistivity (96 µΩcm), hardness (5.2 GPa), ductility and incremental stress.

Lastly, in many MEMS/NEMS applications the unique properties of non-metallic components are required, but a metallization layer is still needed. As metallization layers become increasingly thinner, film stability can become problematic, due to the phenomenon of solid-state dewetting. The fundamental mechanisms of solid-state dewetting are investigated in Ni thin films on SiO_2. This phenomenon is monitored *in situ* using time resolved differential reflectometry (TRDR) and *ex situ* using AFM. It is found that Ni dewetting on SiO_2 occurs through the sequential processes of grain growth, grain boundary grooving, hole growth and particle coarsening. Kinetic analysis of the TRDR data revealed two rate-limiting processes, with activation energies of 0.31 ± 0.04 and 0.59 ± 0.06 eV. It is hypothesized that these kinetic pathways correspond to Ni grain growth and surface mass self-diffusion on the Ni(111) planes, respectively.

Preface

This thesis is organized into 5 chapters. Chapter 1 introduces the important concepts used in this thesis. Chapter 2 describes how to tailor the microstructure and morphology of thin metal films for NEMS/MEMS applications, where NEMS cantilevers are fabricated from Ni-Mo thin films. Chapter 3 pertains to the development and design of Cu-Hf thin films for all-metal AFM probes. Chapter 4 investigates the fundamental mechanisms of solid-state dewetting in Ni thin films on SiO_2. Finally, chapter 5 summarizes the main conclusions of this thesis.

Acknowledgements

Firstly, I would like to thank my supervisor Dave Mitlin for giving me the freedom and resources that most graduate students could only dream of. However, I am most grateful for your infinite enthusiasm and excitement for research, it is what brought me here and what kept me here for so long. I also have to acknowledge every member of Mitlin Group, it is awesome to work in a true team environment where everyone helps everyone else on their projects. In particular I have to mention my two partners in crime, Colin Ophus and Brian Olsen. Colin, aside from the hundreds of hours I have enjoyed solving your fun math problems and having endless scientific discussions, I am most appreciative of your truly genuine and contagious love of Science. Brian, first I must thank you for keeping the lab together and running, you are the glue. Secondly, for the countless hours we have spent discussing everything under the sun, you always present a fresh and different perspective.

Without the continued training and support from the staff at the University of Alberta Nanofab this thesis would not have been possible. Thank you Ken Westra, Keith Franklin, Stephanie Bozic, Les Showalter, Scott Munro and Jolene Chorzempa. I would also like to acknowledge the generous financial support of Alberta Ingenuity and NSERC during the course of my graduate studies.

Although my long list of collaborators are all greatly appreciated, I must make a special mention of Velimir 'Mimo' Radmilovic. You are a role model for what a scientist should be, your faith in my abilities and support inspire me to do better. Also, I am greatly in debt to Dr. Brett; when I don't know what to do or where to go with my life/career you are always seem to know the answers. Thanks for always

looking out for me and pointing me in the right direction.

I must also acknowledge the support of my friends. The other two members of L^3, Luc Gervais and Lee Fischer; you guys made my first few years of graduate studies some of the most memorable and enjoyable times of my life. Andrew Murray, thanks for always being there for me no matter what and turning 2 a.m. nanofab sessions into a good time. Nemanja Danilovic, for being the best material science roommate ever and housing my sister for so long. Lastly, my best friend Patrick Chan, you make me a better person.

This thesis would not exist without the love and support of my family. Thank you Mom and Pop for teaching me the value of hard work and making my childhood a place of adventure, discovery and wonder. My sister and best friend Christina, for thinking the world of me and making the planet earth a more exciting and interesting place. Lastly, my fiance Kelli Hewins, you are the most loving, caring and supportive partner anyone could ever hope for. I am lucky to have you in my life.

Contents

List of Figures

List of Tables

List of Symbols

Symbol	Meaning [units]	Symbol	Meaning [units]
D	Diffusivity [m^2/s]	λ	Wavelength [m]
δ	Dilation factor	η	Transmissivity
E	Young's modulus [Pa]	μ	Chemical potential [J/mol]
ΔE	Activation energy [eV]	M	Biaxial modulus [Pa]
ϵ	Strain	$\dot{N}$	Nucleation Rate
f	frequency [1/s]	σ	Stress [Pa]
ΔG	Gibbs energy [J/mol]	Ω	Atomic volume [m^3]
γ	Surface free energy density [J/m^2]	ρ	Resistivity [Ω m]
h	Thickness [m]		Molar density [mol/m^3]
k	Spring constant [N/m]	P	Pressure [Pa]
k_B	Boltzmann constant [J/K]	S	Structure factor
κ	Curvature [1/m]	R	Reflectivity
κ_T	Compressibility [m^2/N]	T	Temperature [K]

List of Abbreviations

Abbreviation	Meaning
AFM	Atomic force microscopy
CVD	Chemical vapour deposition
DC	Direct current
EDX	Energy-dispersive x-ray spectroscopy
EELS	Electron-energy loss spectroscopy
FDTD	Finite-difference time-domain simulation
FIB	Focused ion beam
GISAXS	Grazing incidence small angle X-ray scattering
HRTEM	High resolution transmission electron microscopy
IBAD	Ion beam assissted deposition
IC	Integrated circuit
KMC	Kinetic monte carlo simulation
MEMS	Microelectromechanical system
MOSS	Multi-beam optical stress sensor
NEMS	Nanoelectromechanical system
PMMA	Poly(methyl methacrylate)
PVD	Physical vapour deposition
RMS	Root mean square
SEM	Scanning electron microscopy
SPM	Scanning probe microscopy
TEM	Transmission electron microscopy
TRDR	Time-resolved differential reflectivity
XRD	X-ray diffraction

1

Introduction

1.1 MEMS/NEMS: A Materials Perspective

Microelectromechanical/nanoelectromechanical systems, or MEMS/NEMS, are ubiquitous; they are becoming increasingly incorporated in aspects of modern life, ranging from products such as automobile airbag systems, display systems, inkjet cartridges, to video game controllers. More generally, MEMS/NEMS characterize systems in which a micro/nano-scale mechanical structure is either acted upon by an external force which is transduced into an electrical signal by a specific method, or in which the structure itself generates a mechanical force to perform work.

Most structural MEMS/NEMS components are usually fabricated from silicon

based compounds such as silicon nitride, silicon carbide and silicon oxide, with silicon being by far the most widely used [1]. The dominance of silicon in MEMS/NEMS directly mirrors the use of silicon as the primary substrate material in integrated circuitry (IC). Perhaps the leading contributor to the growth of silicon MEMS/NEMS is the success of the IC industry itself, which provides a variety of well-developed fabrication methods that can be directly applied to mechanical structures. Moreover, silicon is an excellent structural material [2]. Silicon is both elastically stiff and very hard, but perhaps most importantly is the ability to produce silicon of amazing purity (99.999999999% pure) [3] in large, flawless single crystals.

Despite the almost ubiquitous use of Si in MEMS/NEMS and ICs, most applications require some form of metallization. These metallization layers are typically used in order to provide either/or high electrical conductivity and optical reflectivity. Metallization can however critically effect device performance, where concerns such as electromigration, thermal expansion mismatch, stress, inter-diffusion and dewetting must be addressed. Moreover, the use of metals in NEMS/MEMS can significantly change the mechanical properties and performance of the device. To this end, the primary focus of this thesis is to investigate fundamental material properties, structure and behaviour of various types of metallic thin films, with regard to their application in MEMS/NEMS devices.

1.2 Metallic Thin Film Deposition Methods

Metallic thin films can be deposited by a variety of techniques, with physical vapour deposition (PVD) and chemical vapour deposition (CVD) being the most common methods. In these vapour deposition methods, the film is grown by the condensation of metal atoms onto a substrate. In PVD the vapour is created by a physical process, whereas in CVD the film deposition is a product of a chemical reaction that occurs at the film surface. Many different PVD and CVD techniques exist, each of which have unique deposition environ-

ments (energies, pressure, deposition rate, flux distribution etc.), which can consequently be used to produce a variety of different film microstructures. The purpose of this section is to outline some of the most commonly used deposition techniques for thin metal films.

1.2.1 Evaporation

Shown in figure 1.1 is a simplified schematic of an evaporative deposition system. In this process sufficient thermal energy is provided to the source material such that atoms are evaporated (or sublimated) and condense on the substrate. Heating of the source material can be achieved via resistive heating of a wire, or resistive heating of a high melting point crucible containing the source, or induction heating or by an electron beam.

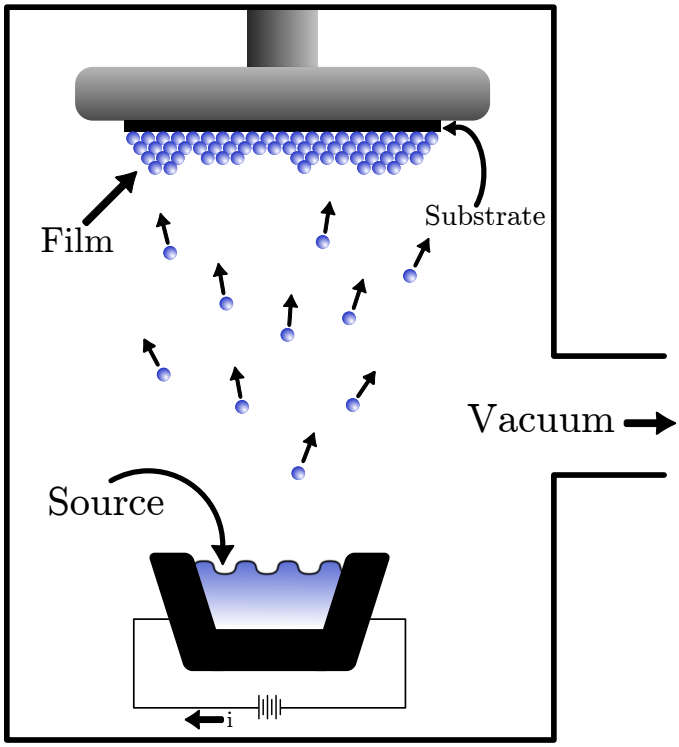

Figure 1.1: Schematic of an evaporative deposition system.

Evaporation rates (or vapour pressure) vary significantly depending on the

source material used [4], due to an exponential dependence of vapour pressure on the heat of sublimation. This limits the class of metals that can be practically evaporated, as extremely high temperatures are required for most refractory metals and other high melting point materials in order to reach a sufficiently high vapour pressure ($\sim$ 10 mtorr) necessary for appreciable deposition rates.

1.2.2 Sputtering

All films prepared in this thesis are deposited using DC-magnetron co-sputtering, therefore a more detailed discussion of sputtering is provided. Shown in figure 1.2 is a schematic of a DC sputtering system. Despite the extremely complex physics of sputtering it is a conceptually simple process, the basic principle behind sputtering is demonstrated in figure 1.3. A low-pressure, non reactive gas (typically argon), is flooded into a vacuum chamber with the target and substrate, a plasma is initiated by applying a large voltage across the substrate (anode) and target (cathode). The positive ions are then accelerated towards the negatively charged cathode, these ions then collide with the surface, which results in the release of secondary electrons. The secondary electrons are then accelerated to the positively charged anode, as they are travelling towards the anode they can collide with neutral argon atoms. If the energy transfer of the collision is less than the ionization potential of argon, the argon will excited to a higher energy state. Eventually the argon will decay back to it's ground state releasing the energy in the form of photons, which produces the characteristic glow discharge seen in sputtering. If the energy transfer is sufficient, the argon will become ionized and accelerated towards the target, releasing more secondary electrons. This avalanche process results in the formation of a stable plasma and acceleration of energetic ions towards the target which gives rise to the process of sputtering.

When the energetic ions strikes the target surface, several things can happen. At low incident ion energies ($\lesssim$ 10 eV) the ion may simply bounce off the target

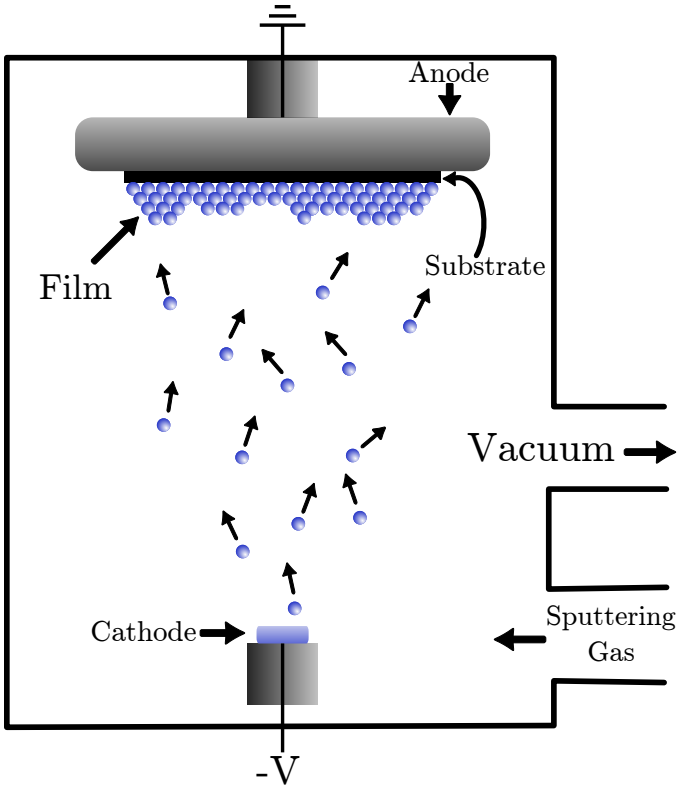

Figure 1.2: Schematic of a DC sputtering deposition system.

surface, or adsorb onto the surface giving off it's energy as heat. At higher energies there is physical rearrangement of the target, which typically occurs within the first few atomic layer of the surface. This results in a collisional cascade of atoms and eventual ejection of atoms from the surface (see figure 1.3). It is these ejected or sputtered atoms that impinge upon the substrate and grow the film.

Sputtering did not achieve widespread commercial use until it became magnetically assisted. By placing strong bar magnets underneath the guns the sputter rates were greatly increased. This process, called magnetron sputtering was one of the first practical applications of the magnetic confinement of electrons. In a the presence of a magnetic field, electrons will spiral around the magnetic field lines. By placing the bar magnets in a configuration in such a way that the magnetic field lines form closed loops within the vicinity of the target, the

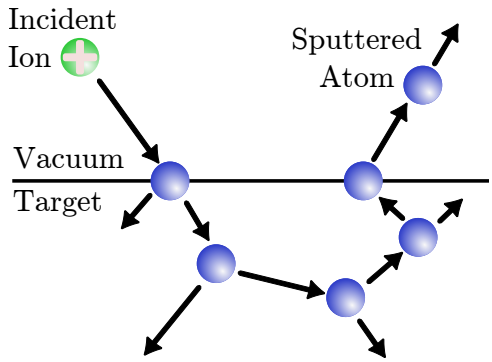

Figure 1.3: Illustration of basic sputtering principle. Energetic ions bombard the target surface which results in the ejection atoms from the target surface. These sputtered atoms are then subsequently deposited on the substrate surface.

secondary electrons become trapped in the magnetic field lines. This increases the probability of argon-electron collisions and hence the degree of ionization, which in turn increases the rate of ion bombardment rate, leading to higher deposition rates.

1.2.3 Chemical Vapour Deposition

Although there are a great number of CVD techniques (atmospheric–pressure CVD, low pressure CVD, laser-enhanced CVD, and plasma enhanced CVD), the fundamental steps that occur in all of them is illustrated in figure 1.4. In general, these steps include (1) gas phase reaction of the precursor gas(es), (2) transport of reactant(s) to substrate, (3) surface reaction(s) producing atomic metal species and reactant gas phase products, (4) nucleation of metal phase and (5) desorption of gas phase products.

One of the primary uses for CVD of metals is the ability to produce conformal coatings, unlike sputtering and evaporation. However, process development for depositing specific metals can be quite difficult, due to the often very large number of complex chemical pathways required for film deposition. Moreover, adjusting the film microstructure and morphology can challenging, due to the

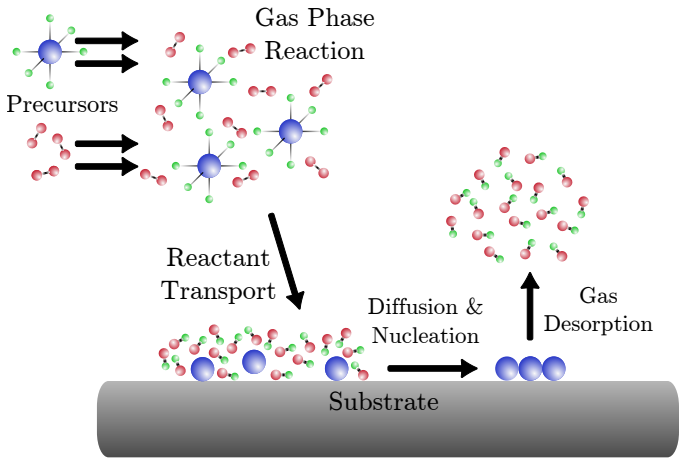

Figure 1.4: Schematic illustration the fundamental processes that occur during CVD film growth.

thermodynamic restrictions of the chemical reactions.

1.3 Atomistic Description of Film Growth

The purpose of this section is to provide a general overview of some of the most important atomic processes that occur during film growth. The extent of these processes will generally determine the structure and properties of the final film. As such, understanding how these processes are influenced by deposition parameters is of vital importance when engineering metal thin films.

1.3.1 Vapour Condensation

Before discussing the processes that occur during film growth, the necessary conditions for film growth to occur should first be established. Given a substrate at temperature T_s, exposed to a gas at temperature T_v, atoms in the vapour phase will collide with the substrate, with a certain fraction sticking to the substrate via physisorption or chemical bonds. These attached atoms are referred to as adatoms. However, given sufficient thermal energy some of these

adatoms will break the chemical bonds at the surface and evaporate. Therefore, for the growth front to advance the condensation rate must be larger than the evaporation rate. In this way the vapour must be supersaturated with respect to the substrate at temperature T_s.

For a homogeneous metal in contact with its own vapour at pressure P_v, there is a free energy difference of

$$\Delta G = k_\mathrm{B} T \ln(P_\mathrm{v}/P_\mathrm{eq}) \tag{1.3.1}$$

where P_eq is the equilibrium pressure of the vapour and k_B is the Boltzmann constant. Therefore if the vapour is supersaturated ($P_\mathrm{v} > P_\mathrm{eq}$) with respect to the substrate a net amount of material is continuously deposited. During actual thin film deposition the situation is somewhat more complicated, since the vapour and the substrate are most often different materials and at different temperatures. In this non-equilibrium situation P_eq is not well defined. Nonetheless the substrate is generally at a lower temperature than the vapour, which provides an additional driving force for film growth.

1.3.2 Adatom Transport

As atoms impinge and on the growth surface they are believed to quickly thermalize to the substrate temperature T_s, where they reside in equilibrium positions. Atoms can hop between equilibrium sites, but must overcome some energy barrier (or activation energy) ΔE_d for surface diffusion, where the hopping rate is [5],

$$w = v_0 \exp(-\Delta E_d / k_\mathrm{B} T_s) \tag{1.3.2}$$

where v_0 is on the order of the Debye frequency ($\sim 10^{13} - 10^{14}$ Hz). As such, surface diffusion rates are higher at elevated substrate temperatures. Bulk diffusion and intermixing with the substrate can also occur but only play a role at elevated temperatures, because the activation energy is typically much larger ($\sim 1 - 10$ eV) than surface diffusion ($\sim 0.1 - 1$ eV).

Most substrates will have some amount of defects, such as steps, grain boundaries and dislocation line terminations. These defects typically have a larger E_d than other defect-free surface sites, resulting in a much lower hopping rate away from these sites, and act as heterogeneous nucleation sites. If the average distance between defect sites in on the order of the diffusion length (which depends on temperature, deposition rate and material constants) the nucleation is heterogeneous. Conversely, if the diffusion length is significantly less than the mean spacing between defects, then nucleation is said to be homogeneous. Which is the result of diffusing adatoms meeting each other and forming stable clusters that reduce the free energy of the system.

1.3.3 Nucleation

As previously mentioned, there are two types of nucleation, heterogeneous and homogeneous. General statements about heterogeneous nucleation are difficult to make, as it is strongly dependent on the type of nucleation site and material system in question. However, capillarity theory is a conceptually useful tool for describing homogeneous nucleation*.

First, using basic thermodynamic arguments we can analyse the stability of a cluster of atoms with critical dimension r^*. This scenario is schematically depicted in figure 1.5. The cluster is a spherical cap of radius r situated on a planar substrate, where the surface free energy densities of the film–substrate, film–vapour and substrate–vapour interfaces are denoted by γ_{fs}, γ_{fv} and γ_{sv} respectively.

With respect to the supersaturated vapour there will be a reduction in the free energy, due bonding within the bulk of the cluster. However, there will also be a increase in the free energy as the result of forming new interfaces.

*It should be noted that there is some confusion in thin film literature regarding the distinction between heterogeneous and homogeneous nucleation. Some authors (typically in CVD literature) define any nucleation occurring on the growth surface as heterogeneous, since the vapour condensation is being catalysed by the presence of a surface.

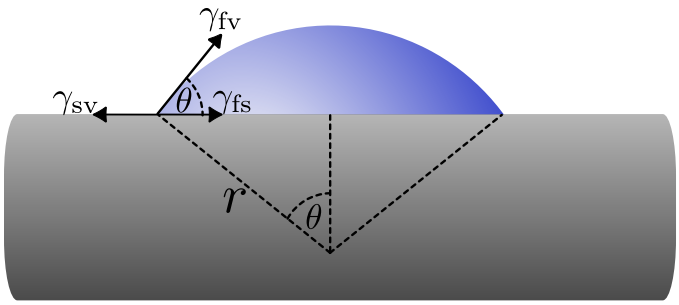

Figure 1.5: Nucleation of a spherical cap on a planar substrate, where the surface free energy densities of the film–substrate, film–vapour and substrate–vapour interfaces are denoted by γ_{fs}, γ_{fv} and γ_{sv} respectively.

The total free energy change is given by

$$\Delta G(r,\theta)_{nuc} = -V_{cap}\Delta G_v + A_{cap}\gamma_{fv} + A_{base}[\gamma_{fs} - \gamma_{sv}] \quad (1.3.3)$$

$$= c_1(\theta)r^3\Delta G_v + c_2(\theta)r^2\gamma_{fv} + c_3(\theta)r^2[\gamma_{fs} - \gamma_{sv}] \quad (1.3.4)$$

where ΔG_v is given by equation 1.3.1 and $c_1(\theta) = \frac{\pi}{3}(2 - 3\cos(\theta) + \cos^3(\theta))$, $c_2(\theta) = 2\pi(1 - \cos(\theta))$ and $c_3(\theta) = \pi\sin^2(\theta)$. A nucleus is thought to be stable if an infinitesimal increase in the size decreases the free energy, i.e. the free energy is a maximum at the critical size. This is easily solved for via differentiation,

$$\frac{\partial \Delta G_{nuc}}{\partial r} = -3c_1\Delta G_v r^2 + 2[c_2\gamma_{fv} + c_3(\gamma_{fs} - \gamma_{sv})]r = 0 \quad (1.3.5)$$

$$\Rightarrow r^* = \frac{2[c_3(\gamma_{sv} - \gamma_{fs}) - c_2\gamma_{fv}]}{-3c_1\Delta G_v} \quad (1.3.6)$$

Correspondingly, the activation energy for nucleation ΔG^*_{nuc} can be determined:

$$\Delta G^*_{nuc} = \Delta G(r^*) = \frac{4[c_3(\gamma_{fs} - \gamma_{sv}) + c_2\gamma_{fv}]^3}{27c_1^2\Delta G_v^2} \quad (1.3.7)$$

Furthermore, it is reasonable to expect that the wetting angle of the nucleus θ, is dependent all three of the surface free energy densities. This dependency can be determined by assuming that the free energy difference is minimum for a nucleus at a constant volume of $V_{cap} = c_1(\theta)r^3$, at equilibrium. Therefore we

must minimize $\Delta G(r,\theta) = c_2(\theta)r^2\gamma_{\rm fv} + c_3(\theta)r^2[\gamma_{\rm fs} - \gamma_{\rm sv}]$, subject to the constraint that $V_{\rm cap}$ is constant. This accomplished using the method of Lagrange multipliers, where the following Lagrangian is minimized,

$$L(r,\theta,\lambda) = c_2(\theta)r^2\gamma_{\rm fv} + c_3(\theta)r^2[\gamma_{\rm fs} - \gamma_{\rm sv}] - \lambda c_1(\theta)r^3 \tag{1.3.8}$$

Giving us the following set of equations

$$\frac{\partial L}{\partial r} = 0 \Rightarrow \frac{r\lambda}{2} = \frac{2[1-\cos(\theta)]\gamma_{\rm fv} + \sin^2(\theta)[\gamma_{\rm fs} - \gamma_{\rm sv}]}{2 - 3\cos(\theta) + \cos^3(\theta)} \tag{1.3.9}$$

$$\frac{\partial L}{\partial \theta} = 0 \Rightarrow \frac{r\lambda}{2} = \frac{\gamma_{\rm fv} + \cos(\theta)[\gamma_{\rm fs} - \gamma_{\rm sv}]}{\sin(\theta)} \tag{1.3.10}$$

Equating 1.3.10 and 1.3.10, and simplifying gives the following relation

$$\gamma_{\rm fv}\cos(\theta) + [\gamma_{\rm fs} - \gamma_{\rm sv}] = 0 \tag{1.3.11}$$

This is the famous Young's equation, relating wetting angle to surface free energy densities or surface tensions[†]. If Young's equation is then substituted into equation 1.3.7, the following simple expression is obtained for the activation energy of nucleation

$$\Delta G^*_{\rm nuc} = \frac{16\pi\gamma_{\rm fv}^3}{3\Delta G_v^2}\left[\frac{2 - 3\cos(\theta) + \cos^3(\theta)}{4}\right]^3 \tag{1.3.12}$$

$$= \Delta G^*_{\rm sph} f^3(\theta) \tag{1.3.13}$$

where $\Delta G^*_{\rm sph}$ is the activation energy for homogeneous nucleation of a sphere and $f(\theta)$ is a a monotonically increasing function ranging from $f(0) = 0$ and $f(\pi) = 1$. This expression has a straightforward and intuitive explanation. When the metal perfectly dewets the substrate (i.e. $\theta = \pi$), the activation energy is maximum and approaches that of homogeneous nucleation for a sphere. For partial wetting, the substrate catalyses the nucleation, and the

[†]This result is often derived by setting a so–called 'force balance' in the horizontal direction along the contact line. This does indeed give Young's equation, however the result is fortuitous. A force balance in the vertical direction would also be necessary, yielding the result of $\theta = 0$.

activation barrier is proportionally decreased by the shape factor of $f^3(\theta)$, and at perfect wetting the nucleation barrier is reduced to zero.

An important quantity determining the microstructure and properties of a metal thin film is the initial nucleation rate $\dot{N}$. The nucleation rate can be thought to be the product of three factors

$$\dot{N} = N^* A^* \omega \tag{1.3.14}$$

where N^* is the areal nucleation density, A^* is the area of a critical nucleus and ω is the impingement rate of adatoms on critical nuclei. Given that the energy barrier to nucleation is ΔG^*, then for a substrate at a temperature T, the probability of nucleation will be proportional to a Boltzmann factor [6], giving a nucleation density of:

$$N^* = n_s \exp(-\Delta G^* / k_\mathrm{B} T) \tag{1.3.15}$$

The critical area is simply $2\pi r^* \sin(\theta)$. The impingement rate can be thought as the product of deposition rate $\dot{R}$, and the hopping frequency of atoms on the surface w, given by equation 1.3.2. As such, at low temperatures and high deposition rates, high nucleation rates will lead to fine grained microstructure. Conversely, high temperatures and low deposition rates will lead to a coarse grained microstructure. It should also be noted that $\dot{N}$ is exponentially dependent on the nucleation barrier, which is dependent on the chemical potential and surface free energies; therefore, film growth of two different material/substrate systems under otherwise identical deposition parameters can have vastly different microstructures and morphologies.

1.3.4 Growth Modes

Three common growth modes have been identified for thin metal film growth, which are Frank-van der Merwe (FM) mode [7], Volmer-Weber (VW) mode [8] and Stranski-Krastanov (SK) mode [9]. These different growth modes are

shown in figure 1.6.

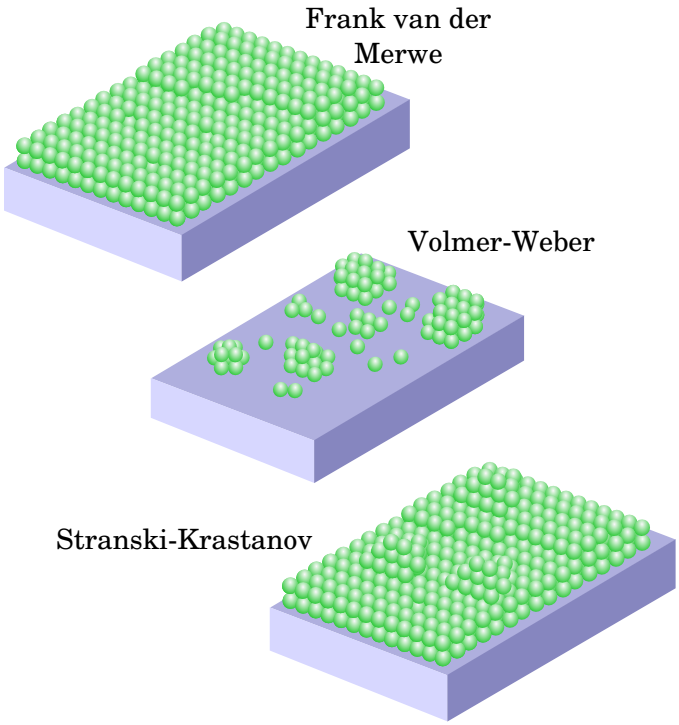

Figure 1.6: Illustration of Frank-van der Merwe, Volmer-Weber and Stranski-Krastanov growth modes

These different growth modes are most easily interpreted using Young's equation (1.3.11). As seen in figure 1.6 the FM mode is a layer-by-layer growth mode, which implies that the wetting angle must be $\theta \simeq 0$. From Young's equation this implies that

$$\gamma_{sv} \geq \gamma_{fv} + \gamma_{fs} \tag{1.3.16}$$

Physically, this inequality represents the condition that the additional free energies of the new interfaces created during nucleation is less than free energy of the previous interfacial region that existed before nucleation. Generally, a low surface tension metal will wet a high surface tension substrate.

From figure 1.5, the VW mode is characterized by island growth, where the wetting angle is greater than zero. Again, Young's equation can be applied,

giving the following

$$\gamma_{sv} < \gamma_{fs} + \gamma_{fv} \tag{1.3.17}$$

Physically, this inequality expresses the opposite scenario of FM growth, where the free energy of the new interfaces is greater than the previously existing interface. In this way, islands will form as a result of the energetic favorability of leaving the substrate–vacuum interface intact.

Lastly there is the SK growth mode, which is characterized by layer growth followed by island growth. The layer growth typically on the order of $5 - 6$ monolayers, after which island growth begins. This transition is typically governed by a critical strain energy developed in the epilayer, due to lattice mismatch.

1.4 Microstructures

As previously mentioned, the method of deposition, materials used and deposition parameters can significantly impact the microstructure of the film. The three fundamental structure types are single-crystal, polycrystalline and amorphous, which are atomistically depicted in figure 1.7.

As seen in figure 1.7 single crystal films possess extremely long range order, where a unit cell is periodically repeated in 3 dimensional space. Single crystal metal thin films are desirable for several microelectronic and optoelectronic applications, as they have the maximal possible conductivity at a given temperature. It should however be noted that any single crystal must posses a non-zero equilibrium concentration of defects (such as vacancies) due to the entropy of mixing [5], and without the presence of these defects a single crystal would have infinite conductivity [10].

Unfortunately the preparation of single crystal thin metal films can require very specific deposition parameters and substrates, which are most often not compatible with most NEMS/MEMS applications. One method of preparing a

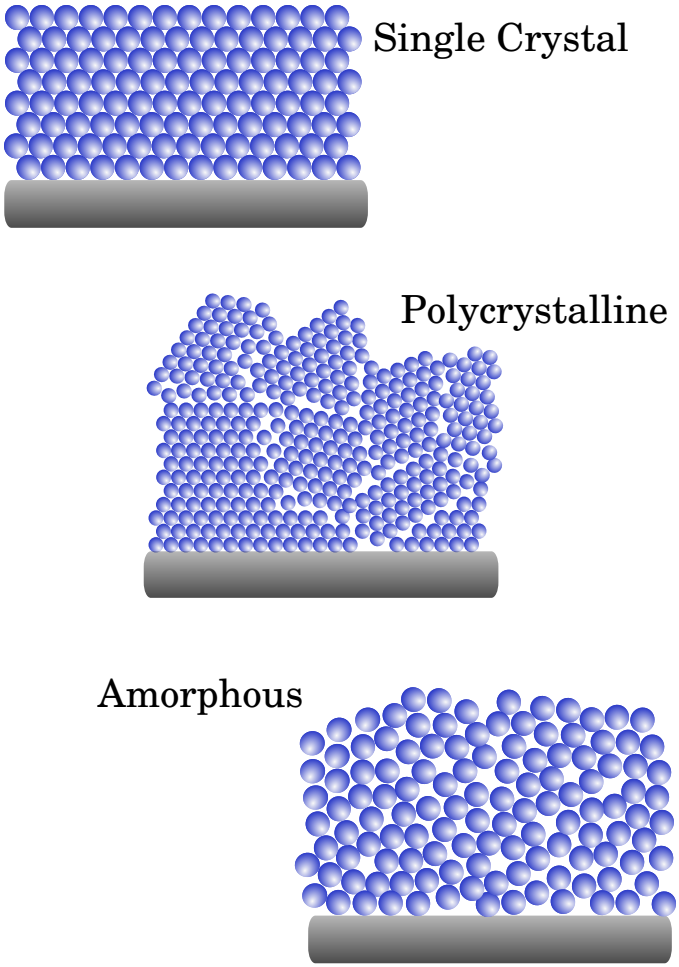

Figure 1.7: Atomistic depiction of the three different types of thin metal film microstructures: single crystal, polycrystalline and amorphous.

single crystal film is to have extremely low nucleation rates [11]. Inspection of equation 1.3.14 shows that this can be achieved at very high temperatures and low deposition rates. However, this method of single crystal film deposition is typically not employed, as the necessary temperatures are not practically accessible nor are the low deposition rates. The most common method of single crystal thin film deposition is through epitaxy [12], where the interface between the film and substrate occupy the same natural lattice sites. Although some mismatch between lattice parameters is possible (~ 0.5 %), finding a substrate that promotes epitaxy and is compatible with the required microfabrication

process for a given NEMS/MEMS application is often not possible.

The most common microstructure observed in thin metal films is polycrystalline. As shown in figure 1.7, a polycrystalline thin film consists of an ensemble of single crystals, referred to as grains. The properties of polycrystalline thin films are often dictated by their grain structure. The grain structure is typically characterized by grain size distribution, grain shape and crystallographic orientation (film texture). The influence of deposition parameters on grain structure has been extensively studied, and is most compactly expressed via various structure zone maps [13], [14].

Lastly, it is also possible to deposit thin metal film possessing an amorphous microstructure, which is depicted in figure 1.7. The naming of such a microstructure is somewhat of a misnomer, as the word 'amorphous' is derived from Greek meaning 'without shape or form'. This is far from the case, as metallic glasses (a more appropriate name) have a very rich and complex atomic structure. Metallic glasses are characterized by short range atomic ordering, or dominant coordination environments. The type and geometry of the dominant coordination environment significantly effect mechanical and thermal properties [15].

In relation to single crystal and polycrystalline microstructures, the understanding of metallic glass microstrucutures is still in its infancy. Current topics of research on metallic glasses include, the basic structure of metallic glasses [16–18], the relation between structure and glass forming ability [19, 20], and mechanical properties [21, 22]. The unique morphology, structure, mechanical properties of metallic glass thin films and their application in NEMS/MEMS devices will be explored in much greater detail in the following chapters of this thesis.

1.5 Stress in Thin Films

Depending on deposition parameters and materials used, metallic thin films will develop stress, which are relieved via bending of the film-substrate system. These stresses can be extrensic (such as thermal mismatch) or intrinsic. The mechanisms of intrinsic growth stresses and subsequent relaxation in metallic thin films are numerous, system dependent and there is still significant disagreement on the true mechanisms of intrinsic stress generation [23–26]. This topic is discussed in greater detail in chapter 3, since controlling film stress is critical to the performance of fabricated cantilevered NEMS/MEMS devices described in this thesis. The purpose of this section is to show how film stress can be derived from measurements.

The average stress in a thin film can be deduced using curvature measurements of the film-substrate system via the Stoney formula, which is

$$\bar{\sigma} = \frac{h_s^2 M_s \kappa}{6 h_f} \tag{1.5.1}$$

(all variables are defined later in this sections). However, the Stoney formula does not provide any information about the bending of a cantilever when released from the substrate, therefore we must derive an equation to predict the amount of bending. The Stoney equation is typically derived using an equilibrium approach where all of the forces and moments are set to zero. While this method is conceptually simple it is more difficult to use when the loading situation is non-uniform, therefore a more powerful approach, the total energy approach, is used [11]. The essence of the total energy method is to express the total energy of the film-substrate system as a function of the curvature and the strain in the chosen reference plane. Then it is determined which values of the curvature and reference strain give the minimum system energy.

Consider a substrate-film system with thicknesses h_s and h_f where the substrate has no intrinsic strains present and the biaxial modulii are independent

of thickness, which are denoted by M_s and M_f. The reference plane is chosen to be the midplane of the substrate which has curvature κ and strain of ϵ_0. The strain in the film layer is assumed be axially isotropic, but in general my vary through the thickness and is denoted by $\epsilon_m(z)$. This is illustrated in figure 1.8.

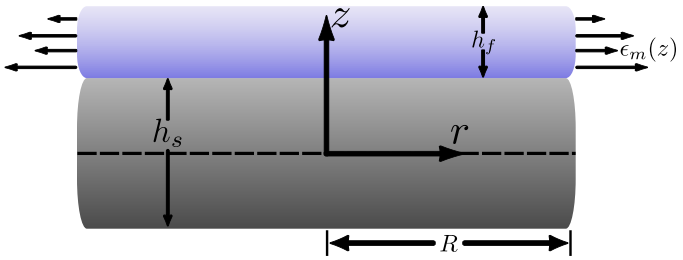

Figure 1.8: Film-substrate system with a strain distribution $\epsilon_m(z)$ throughout the thickness. When the traction is released this system will bend with curvature κ.

The strain energy density is written as [11]

$$U(r,z) = M(z)[\epsilon_0 - z\kappa + \epsilon_m(z)]^2 \tag{1.5.2}$$

where $M(z)$ the biaxial modulus as a function of thickness. The total energy is given by

$$V(\epsilon_0,\kappa) = \int_0^{2\pi}\int_0^{R}\int_{-h_s/2}^{h_s/2+h_f} U(r,z) r dz\, dr\, d\theta \tag{1.5.3}$$

$$= \pi R^2[\epsilon_0^2 C_{0,0} - 2\kappa\epsilon_0 C_{1,0} + 2\epsilon_0 C_{0,1} - 2\kappa C_{1,1} + \kappa^2\epsilon_0 C_{2,0} + C_{0,2}] \tag{1.5.4}$$

where

$$C_{i,j} = \int_{-h_s/2}^{h_s/2+h_f} z^i M(z)\epsilon_m(z)^j\, dz \tag{1.5.5}$$

Setting the gradient to zero $\nabla_{\epsilon_0,\kappa} V(\epsilon_0,\kappa) = 0$, then the total energy will be minimized. This procedure gives the following set of equations

$$\begin{pmatrix} C_{1,0} & -C_{0,0} \\ C_{2,0} & -C_{1,0} \end{pmatrix} \begin{pmatrix} \kappa \\ \epsilon_0 \end{pmatrix} = \begin{pmatrix} C_{0,1} \\ C_{1,1} \end{pmatrix} \tag{1.5.6}$$

The curvature is then solved for using Cramer's rule, yielding

$$\kappa = \frac{C_{1,1}C_{0,0} - C_{0,1}C_{1,0}}{C_{2,0}C_{0,0} - C_{1,0}^2} \tag{1.5.7}$$

Making the thin film approximation, $M_s h_s \gg M_f h_f$, then the constants in equation 1.5.7 are

$$\begin{aligned} C_{0,0} &= M_s h_s \\ C_{1,0} &= 0 \\ C_{2,0} &= \frac{M_s h_s^3}{12} \\ C_{1,1} &= \int_{-h_s/2}^{h_s/2+h_f} z\epsilon_m(z)\, dz \end{aligned}$$

Substituting these constants into equation 1.5.7 gives an integral equation relating the curvature as a function of film thickness to the intrinsic strain distribution in the film

$$\kappa(h_f) = \frac{12M_f}{M_s h_s^3} \int_{-h_s/2}^{h_s/2+h_f} z\epsilon_m(z)\, dz \tag{1.5.8}$$

Since curvature is the physical quantity that is measured, equation 1.5.8 is inverted for the strain distribution. This is accomplished by differentiation with respect to the film thickness, giving

$$\frac{\partial \kappa}{\partial h_f} = \frac{6M_f}{h_s^2 M_s}\epsilon_m(h_f) \tag{1.5.9}$$

Making use of Hooke's law, the final expression for the distribution of stress as a function of thickness is:

$$\sigma(h_f) = \frac{h_s^2 M_s}{6}\frac{\partial \kappa}{\partial h_f} \tag{1.5.10}$$

It is worth noting that if this expression is used to calculate the mean film stress the Stoney formula is recovered. Typically when the Stoney equation

is derived it is assumed that the film has a uniform stress, which often is not the case. Equation 3.3.8 explains why the Stoney equation still produces a meaningful result even when the stress is not uniformly distributed.

1.6 Thermal Grooving of Thin Films

As metallization layers on devices become increasingly thinner, solid-state dewetting, which results in the break up of the film becomes a serious concern. Although the phenomena of liquid-state dewetting was first discovered over 100 years ago by Lord Rayleigh [27], a firm theoretical understanding of solid-state dewetting remains elusive, due to the complex nature of a real assembly of grains composing a thin film. As such, chapter 4 investigates some of the fundamental mechanisms by which thin metal films dewet in the solid-state. In this section, the process of thermal grooving [28] is reviewed, as several key concepts of solid-state dewetting are covered and it is the fundamental mechanism by which the solid-state dewetting process is initiated.

Given the surface of a thin film with no overhangs, in the continuum limit, the height of the surface with respect to some reference plane can be represented by $h = h(x, t)$. If an atom is transported from a region of zero surface curvature to some other region of curvature κ, there will be a change in chemical potential $\mu(\kappa)$. It can be shown [5] that

$$\mu(K) = -\Omega\gamma_{\text{fs}}\kappa \tag{1.6.1}$$

where Ω is the atomic volume. Physically this relation is understood by analysing the average bonding environment, which is roughly proportional the local curvature; at the tops of hills ($\kappa < 0$) the average number of bonds will decrease, and in valleys ($\kappa > 0$) the average number of bonds will decrease. These differences in chemical potential on the surface will result in a net surface drift of atoms, which will flow in the direction on the gradient of the surface chemical potential. From the Einstein relation [29] the drift

current is given by

$$\mathbf{j} = -\frac{D_s \delta}{k_\mathrm{B} T} \nabla \mu = \frac{D_s \delta \Omega \gamma_\mathrm{fs}}{k_\mathrm{B} T} \nabla \kappa \tag{1.6.2}$$

where D_s is the surface diffusivity and δ is the width of the diffusion layer. Assuming the surface atoms are in equilibrium with their vapour, conservation of mass implies that the rate of change in height of a surface element is equal to the inward flux of atoms,

$$\frac{\partial}{\partial t} \int_V h \, dV = -\Omega \int_{\partial V} \mathbf{j} \cdot \mathbf{n} \, dS \tag{1.6.3}$$

Making use of the fundamental theorem of calculus,

$$\int_V \frac{\partial h}{\partial t} \, dV = -\Omega \int_V \nabla \cdot \mathbf{j} \, dV \tag{1.6.4}$$

which gives the continuity relation of surface diffusion

$$\frac{\partial h}{\partial t} + \Omega \nabla \cdot \mathbf{j} = 0 \tag{1.6.5}$$

Combining equations 1.6.2 and 1.6.5 gives

$$\frac{\partial h}{\partial t} + B \nabla^2 \kappa = 0 \tag{1.6.6}$$

where $B = \frac{D_s \delta \Omega^2 \gamma_\mathrm{fs}}{k_\mathrm{B} T}$. If it is further assumed that the surface slopes are small $\kappa \simeq \nabla^2 h$, giving the surface diffusion equation

$$\frac{\partial h}{\partial t} + B \nabla^4 h = 0 \tag{1.6.7}$$

The surface diffusion equation can now be used to solve for the evolution of a symmetric grain boundary with an equilibrium angle of $\theta_0 = \sin^{-1}(\gamma_\mathrm{gb}/2\gamma_\mathrm{fs})$, where γ_gb is the grain boundary free energy density. This configuration is shown in figure 1.9. Therefore equation 1.6.7 is solved with the following

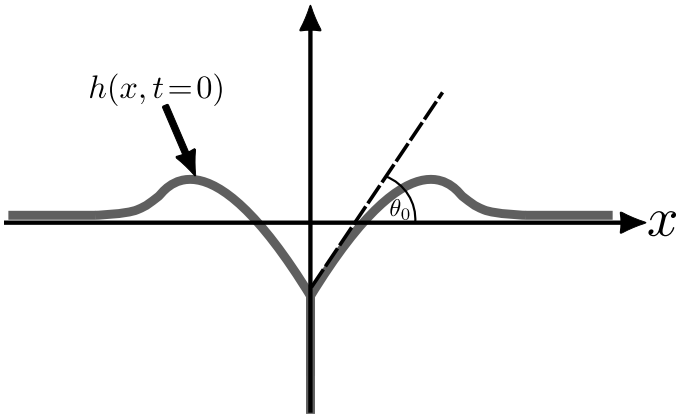

Figure 1.9: Profile of a symmetric grain boundary with an equilibrium angle of θ_0.

boundary and initial conditions

$$h(x,t)|_{t=0} = h_0(x) \tag{1.6.8}$$

$$\left.\frac{\partial h(x,t)}{\partial x}\right|_{x=0} = \tan(\theta_0) = m \tag{1.6.9}$$

$$\left.\frac{\partial^3 h(x,t)}{\partial x^3}\right|_{x=0} = 0 \tag{1.6.10}$$

$$h(x,t)|_{x\to\infty} = 0 \tag{1.6.11}$$

where condition 1.6.9 expresses the constant equilibrium angle, and condition 1.6.10 ensures that grain boundary diffusion is negligible with respect to surface diffusion. Since this a symmetric boundary value problem over a semi-infinite domain, it is most naturally solved via cosine transformation of equation 1.6.7, giving

$$\frac{\partial H(k,t)}{\partial t} + Bk^4 H(k,t) = -Bk^2 m \tag{1.6.12}$$

where $H(k,t) = \int_0^\infty h(x,t)\cos(kx)\,dx$. This first-order differential equation is easily solved, giving

$$H(k,t) = -mk^{-2}(1 - e^{-k^4 Bt}) + H(k,0)e^{-k^4 Bt} \tag{1.6.13}$$

Applying the inverse cosine transformation results in the following integral expression for the grain boundary profile as a function of time

$$h(x,t) = -\frac{2m}{\pi}\int_0^\infty \frac{(1-e^{-k^4Bt})}{k^2}\cos(kx)dk + \frac{2}{\pi}\int_0^\infty H(k,0)e^{-k^4Bt}\cos(kx)dk \tag{1.6.14}$$

From the form of this expression the natural length scale during thermal grooving is identified as $(Bt)^{1/4}$. For an initially flat grain ($h(x,0) = 0$) the depth of the groove can be evaluated as a function of time.

$$\begin{aligned} h(0,t) &= -\frac{2m}{\pi}\int_0^\infty \frac{(1-e^{-k^4Bt})}{k^2}dk & (1.6.15)\\ &= -\frac{2m}{\pi}\int_0^\infty 4k^2Bt(1-e^{-k^4Bt})dk & (1.6.16)\\ &= -\frac{2m(Bt)^{1/4}}{\pi}\int_0^\infty x^{3/4-1}e^{-x}\,dx & (1.6.17)\\ &= -\frac{2m(Bt)^{1/4}}{\pi}\Gamma(3/4) & (1.6.18) \end{aligned}$$

This gives the important result that the depth of the groove increases monotonically in time and is proportional to $(Bt)^{1/4}$. It is also straightforward to show that this result holds true for an arbitrary initial profile, given that $H(k,0)$ is of exponential order.

Shown in figure 1.10 is the time evolution of a grain boundary profile having $\theta_0 = 45°$, $B = 1.0$ and $h(x,0) = -e^{-|x|}$, which is solved numerically using equation 1.6.14. As expected by equation 1.6.18 the groove deepens and widens with time, but there is also the development of a so-called 'lip' at the rim of the grain boundary. This lip is characteristic of diffusional thermal grooving and often observed [30, 31].

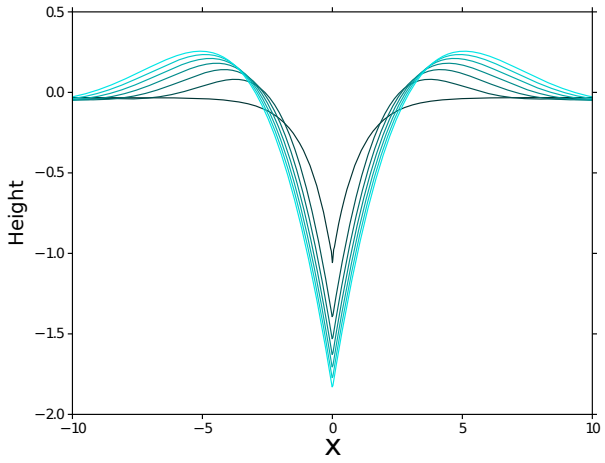

Figure 1.10: Time evolution of a symmetric grain boundary with $\theta_0 = 45\,\text{deg}$, $B = 1.0$ and $h(x,0) = -e^{-|x|}$.

1.7 Characterization Techniques

There are an ever growing number of experimental techniques used for the characterization of thin film materials. The purpose of this section is to provide a brief overview of the most important characterization techniques used throughout the course of this thesis.

1.7.1 X-Ray Diffraction

X-ray diffraction (XRD) is a versatile non-vacuum, non-destructive inverse technique that is primarily used to determine the underlying atomic structure of a film. In XRD a beam of high energy photons (X-rays) are fired at a sample, where the intensity of scattered photons is measured. Since the photon wavelengths used is roughly on the order of atomic spacings (e.g. photons from a Cu$K\alpha$ source have a wavelength of $\sim$ 1.54 Å), diffraction effects can be observed. The position of diffraction maxima are set by the Laue conditions

$$\mathbf{\Delta k} = \mathbf{\Delta G} \tag{1.7.1}$$

where $\mathbf{\Delta k}$ is the scattering vector of the elastically scattered photons and $\mathbf{\Delta G}$ is a reciprocal lattice vector of the material lattice. Using equation 1.7.1 measured peak positions can be used to deduce the spacing between planes in the diffracting crystals.

XRD can also be used to infer quantities such as grain size, texture, lattice strain, microstrain and density. It is also one of the primary tools used for the identification phases present in a film. Further details on XRD can be found in the following reference materials [32, 33].

1.7.2 Scanning Electron Microscopy

Scanning electron microscopy (SEM) is a mostly qualitative technique used for the imaging of micro/nanoscale features of surfaces. In SEM an electron beam, with energies typically ranging from a few keV to 50 keV, is rastered across the sample surface where electrons are scattered. These scattered electrons are then collected at various detectors and used for image formation. Due to the teardrop-shaped interaction volume of electrons entering the sample, sloped surfaces scatter a greater number secondary electrons, giving rise to contrast in SEM.

Despite being a vacuum based technique, SEM is a relatively simple characterization method, often requiring very little sample preparation. Imaging electrically insulating or magnetic samples can be challenging, but are certainly possible. The primary information gleaned from SEM is feature size such as grain size or device dimensions and sample morphology. More information in SEM can be found in [34, 35].

1.7.3 Transmission Electron Microscopy

Transmission electron microscopy (TEM) is a powerful technique used for structural characterization of nanometer scale features of a sample. In TEM a

beam of high energy electrons (typically 100 to 300 keV) is focused on an electron transparent sample, where the transmitted electrons are used for image formation. Diffracted electrons can also be used to identify crystal structure, spatial location, defects and orientation. Also, phase contrast imaging or high resolution TEM is an increasingly popular technique where direct imaging of atomic columns is possible. There also exists a variety analytical methods in TEM, such as X-ray energy dispersive analysis (EDX) and electron energy loss spectroscopy (EELS), which allow for elemental identification and compositional identification.

The primary problem in TEM is proper sample preparation and the effects of sample preparation. Depending on imaging mode used and elemental composition of the sample, it must have a thickness ranging from 10s of nm to a few Å. This can be performed via various methods, such as traditional grinding and polishing or focused ion beam (FIB) cutting, yet most methods still require a great deal of skill and expertise. Moreover, particular care must be taken when interpreting TEM data of defects or metastable samples, due to the effects of sample preparation. More information on TEM can be found in [36].

1.7.4 Nanoindentation

Nanoindentation is a characterization technique used to measure mechanical properties of thin films. A tip of known geometry and material constants is used to indent the surface of a thin film, which produces a load-displacement curve. Since the cross-sectional area of the tip as a function of height is known, the hardness of the film can be determined from the load-displacement curve. If the Young's modulus and Poisson's ratio of both the substrate and indenter are known, the reduced modulus of the film can also be determined. Using nanoindentation it is possible map both the hardness and modulus of the film.

Although acquiring nanoindentation data is rather straightforward, care must be taken during measurements. In particular indents must be sufficiently deep

such that surface effects do not effect measurements. Conversely, if the indent is too deep substrate effects may dominate the measurements. It is also important that samples are bonded using a non-compliant epoxy/adhesive. More information on nanoindentation can be found in [37, 38].

1.7.5 Multi-beam Optical Stress Sensor

Multi-beam optical stress sensing (MOSS) is an in-situ technique for measuring film stress during deposition [39]. In the MOSS method, a laser is shone through a quartz view port in the deposition chamber which is reflected off the substrate. Prior to the view port, the laser beam passes through a pairs of elatons which splits the beam into an array of parallel beams. The beams reflected off the substrate pass to another view port, where they are then imaged with a CCD camera. This effectively provides a mapping of the curving substrate. If the angle of reflection of the laser beam and the substrate normal is θ, and the distance between the substrate and the camera is L, then it can be shown [40] that the curvature of the substrate is

$$\kappa = \frac{\cos(\theta)}{2L}\left(1 - D/D_0\right) \tag{1.7.2}$$

where D is the average spot spacing and D_0 is the initial average spot spacing. This measured data can then be converted to film stress using equation 3.3.8.

1.7.6 Atomic Force Microscopy

Since chapter 3 is devoted to the fabrication of all-metal atomic force microscope (AFM) probes, and in chapter 4 AFM is a heavily used characterization tool, a more detail description of AFM will be given. The AFM, which is a type of scanning probe microscope (SPM), is a high (spatial) resolution surface imaging tool that maps surface topography by using attractive and repulsive interaction forces between a few atoms attached at a tip on a cantilever and

a sample. The AFM uses 3-dimensional piezo-mechanical drivers to achieve precise sub-nanometer positioning. The most basic mode of AFM operation is contact mode, (C-AFM), where the cantilever is pressed against the sample surface and the close-range repulsive atomic forces cause the cantilever to bend. A laser is trained on the cantilever backside (figure 1.11), and a grid of photodiodes senses the reflected light to measure cantilever deflection. In this way, very small deflections of the cantilever is tracked by large deflections of the laser on the photodetector array. As the cantilever is scanned across the surface the tip deflection is monitored to create a three-dimensional image of the surface. C-AFM has two configurations; constant-height and constant-force. In constant-height configuration, the cantilever is held at a set height above the surface and scanned, using the deflection measurements to create a height-mapping of the sample. In constant-force configuration, a control system is used to adjust the vertical height of the tip such that the cantilever deflection (and thus the force on the sample) remains constant, these height adjustments are then used to create the image [41]. Non-contact AFM (NC-AFM), which was developed by Martin *et al* [42] in 1987, whose operation involves the cantilever being driven at its resonant frequency. Equation 1.7.3 is the basic formula relating the resonant frequency, f_0, of any spring-mass system to the stiffness or spring constant, k, and the effective load or mass of the oscillator, m.

$$f_0 \propto \sqrt{\frac{k}{m}} \tag{1.7.3}$$

When the tip of the vibrating cantilever is brought close to the surface it experiences an attractive force towards the sample atoms [43]. This atomic force puts a load on the resonating cantilever, thus changing its resonant frequency, which can be used as an indicator of the tip-sample distance.

In non-contact mode the cantilever is approached to the surface so that mild interaction forces cause a frequency shift. Then, as the tip is scanned across the surface the resonance of the cantilever shifts due to an effective change in its

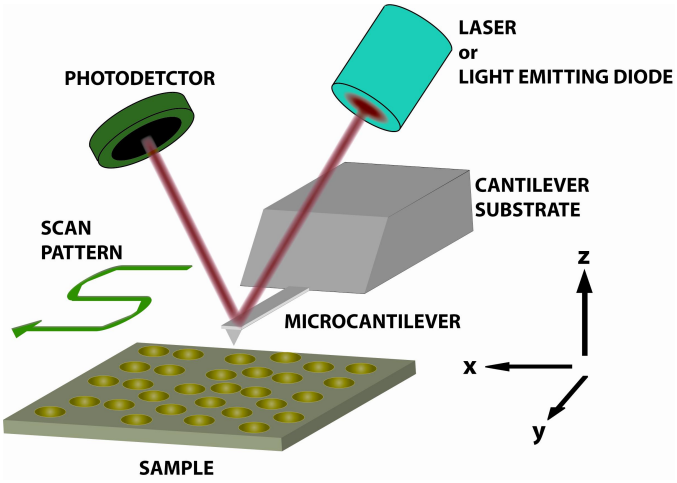

Figure 1.11: Basic configuration of a modern atomic force microscope. The cantilever substrate is typically fastened to the piezo-actuator to provide the driving force for cantilever resonance.

spring constant [43]. The change in frequency is detected by a control system and converted into a change in height, which is then applied to the z-axis piezo-actuator to change the tip position to restore the original resonance (similar to contact-mode constant force operation). The tip scans the surface, raising and lowering as the surface changes, and the AFM software once again generates a three-dimensional plot of the sample surface. After the invention of NC-AFM, Zhong *et al.* [44] proposed another mode of operation known as tapping-mode, which is similar to non-contact operation, except the tip makes intermittent physical contact with the surface. For further explanations of these, as well as additional modes of operation, please refer to the cited literature.

1.8 Optical Lithography

The micromachining of NEMS/MEMS devices in this thesis was accomplished using the fundamental step in almost all microfabrication processes: optical lithography [45], [3]. The basic principle of photolithography is illustrated in figures 1.12(a)-1.12(c). In order to transfer a certain pattern onto a substrate

material, it is first spin coated with a thin layer of photosensitive material, called photoresist, or just resist. Using a high precision laser mask writer, a master copy of the pattern is made on a mask. The mask is then placed in close proximity or contact with the resist covered substrate and illuminated with UV light (figure 1.12(a)). The UV light causes a reaction in the resist such that the exposed areas are selectively removed by a developing chemical (figure 1.12(b)). The exposed areas of the substrate are then chemically etched to transfer the mask pattern into the substrate material. The resist is then removed and the pattern transfer is complete (figure 1.12(c)). More information on optical lithography can be found in the given references.

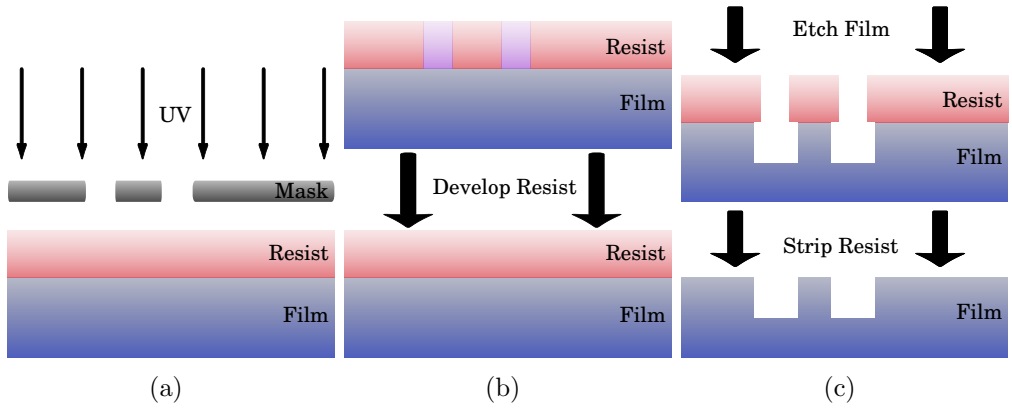

Figure 1.12: (a) Photoresist is deposited onto material that is to be patterned, which is exposed to UV light while certain regions are covered by the mask. (b) The UV exposed resist is chemically altered and is selectively removed by developer etchant. c) Remaining resist masks the material as exposed areas are etched. Resist is stripped and pattern transfer is complete.

References

[1] S. M. Spearing. Materials issues in microelectromechanical systems (mems). *Acta Mater.*, 48(1):179, 2000.

[2] K. E. Petersen. Silicon as a mechanical material. *Proc. IEEE*, 70(5):420, 1982.

[3] S.A. Campbell. *The science and engineering of microelectronic fabrication.* Oxford University Press, New York, NY, USA, 2001.

[4] T. Iida, Y. Kita, H. Okano, I. Katayama, and T. Tanaka. Equation for the vapor pressure of liquid metals and calculations of their enthalpies of evaporation. *J. High Temp. Mat. Proc.*, 10(1):199, 1992.

[5] P. Shewman. *Diffusion in Solids.* The Minerals, Metals Materials Society, Warrendale, PA, 1989.

[6] D.V. Schroeder. *Introduction to thermal physics.* Addison Wesley Longman, San Francisco, CA, 2000.

[7] E Bauer. Phenomenal theory of precipitation on surfaces. *Z. Kristallogr*, 110: 372, 1958.

[8] M Volmer and A Weber. Germ-formation in oversaturated figures. *Z. Phys. Chem*, 119(3):277, 1926.

[9] I. N. Stranski and Krastanow. *Sitzungsber*, 146:797, 1937.

[10] R.P. Feynman. *The Feynman lectures on physics: Volume III.* Addison Wesley Longman, Menlo Park, CA, 1966.

[11] L. B. Freund and S. Suresh. *Thin film materials: stress, defect formation and surface evolution.* Cambrdige university press, Cambridge, UK, 2003.

[12] R Koch. The intrinsic stress of polycrystalline and epitaxial thin metal-films.

J. Phys. Condens. Matter, 6(45):9519, 1994.

[13] J. A. Thornton. Influence of apparatus geometry and deposition conditions on structure and topography of thick sputtered coatings. *J. Vac. Sci. Technol.*, 11 (4):666, 1974.

[14] H. T. G. Hentzell, C. R. M. Grovenor, and D. A. Smith. Grain-structure variation with temperature for evaporated metal-films. *J. Vac. Sci. Technol., A*, 2(2):218, 1984.

[15] L. Zhang, Y. Q. Cheng, A. J. Cao, J. Xu, and E. Ma. Bulk metallic glasses with large plasticity: Composition design from the structural perspective. *Acta Mater.*, 57(4):1154, 2009.

[16] H. W. Sheng, W. K. Luo, F. M. Alamgir, J. M. Bai, and E. Ma. Atomic packing and short-to-medium-range in metallic glasses. *Nature*, 439(7075):419, 2006.

[17] D. B. Miracle. A structural model for metallic glasses. *Nat. Mater.*, 3(10):697, 2004.

[18] A. Hirata, P.F. Guan, T. Fujita, Y. Hirotsu, A. Inoue, A. R. Yavari, T. Sakurai, and M. W Chen. Direct observation of local atomic order in a metallic glass. *Nat. Mater.*, 10(1):28, 2011.

[19] T. Egami. Atomistic mechanism of bulk metallic glass formation. *J. Non-Cryst. Solids*, 317(1):30, 2003.

[20] Y. Li, Q. Guo, J. A. Kalb, and C. V. Thompson. Matching glass-forming ability with the density of the amorphous phase. *Science*, 322(5909):1816, 2008.

[21] H. Wagner, D. Bedorf, S. Kuchemann, M. Schwabe, B. Zhang, W. Arnold, and K. Samwer. Local elastic properties of a metallic glass. *Nat. Mater.*, 10(6):439, 2011.

[22] M.D. Demetriou, M.E. Launey, G. Garrett, J.P. Schramm, D.C. Hofmann, W.L. Johnson, and R.O. Ritchie. A damage-tolerant glass. *Nat. Mater.*, 10(2): 123, 2011.

[23] F. Spaepen. Interfaces and stresses in thin films. *Acta Mater.*, 48(1):31, 2000.

[24] E. Chason, B. W. Sheldon, L. B. Freund, J. A. Floro, and S. J. Hearne. Origin of compressive residual stress in polycrystalline thin films. *Phys. Rev. Lett.*, 88 (15):156103, 2002.

[25] R. Koch, D. Hu, and A. K. Das. Compressive stress in polycrystalline volmer-weber films. *Phys. Rev. Let.*, 94(14), 2005.

[26] J. Leib, R. Mnig, and C. V. Thompson. Direct evidence for effects of grain structure on reversible compressive deposition stresses in polycrystalline gold films. *Phys. Rev. Let.*, 102(25), 2009.

[27] L. Rayleigh. On the stability of liquid jets. *Proc. London Math. Soc*, 10(4), 1878.

[28] W. W. Mullins. Theory of thermal grooving. *J. Appl. Phys.*, 28(3):333, 1957.

[29] R. Kubo. Statistical-mechanical theory of irreversible processes .1. general theory and simple applications to magnetic and conduction problems. *J. Phys. Soc. Jpn.*, 12(6):570, 1957.

[30] M. J. Rost, D. A. Quist, and J. W. M. Frenken. Grains, growth, and grooving. *Phys. Rev. Lett.*, 91(2):26101, 2003.

[31] O. Pierre-Louis, A. Chame, and Y. Saito. Dewetting of ultrathin solid films. *Phys. Rev. Lett.*, 103(19):195501, 2009.

[32] M. Birkholz. *Thin film analysis by X-ray scattering.* Wiley-VCH, Weinheim, GER, 2006.

[33] B. D. Cullity and S.R. Stock. *Elements of X-ray diffraction.* Prentice Hall, 2001.

[34] J. Goldstein, D. Newbury, D. Joy, C. Lyman, P. Echlin, E. Lifshin, L. Sawyer, and J. Michael. *Scanning electron microscopy and X-ray microanalysis.* Springer, 2003.

[35] I. M. Watt. *The principles and practice of electron microscopy.* Cambridge University Press, 1997.

References

[36] D. B. William and C. B. Carter. *Transmission electron microscopy: a textbook for materials science*. Springer, 1996.

[37] W. C. Oliver and G. M. Pharr. Measurement of hardness and elastic modulus by instrumented indentation: Advances in understanding and refinements to methodology. *J. of Mater. Res.*, 19(1):3, 2004.

[38] A. C. Fischer-Cripps. *Nanoindentation*. Springer, 2004.

[39] A. L. Shull and F. Spaepen. Measurements of stress during vapor deposition of copper and silver thin films and multilayers. *J. Appl. Phys.*, 80(11):6243, 1996.

[40] J. A Floro and E. Chason. Measuring ge segregation by real-time stress monitoring during si1-xgex molecular beam epitaxy. *Appl. Phys. Lett*, 69(25):3830, 1996.

[41] R. Garcia and Perez R. Dynamic atomic force microscopy methods. *Surf. Sci. Rep.*, 47(6):197, 2002.

[42] Y. Martin, C. C. Williams, and H. K. Wickramasinghe. Atomic force microscope–force mapping and profiling on a sub 100-[a-ring] scale. *J. Appl. Phys.*, 61(10):4723, 1987.

[43] Y. Seo and W. Jhe. Atomic force microscopy and spectroscopy. *Rep. Prog. Phys.*, 71(1):016101, 2008.

[44] Q. Zhong, D. Inniss, K. Kjoller, and et al. Fractured polymer silica fiber surface studied by tapping mode atomic force microscopy. *Surf. Sci.*, 290(1), 1993.

[45] D. Bratton, D. Yang, J. Y. Dai, and et. al. Recent progress in high resolution lithography. *Polym. Adv. Technol.*, 17(2):94, 2006.

2

Tailoring the microstructure and surface morphology of metal thin films for nano-electro-mechanical systems applications *

2.1 Introduction

Thin films have been widely used in practical applications such as force sensing devices [1, 2], mass sensors [3, 4] and separation membranes [5] over the past decade. Most structural components in micro-electro- mechanical/nano-electro-mechanical systems (MEMS/NEMS) are usually fabricated from silicon-based compounds such as silicon nitride, silicon carbide and silicon oxide, with silicon being by far the most widely used [6–9]. Despite being easy to etch, elastically stiff, and very hard, silicon has low fracture strength, ductility, and wear resistance, resulting in low reliability for in-contact moving parts of the structures [10]. Moreover, silicon is poorly suited for applications requiring high electrical conductivity and/or optical reflectivity. Therefore, metals have been proposed as a potential substitute for Si in MEMS/NEMS device applications since metals offer higher electrical conductivity and superior ductility [11, 12].

Most conventional thin metal films deposited at temperatures less than 0.2

*Material in this chapter has been published in:
▶ E. Luber, R. Mohammadi, C. Ophus, Z. Lee, N. Nelson-Fitzpatrick, K. Westra, S. Evoy, U. Dahmen, V. Radmilovic and D. Mitlin. *Nanotechnology* **19**, 125705 (2008).

times the melting temperature exhibit substantial variation in grain size throughout the thickness of the film [13]. It is found that this variability in grain size can result in the development of a residual stress gradient across the film [13]. In released devices, such as singly clamped cantilevers, this residual stress is relieved by deformation bending of the beam [14]. Additionally, metal films typically exhibit low strength and hardness, and high surface roughness. Due the aforementioned properties of thin metal films, their usage as a potential substitute for silicon has achieved limited success.

Nickel has received interest for structural components in MEMS applications such as microswitches, accelerometers and motors [15]. Nickel has higher ductility and fracture resistance than silicon; however, nickel has low strength and hardness [16, 17] which precludes it from being used in structural components for NEMS. This shortcoming can cause deformation and even failure during the device release steps when stresses are present. Also, high surface roughness resulting from competitive grain growth is another disadvantage of metals that limits their use in NEMS applications. Both the strength and fatigue resistance of Ni MEMS can be improved by producing nanoscale equiaxed grains [18], but this has yet to be utilized for the fabrication of Ni NEMS. The smallest single-anchored cantilevers reported to date had the length, width and thickness of 500 µm × 50 µm × 0.84 µm for low contact-force integrated circuit probing [19] and 10 µm × 4 µm × 0.210 µm as microswitches [20], respectively.

To overcome the above-mentioned limitations of nickel such that it can be more widely used in structural components of NEMS devices, we need to increase its hardness, decrease its surface roughness, and make the devices free of residual stress. Since this polycrystalline microstructure is responsible for the majority of these limitations, they can be overcome be tailoring the microstructure in a very specific way. One approach is to grow single-crystal Ni; much like single-crystal Si, these films would have very low roughnesses and zero residual stress. Unfortunately, the deposition of single-crystal metal films is very non-trivial and expensive. An alternative approach is to remove all long-range order within the matrix (creating an amorphous or amorphous-

nanocrystalline microstructure), thereby eliminating any substantial residual stress gradients and reducing the film roughening caused by large grains at the surface.

Our approach to designing an amorphous microstructure is to alloy Ni with other elements via co-deposition at high cooling rates (sputtering). General criteria for the formation of a binary metallic glass are increasing atomic size ratio of constituent elements [21], large negative heats of mixing [22, 23], and high cooling rates [24]. Based on these criteria, the alloying element chosen in this study is molybdenum. The Ni–Mo equilibrium phase diagram [25] shows the presence of three intermetallic phases, NiMo, Ni_3Mo, and Ni_4Mo; thermodynamically, it is expected that systems with a large number of intermetallics will have a large negative heat of mixing. Also, there is a reasonable atomic size mismatch of $r_{\mathrm{Mo}}/r_{\mathrm{Ni}} = 1.1$.

Previous study on Ni–Mo has mainly focused on the possibility of amorphization in multilayers of pure Ni and pure Mo thin films prepared by the Ar^+-ion-beam-assisted deposition (IBAD) technique [26]. The authors showed that IBAD is a non-equilibrium method and, therefore, phase formation and evolution is affected by atom mobility. In another work, the ion-beam mixing (IBM) process was used to prepare Ni–Mo multilayer film, and the microhardness of the multilayer film was investigated, showing an increase over that of pure Ni [27].

2.2 Experimental Procedure

Since the discovery of metallic glasses over 40 years ago [28], there have been several attempts to explain the mechanisms of forming metallic glasses [21], and predicting if a system will have an amorphous phase and at what compositions it will occur [22, 29]. Despite the theoretical advances in the field of metallic glasses, the criteria for metallic glass formation still remain largely empirical and qualitative; therefore, our alloy design is as follows. Using the

general criteria for metallic glass formation, our material system is carefully chosen (Ni– Mo in the present study). Beyond this, it is difficult to predict at what composition the amorphous phase will be, or if it exists at all; therefore, it is necessary to conduct a systematic study of the material system.

We deposited 1 µm thick Ni–Mo films from pure Ni to pure Mo in roughly 10 at.% intervals onto 4 inch ⟨100⟩ naturally oxidized silicon wafers using a DC-magnetron co-sputtering system (AJA International). Prior to sputtering, the wafers were cleaned using a 7:5:1 mixture of H_2O:H_2SO_4:H_2O_2 . Argon sputtering was maintained at 4.0 mTorr with a base pressure of 7.0×10^{-7} Torr. Deposition was done in a sputter-up configuration with continuous substrate rotation to ensure film uniformity. The Ni deposition rate was kept constant at 1.42 Å/sec, while the Mo rate was varied to produce the desired film stoichiometry. Film compositions were confirmed using electron dispersed spectroscopy (EDS) mounted on a Hitachi S3000N scanning electron microscope. A 5 nm thick Ti adhesion layer was used to prevent film delamination from the substrate. The film thickness was confirmed using chemical etching (a hot mixture of HCl and HNO_3) and a contact profilometer (Tencor Alphastep).

In order to determine the ideal composition to be used for the fabrication of NEMS components, it was necessary to measure important physical properties, such as roughness, modulus, hardness, and conductivity. The roughness was measured using tapping-mode AFM, the modulus and hardness were measured using nanoindentation, and the conductivity was measured using a standard thin-film four-point probe test. A more detailed description of the measurement methods used is given elsewhere [11]. Also, the microstructure was analyzed using x-ray diffraction (XRD). We used a Bruker AXS D8 Discover diffractometer with a GADDS area detector. A Cu $K\alpha$ radiation source collected the x-ray scans from a sample mounted on a two-axis rotation stage that also allowed for XYZ translation.

In order to further understand the measured physical properties, a detailed investigation of the microstructure was performed using high-resolution TEM (HRTEM). HRTEM was done using a FEI Tecnai G^2 F20 TEM operating

at 200 kV. Finally, we fabricated single-clamped Ni–Mo cantilevers at widths of 400 and 800 nm with different lengths from 2 to 6 µm. These cantilevers were fabricated using a combination of electron-beam lithography, lift-off, and release by buffered oxide etch (BOE) followed by critical point drying (CPD). A silicon prime wafer was obtained for the structural base for the cantilevers. We cleaned the wafer in a hot piranha solution, then rinsed with deionized water and cleaned in a spin-rinse dryer. First a 400 nm layer of SiO_2 was grown onto a $\langle 100 \rangle$ silicon wafer by wet oxidation. A bilayer of PMMA was spun onto the oxidized wafer, and patterned in a Raith 150 lithographic writer using an electron beam of 10 kV with a 10 µm aperture. After development of the resist, a 5 nm Ti adhesion layer followed by a 50 nm layer of Ni–44 at.%Mo were sputtered onto the patterned resist, then lifted off by dissolving the unexposed resist in an ultrasonic acetone bath. The cantilevers were then released using a BOE of the sacrificial SiO_2 layer, followed by rinsing in two different water baths before being immersed in an IPA beaker for transfer to the critical point dryer.

2.3 Results

Figure 2.1 shows XRD scans of Ni–Mo films ranging from pure nickel to pure molybdenum in roughly 20 at.% intervals. As expected, the sputter-deposited pure nickel film has a face-centred cubic (fcc) crystal structure much like bulk nickel. As molybdenum is added to nickel it in remains in substitutional solid solution in the nickel fcc lattice, up until 23 at.% nickel. Further addition of Mo results in a fundamental change in the Ni–Mo microstructure, as seen in figure 2.1: the scans of Ni–34 at.%Mo through Ni–69 at.%Mo show a single broad peak at $2\theta \sim 44°$. The presence of a single broad peak indicates the presence of a significant amount of short- to medium-range order, which is typically associated with an amorphous microstructure. The exact microstructure is difficult to determine through XRD, since the spectra of purely amorphous, amorphous-nanocrystalline, or highly textured Ni–Mo nanocrystallites can be

very similar when investigated using Cu $K\alpha$ radiation; therefore, TEM was used to characterize the microstructure of Ni–44 at.%Mo in greater detail. Figure 2.2 is a cross-sectional HRTEM image of a Ni–44 at.%Mo film, and it

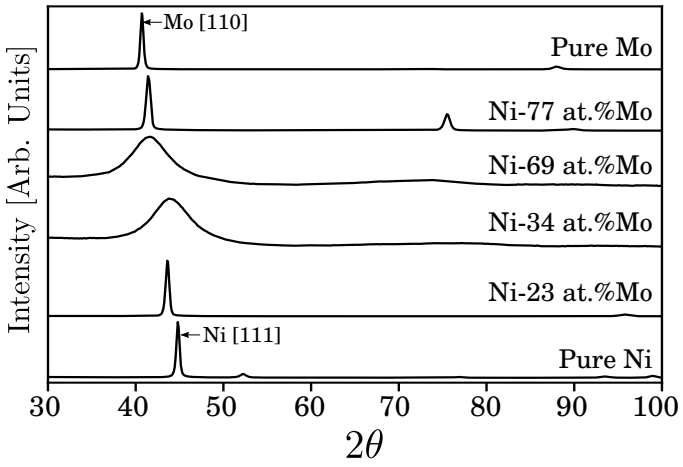

Figure 2.1: $\theta/2\theta$ diffractograms of 1 µm thick Ni–Mo thin films. A transition from crystalline to amorphous microstructure occurs between Ni–23 at.%Mo and Ni–34at.%Mo, and back to crystalline at Ni–77 at%Mo.

reveals the presence of very small nanocrystallites embedded in the amorphous matrix. We found that the nanocrystallites were bodycentered cubic (bcc) and exhibited a strong {110} orientation relative to the substrate normal. Crystallite sizes ranged from 2 to 6 nm and were all roughly equiaxed. Finally, as Mo is added beyond 69 at.% we find that the nickel goes into substitutional solid solution in the bcc molybdenum matrix.

The resistivity of Ni–Mo films as a function of Mo content is shown in figure 2.3. As molybdenum is added to nickel, which has a measured resistivity of 14 µΩcm, there is an order of magnitude increase in resistivity, reaching a maximum of 125 µΩcm at Ni–34 at.%Mo. Despite significant change in microstructure, we see that Ni–Mo films remain metallically conductive at all compositions.

The variation of global root mean square (RMS) surface roughness of 1.5 µm thick films as a function of molybdenum content is shown in figure 2.4. At low solute concentrations we observe roughness on the order of 10 nm, with

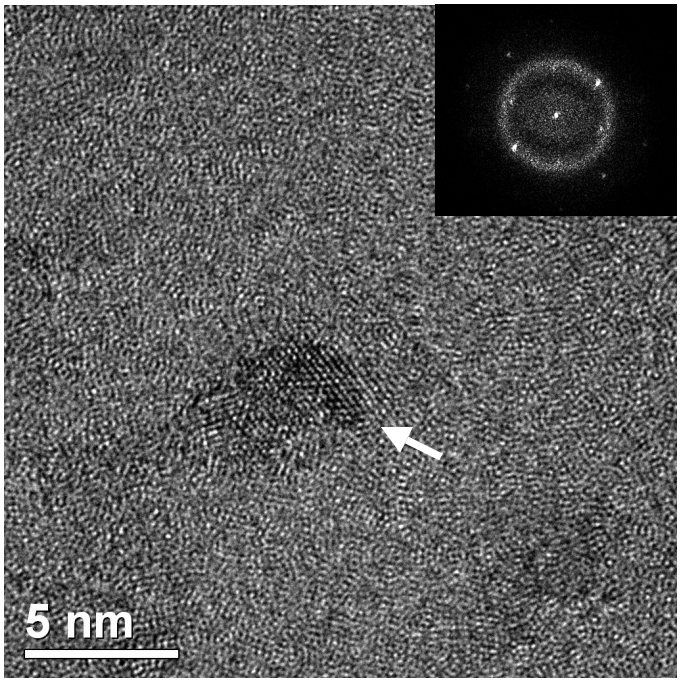

Figure 2.2: Cross–sectional HRTEM image of a Ni–44 at.%Mo film. The image shows a single nanocrystallite (indicated by white arrow) imbedded in the amorphous matrix. The inset is the corresponding digital diffractogram.

a slight decrease in roughness as further solute is added. Within the interval of Ni–34 at.%Mo to Ni–69 at.%Mo there is a fundamentally different type of surface evolution and roughening mechanism, since the roughness decreases by an order of magnitude to the sub-nanometer regime. Once the Mo content is increased beyond 69 at.% the roughness sharply increases by an order of magnitude. Comparison of figure 2.4 to figure 2.1 clearly reveals that films possessing crystalline microstructures have rough surfaces, while those of amorphous microstructures have smooth surfaces.

To further identify the ideal composition for Ni–Mo NEMS the mechanical properties were measured. We found the hardness of pure nickel to be 4.5 GPa, which agrees well with literature results of pure nickel thin films [30]. As further Mo is added there is a moderate increase in hardness, which is attributed to solid solution hardening [31]. The amorphous- nanocrystalline

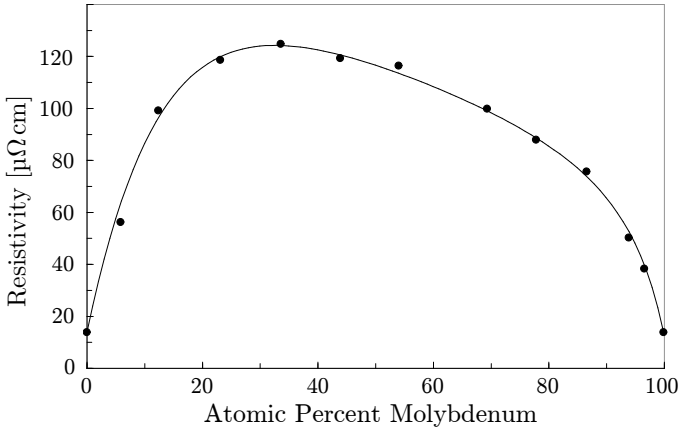

Figure 2.3: Measured electrical resistivities of 1 m thick NiMo thin films (•). Best fit of equation 2.4.6 to experimental resistivities (solid line).

films (Ni–34 at.%Mo to Ni–69 at.%Mo) exhibit significantly higher hardness when compared to their polycrystalline counterparts, increasing from 6 GPa (Ni–23 at.%Mo) to a maximum of 11 GPa (Ni–44 at.%Mo). The relatively large increase in hardness is consistent with the increased hardness reported for thin-film metallic glasses [32] when compared to conventional polycrystalline thin metal films. The greatly improved hardness of the amorphous-nanocrystalline films is desirable if they are to be used as structural components for NEMS cantilevers, since plastic deformation during resonance is obviously undesirable. Also the modulus of elasticity of Ni–44 at.%Mo was determined to be 200 ± 17 GPa.

From these characterization results we found that Ni– 44 at%Mo was an ideal candidate to be used for the fabrication of resonating NEMS cantilevers. It exhibits near atomic smoothness, metallic conductivity, and greatly improved hardness. Figure 2.5 shows a scanning electron microscopy (SEM) micrograph of a 50 nm thick fully released singly clamped Ni–44 at.%Mo cantilever. We see that the cantilever is both extremely smooth and uncurled. Stress-free metallic cantilevers such as these have obvious potential in force sensing or scanning probe microscopy applications. The need for a metallization layer, which results in degraded quality factor and a rough surface, is eliminated.

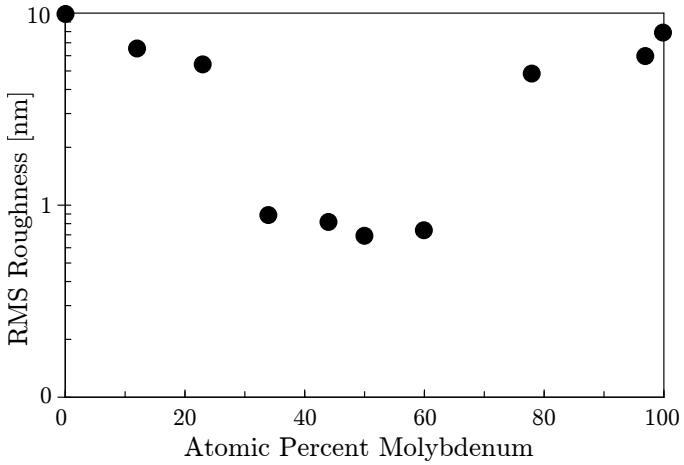

Figure 2.4: RMS roughnesses of 1 µm thick Ni–Mo thin films.

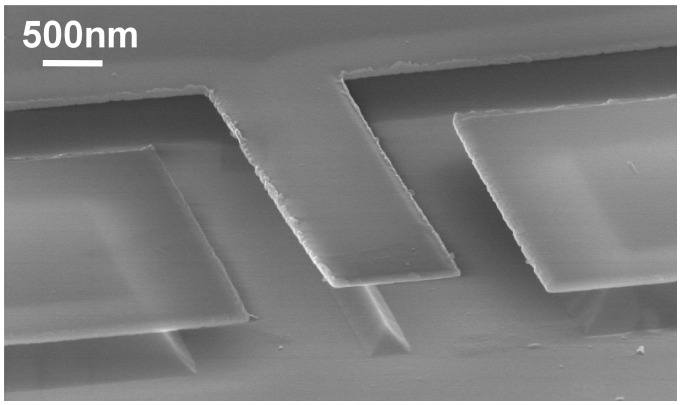

Figure 2.5: SEM micrograph of a fully released 50 nm thick NEMS cantilever fabricated from Ni–44 at.%Mo.

The resonance properties of these cantilevers were characterized using an optical method described by Carr et al [33]. The first-order resonant frequency mode of a singly clamped beam is given as

$$f_0 = \frac{t}{2\pi(0.98)(L+u)^2}\sqrt{\frac{E}{\rho}} \tag{2.3.1}$$

where t is the thickness, L is the length, u is the undercut, E is the modulus, ρ is the density, and f_0 is the resonant frequency. A series of cantilevers ranging in lengths of 2 to 6 µm was resonated, with a typical Lorentzian frequency

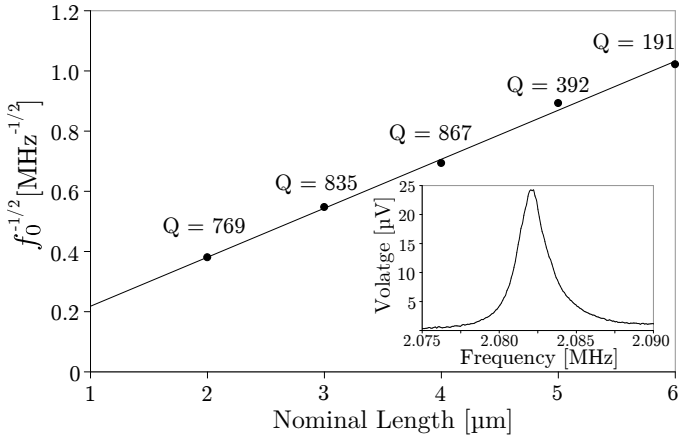

Figure 2.6: Plot of inverse square root resonance frequency versus Ni–44 at.%Mo cantilever length. The measured quality factor of each cantilever is also shown. All cantilevers are 800 nm wide and 50 nm thick. The inset is a typical resonance frequency response taken from a 4 µm long cantilever.

domain response as shown in the inset of figure 2.6. Equation 2.3.1 is linearized by plotting $1/f^{1/2}$ versus L, which is shown in figure 2.3.1. From the slope of this plot we can extract the speed of sound in Ni–44 at.%Mo, which we found to be $\nu = 4.6 \times 10^3$ m/s. Using nanoindentation the modulus was measured to be 175 GPa; therefore, using the relation $\nu = (E/\rho)^{1/2}$, the density of Ni–44 at.%Mo is found to be 9.4×10^3 kg/m^3 , which agrees very well with the rule of mixtures estimation of 9510 kg/m^3. Moreover, by extrapolating to the y-intercept, the average undercut is found to be ∼350 nm, which is in agreement with the undercut measured by SEM. Also shown in figure 2.6 are the corresponding quality factors of each cantilever, which range from 200 to 900. In many cases it has been observed that reduction in devices size results in a degradation of the quality factor [34]. Monocrystalline resonators of similar device dimensions ($\sim 10^{10}$ mm^3) are typically found to have quality factors of $\sim 10^3$, making Ni–Mo resonators comparable in performance to devices fabricated from traditional materials.

2.4 Discussion

By choosing an appropriate binary metal–metal material system we have shown that by varying the composition of elements it is possible to tune the bulk microstructure, electronic properties, and surface morphology. Most importantly, we are able to deposit film and fabricate devices that have near-atomic smoothness while maintaining metallic conductivity. It is critical to understand the origin of these material properties if we wish to tailor them for specific applications.

First we investigate the nature of electrical conduction in Ni–Mo films. As described by Bhatia [35], in the long-wavelength weak electron scattering approximation, the resistivity of a binary alloy with no superstructure can be written as the weighted sum of dynamic structure factors $S_{NN}(0)$, $S_{CC}(0)$, and $S_{NC}(0)$. These structure factors physically represent the mean square fluctuation in the number of particles in a volume V, mean square fluctuations in concentration, and correlation between fluctuation in number density and concentration, respectively. As shown by Bhatia [35], the dynamic structure factors have the following thermodynamic representations:

$$S_{CC}(0) = Nk_{\mathrm{B}}T \Bigg/ \left(\frac{\partial^2 G}{\partial c^2}\right)_{T,P,N} \tag{2.4.1}$$

$$S_{NN}(0) = (N/V)k_{\mathrm{B}}T\kappa_T + \delta^2 S_{CC}(0) \tag{2.4.2}$$

$$S_{NC}(0) = -\delta S_{CC}(0) \tag{2.4.3}$$

where N , k_{B}, T, G, c, and κ_T have their standard thermodynamic meanings. The quantity δ is known as the dilatation factor for a given composition c :

$$\delta = \frac{v_{\mathrm{Mo}} - v_{\mathrm{Ni}}}{(1-x)v_{\mathrm{Mo}} + xv_{\mathrm{Ni}}} \tag{2.4.4}$$

where v_{Mo} and v_{Ni} are the respective molar volumes. The differences in molar volume of Ni and Mo are such that the dilatation factor is small, $\delta < 0.42 \ll 1$ 1, and can be safely neglected when calculating the resistivity. Furthermore,

it has been shown by Singh and Sommer [36] that the isothermal compressibility T obeys a simple rule of mixtures if there is negligible volume expansion or contraction during mixing. Finally, we must determine an appropriate expression for the Gibbs free energy of mixing, where we assume a sub-regular solution model:

$$\Delta G^M = Nk_{\mathrm{B}}T[c\ln c + (1-c)\ln(1-c)] + N(A+cB)c(1-c) \qquad (2.4.5)$$

Using equations 2.4.2-2.4.5 and the previously mentioned assumptions, we obtain the final expression for the resistivity as a function of molybdenum content:

$$\rho(c) = \alpha\frac{c(1-c)}{1+2c(1-c)((B-A)-3Bc)/k_{\mathrm{B}}T} + [\rho_{\mathrm{Mo}}c + \rho_{\mathrm{Ni}}(1-c)] \qquad (2.4.6)$$

where ρ_{Mo} and ρ_{Mo} are the measured resistivities of pure molybdenum and nickel, and α is a scaling parameter. A best fit of the theoretical resistivities (equation 2.4.6) to the experimentally determined resistivities is shown in figure 2.3, which agrees excellently at all compositions. Furthermore, the best-fit coefficients, A and B, are found to be $2.5k_{\mathrm{B}}T$ and $1.2k_{\mathrm{B}}T$, respectively; the magnitudes of these coefficients are physically reasonable as they are of the order of $k_{\mathrm{B}}T$. Also, they are both negative, which is consistent with the fact the Ni– Mo has a negative deviation ($\Delta G^{\mathrm{XS}} < 0$), which is deduced from the presence of intermetallics in the equilibrium phase diagram.

From this model we arrive at the important conclusion that electrical conduction in these binary amorphous metals is dominated by solute scattering, whose rate is dependent on local atomic fluctuations in density and concentration. This mechanism of conduction gives us a physical understanding of the metallic conductivity observed in amorphous Ni–Mo. As seen in figure 2.3, the major changes in conductivity occur when the solute is still in solid solution with the host solvent crystal structure. This is because there is a dramatic increase in local concentration fluctuations as a small amount of so-

lute is added. Further addition of solute atoms results in decreasing marginal increases in local concentration fluctuations until a maximum is reached. This is due to the statistics of random mixing and additional reduction in concentration fluctuations due to the interaction characteristics between Ni and Mo atoms, which results in metallic conductivity across all compositions.

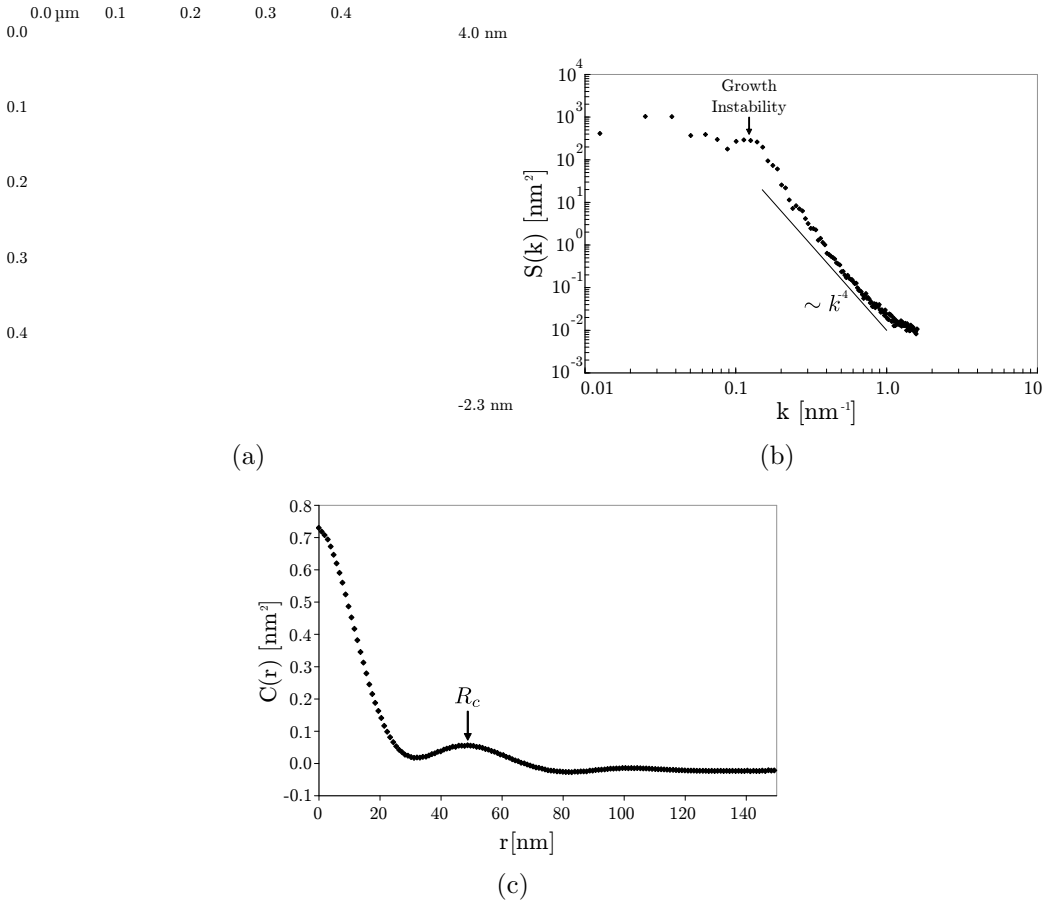

Figure 2.7: AFM height map of 1 µm thick Ni–44 at.%Mo film (a). Corresponding structure factor (b) and height–height correlation function (c) of the AFM height map in (a).

Next we must investigate the possible mechanisms that dominate the growth of amorphous Ni–Mo films, which give rise to sub-nanometer roughness. Due to the local radially isotropic nature of films that condense into the amorphous state, it has been found that their evolution is accurately described by the

well-established phenomenological continuum approach [37, 38]. This method describes the film growth based on the following non-linear Langevin-type stochastic partial differential equation:

$$\frac{\partial h(\mathbf{x},t)}{\partial t} = F[h, \nabla h] + U + \eta(\mathbf{x},t) \tag{2.4.7}$$

where $h(\mathbf{x},t)$ is the height of the film surface at position $\mathbf{x}$ and time t, U is the deposition rate, $F[h, \nabla h]$ is a functional of the local spatial derivatives of h, and $\eta(\mathbf{x},t)$ is uncorrelated white Gaussian noise, where $\langle \eta(\mathbf{x},t) \rangle = 0$ and $\langle \eta(\mathbf{x},t)\eta(\mathbf{x}',t') \rangle = 2D\delta^2(x-x')\delta(t-t')$. As shown by [39], the early to intermediate stages of thin-film metallic growth are accurately described by the following relation mechanisms:

$$\frac{\partial h(\mathbf{x},t)}{\partial t} = -D_s \nabla^4 h - S\nabla^2 h + U + \eta(\mathbf{x},t) \tag{2.4.8}$$

where the $\nabla^4 h$ term is due to curvature-induced surface diffusion [40], and Ds is the surface diffusivity. The $\nabla^2 h$ term is due to self-shadowing, due to the non-zero interaction distance between surface atoms and incident atoms [41, 42]. Equation 2.4.8 is solved by Fourier methods, yielding

$$S(k) = \langle |z(k,t)|^2 \rangle = \frac{D_s}{D_s k^4 - S k^2}[1 - \exp\left(-2(D_s k^4 - S k^2)t\right)] \tag{2.4.9}$$

where $z(x,t) = h(x,t) - \langle h(t) \rangle$, and k denotes the magnitude of the Fourier-conjugated wavevector in space. Using the AFM topograph of a 1 m thick Ni–44 at%Mo film (figure 2.7(a)), the structure factor, $S(k)$, is calculated via angular integration of the squared magnitude of the Fourier transform of the AFM height map, and is shown in figure 2.7(b). Upon inspection of equation 2.4.9 we see that the structure factor exhibits a k^4 dependence at large wavevectors. The experimentally measured structure factor clearly exhibits a k^4 dependence at large wavevectors, which further substantiates the validity of this approach. Moreover, analysis of equation 2.4.9 reveals the presence

of a growth instability, where the critical wavemode, $k_c = (S/2D_s)^{0.5}$, grows without bound. The correlation length R_c, which is the mean characteristic length of topological domains on the surface, is taken to be the distance to the first maximum of the height-height correlation function

$$\begin{aligned} C(r,t) &= \langle z(\mathbf{r}+\mathbf{r}')z(\mathbf{r})\rangle_{r=|\mathbf{r}|} \\ &= \tfrac{D_s}{2\pi}\int_0^\infty \tfrac{k}{D_s k^4 - S k^2}[1-\exp\left(-2(D_s k^4 - S k^2)t\right)]J_0(kr)\,dk \end{aligned} \tag{2.4.10}$$

where $J_0(kr)$ is a Bessel function of the first kind. Due to the unstable wavemode k_c, the topological features of the surface are dominated by the wavelength $\lambda_c = 2\pi/k_c$, resulting in a correlation length of $R_c = 7.0156/k_c$. The height–height correlation function of the AFM topograph in figure 2.7(a) is shown in figure 2.7(c), where the correlation length is found to be $R_c = 49$ nm. This gives us a hint to the origin of the extremely smooth surfaces of these amorphous films.

Using the measured correlation length we can estimate the ratio of the surface diffusion coefficient to the self–shadowing coefficient, $D_s/S \sim 24$. Therefore, we see that surface diffusion is significantly greater than the self-shadowing effect, which results in a very weak growth instability. This in turn is the primary roughening mechanism in amorphous film growth. As seen in figure 2.7(b), a weak maximum at $k_c \sim 0.12\text{nm}^{-1}$ is present in the structure factor, which agrees well with the predicted value of $k_c = 0.14\text{nm}^1$ from the measured correlation length of 49 nm. This result is in contrast to the roughnesses reported for evaporated Zr–based amorphous thin films, where an RMS roughness of ~ 2 and a D_s/S ratio of 3.9 is measured for a 480 nm thick film. The reason for the enhanced smoothness of sputtered versus evaporated amorphous thin films, as proposed by Mayr *et al* [43], is due to the significantly greater thermal energy of sputtered incident adatoms. This results in greater surface adatom mobility and consequently smoother films.

2.5 Conclusions

In this study we co-sputtered Ni–Mo thin films at roughly 10 at.% intervals. Using XRD and TEM it was shown that the equilibrium solubility could be surpassed, achieving a maximum solubility of Ni–23 at.%Mo. Compositions ranging from Ni–34 at.%Mo to Ni–69 at.%Mo were shown to exhibit an amorphous–nanocrystalline microstructure. These films were shown to possess excellent mechanical and physical properties. In particular, Ni–44 at.%Mo shows a nanoindentation hardness of 11 GPa (compared to 4.5 GPa of pure Ni), metallic conductivity of 125 μΩcm, and RMS surface roughness of 0.8 nm. Using a sub–regular solution model it was shown that the electrical conductivity of Ni–Mo is in excellent agreement with Bhatias structural model of electrical resistivity in binary alloys. Moreover, the best- fit sub-regular solution model is physically consistent with the thermodynamics of Ni–Mo since it shows a negative deviation. The morphological evolution of amorphous Ni–Mo is modeled using a Langevin-type stochastic rate equation. Roughening of amorphous thin films is primarily due to a growth instability, which is due to the competing processes of surface diffusion and self-shadowing. Due to the high thermal energies of sputtering, the growth instability in Ni–44 at.%Mo is strongly damped, resulting in sub-nanometer roughness.

Resonant NEMS cantilevers, possessing excellent mechanical and physical properties, were fabricated from Ni–44 at.%Mo. Owing to their amorphous microstructure, these cantilevers lacked significant residual stresses gradients, allowing for the fabrication of uncurled metallic cantilevers. Ni–44 at.%Mo cantilevers having a thickness of 50 nm (5 nm Ti adhesion) at widths of 400 and 800 nm with different lengths from 2 to 6 μm had MHz resonant frequencies and quality factors ranging from 200 to 900.

References

[1] G. Binnig, C. F. Quate, and Ch Gerber. Atomic force microscope. *Phys. Rev. Lett.*, 56(9):930, 1986.

[2] D. Rugar and P. Hansma. Atomic force microscopy. *Phys. Today*, 43(10):23, 1990.

[3] B. Ilic, H. G. Craighead, S. Krylov, W. Senaratne, C. Ober, and P. Neuzil. Attogram detection using nanoelectromechanical oscillators. *J. Appl. Phys.*, 95 (7):3694, 2004.

[4] J. J. Gill, D. T. Chang, L. A. Momoda, and G. P. Carman. Manufacturing issues of thin film niti microwrapper. *Sens. Actuators, A*, 93(2):148, 2001.

[5] H. D. Tong, F. C. Gielens, J. G. E. Gardeniers, H. V. Jansen, J. W. Berenschot, M. J. de Boer, J. H. de Boer, C. J. M. van Rijn, and M. C. Elwenspoek. Microsieve supporting palladium-silver alloy membrane and application to hydrogen separation. *J. Microelectromech. Syst.*, 14(1):113, 2005.

[6] M. Gupta, V. K. Rathi, R. Thangaraj, O. P. Agnihotri, and K. S. Chari. The preparation, properties and applications of silicon nitride thin films deposited by plasma-enhanced chemical vapor deposition. *Thin Solid Films*, 204(1):77, 1991.

[7] Farooqui M. M. and Evans A.G.R. Silicon sensors with integral tips for atomic force microscopy: a novel single-mask fabrication process. *J. Micromech. Microeng.*, 3:8, 1993.

[8] A. Folch, M. S. Wrighton, and M. A. Schmidt. Microfabrication of oxidation-sharpened silicon tips on silicon nitride cantilevers for atomic force microscopy. *J. Microelectromech. Syst.*, 6(4):303, 1997.

[9] G. Suchaneck, V. Norkus, and G. Gerlach. Low-temperatute pecvd-deposited silicon nitride thin films for sensor applications. *Surf. Coat. Technol.*, 142:808, 2001.

[10] T. Yi and C. Kim. Measurement of mechanical properties for mems materials. *Meas. Sci. Technol.*, 10(8):706, 1999.

[11] Z. Lee, C. Ophus, L. M. Fischer, N. Nelson-Fitzpatrick, K. L. Westra, S. Evoy, V. Radmilovic, U. Dahmen, and D. Mitlin. Metallic nems components fabricated from nanocomposite al-mo films. *Nanotechnology*, 17(12):3063, 2006.

[12] A. Chand, M. B. Viani, T. E. Schffer, and P. K. Hansma. Microfabricated small metal cantilevers with silicon tip for atomic force microscopy. *J. Microelectromech. Syst.*, 9(1):112, 2000.

[13] C. V. Thompson and R. Carel. Stress and grain growth in thin films. *J. Mech. Phys. Solids*, 44(5):657, 1996.

[14] S. Huang and X. Zhang. Gradient residual stress induced elastic deformation of multilayer mems structures. *Sens. Actuators, A*, 134(1):177, 2007.

[15] T. Du, A. Vijayakumar, K. B. Sundaram, and V. Desai. Chemical mechanical polishing of nickel for applications in mems devices. *Microelectron. Eng.*, 75 (2):234, 2004.

[16] R. A. Mirshams and P. Parakala. Nanoindentation of nanocrystalline ni with geometrically different indenters. *Mater. Sci. Eng., A*, 372(1):252, 2004.

[17] M. Hebbachi. Nanoindentation: Hardness and phase transition in silicon. *Mater. Sci. Eng., A*, 387(1):743, 2004.

[18] Y. Yang, B. I. Imasogie, S. M. Allameh, B. Boyce, K. Lian, J. Lou, and W. O. Soboyejo. Mechanisms of fatigue in liga ni mems thin films. *Mater. Sci. Eng., A*, 444(1):39, 2007.

[19] K. Kataoka, S. Kawamura, T. Itoh, K. Ishikawa, H. Honma, and T. Suga. Electroplating ni micro-cantilevers for low contact-force ic probing. *Sens. Actuators, A*, 103(1):116, 2003.

[20] W. H. Teh, J. K. Luo, M. A. Graham, A. Pavlov, and C. G. Smith. Near-zero curvature fabrication of miniaturized micromechanical ni switches using electron beam cross-linked pmma. *J. Micromech. Microeng.*, 13(5):591, 2003.

[21] T. Egami. Atomistic mechanism of bulk metallic glass formation. *J. Non-Cryst. Solids*, 317(1):30, 2003.

[22] L. Battezzati and M. Baricco. An analysis of volume effects in metallic-glass formation. *J. Less Common Met.*, 145(1):31, 1998.

[23] A. Inoue and N. Nishiyama. *Mater. Sci. Eng. A*, 401:226, 1997.

[24] O. N. Senkov and D. B. Miracle. Effect of the atomic size distribution on glass forming ability of amorphous metallic alloys. *Mater. Res. Bull.*, 36(12):2183, 2001.

[25] T. B. Massalski. *Binary Alloy Phase Diagrams*, 1990.

[26] B. Zhao, F. Zeng, and F. Pan. Formation of metastable alloy films in the ni-mo binary system by ion-beam-assisted deposition. *Appl. Phys. A*, 77(3):523, 2003.

[27] W. Zhang, X. Zhang, D. Yang, and Q. Xue. Sliding wear study of ion-beam mixing ni-mo multilayer films on steel. *Wear*, 197(1):228, 1996.

[28] W Klement, R. H. Willens, and P. Duwez. Non-crystalline structure in solidified gold-silicon alloys. *Nature*, 187(4740):869, 1960.

[29] T. Egami. Formation and deformation of metallic glasses: Atomistic theory. *Intermetallics*, 14(8):882, 2006.

[30] U. Erb. Electrodeposited nanocrystals: Synthesis, properties and industrial applications. *Nanostruct. Mater.*, 6(5):533, 1995.

[31] R. Labusch. A statistical theory of solid solution hardening. *Phys. Status Solidi A*, 41:659, 1970.

[32] Y. Liu, S. Hata, K. Wada, and A. Shimokohbe. Thermal, mechanical and electrical properties of pd-based thin-film metallic glass. *Jpn. J. Appl. Phys., Part 1*, 40(9):5382, 2001.

[33] D. W. Carr, S. Evoy, L. Sekaric, H. G. Craighead, and J. M. Parpia. Measurement of mechanical resonance and losses in nanometer scale silicon wires. *Appl. Phys. Lett.*, 75(7):920, 1999.

[34] K. L. Ekinci and M. L. Roukes. Nanoelectromechanical systems. *Rev. Sci. Instrum.*, 76(6), 2005.

[35] A. B. Bhatia and D. E. Thornton. Structural aspects of the electrical resistivity of binary alloys. *Phys. Rev. B*, 2(8):3004, 1970.

[36] R. N. Singh and F. Sommer. Temperature dependence of the thermodynamic functions of strongly interacting liquid alloys. *J. Phys. Condens. Matter*, 4(24): 5345, 1992.

[37] J. Villain. Continuum models of crystal growth from atomic beams with and without desorption. *J. Physique I*, 1:19, 1991.

[38] M. Kardar, G. Parisi, and Y. Zhang. Dynamic scaling of growing interfaces. *Phys. Rev. Lett.*, 56(9):889, 1986.

[39] M. Raible, S. G. Mayr, S. J. Linz, M. Moske, P. Hnggi, and K. Samwer. Amorphous thin-film growth: Theory compared with experiment. *Europhys. Lett.*, 50(1):61, 2000.

[40] W. W. Mullins. Theory of thermal grooving. *J. Appl. Phys.*, 28(3):333, 1957.

[41] A. Mazor, D. J. Srolovitz, P. S. Hagan, and B. G. Bukiet. Columnar growth in thin films. *Phys. Rev. Lett.*, 60(5):424, 1988.

[42] S. Van Dijken, L. C. Jorritsma, and B. Poelsema. Steering-enhanced roughening during metal deposition at grazing incidence. *Phys. Rev. Lett.*, 82(20):4038, 1999.

[43] S. G. Mayr and K. Samwer. Tailoring the surface morphology of amorphous thin films by appropriately chosen deposition conditions. *J. Appl. Phys.*, 91(5): 2779, 2002.

3

All-metal AFM probes fabricated from microstructurally tailored Cu-Hf thin films *

3.1 Introduction

Since the inception of the atomic force microscope (AFM) [1], its versatility and usefulness as a characterization, measurement, and fabrication tool has exploded beyond simple topographic imaging. Currently AFM probes are typically made from Si [2], SiO_2 and Si_3N_4 [3]. These Si based materials are so ubiquitously used since they are elastically stiff, very hard and easy to process. Unfortunately these materials possess low electrical conductivity and poor optical reflectivity. An increasing number of applications make use optically reflective cantilevers and electrically or thermally conducting tips, which is typically accomplished by coating the AFM probe with a metal layer. Despite providing the desired optical, thermal, or electrical properties, metal coatings produce adverse side–effects.

The extremely high spatial resolution of the AFM is what makes it such a unique and useful tool. Important technological applications that make use of the high spatial resolution of a conductive AFM tip are: conductive atomic force microscopy (C–AFM) [4], thermomechanical data storage [5], [6], [7] elec-

*Material in this chapter has been published in:
► E. Luber, B.C. Olsen, C. Ophus, V. Radmilovic and D. Mitlin. *Nanotechnology* **20**, 345703 (2009).

trochemical nanolithography by local metal etching [8], local anodic oxidation [9], and ferroelectric data storage [10] to name just a few. A fundamental problem caused by metallization of the AFM tip is increased tip radius, resulting in a loss of spatial resolution. It is straightforward to show that the tip radius of a conformally coated parabolic tip is the sum of the coating thickness and tip radius prior to coating. Therefore, tip radius is significantly limited by the thickness of the metallization layer, which typically made to a minimum thickness of 15–20 nm [8] simply to ensure film continuity. This problem is further compounded by wear of the metal coating.

It has recently been shown [4] that after acquiring just a few C-AFM maps, wear of the tip coating produces significant artifacts which are often quite difficult to detect. Wear of metal coated AFM tips is also particularly important in SPM based recording technologies, such as ferroelectric data storage [10],[11], which promises ultrahigh areal data density. Increasing the thickness of the deposited metal layer is not a viable solution to increasing probe lifetime, as the tip radius become significantly larger and stresses in the metal layer can induce significant bending of the cantilever, to the extent that alignment in the AFM system becomes impossible [12].

As shown by Birkelund et. al.[12] the use of all–metal probes for AFM nanolithography resulted in a 10–fold increase in lifetime compared to conventional titanium coated silicon nitride cantilevers. This large enhancement in device lifetime was a result of maintaining conductivity despite continuous wear of the tip. These probes were fabricated by a combination of silicon micromachining and electroforming, resulting in nickel probes with a gold coating. Due to the bilayer nature of these probes they are still suspectable to thermal mismatch bending [13]. Other authors have fabricated single–layer all–metal AFM cantilevers [14], but are limited to metals that can be electroplated, with nickel often being the material of choice. Moreover, these cantilever are often made to be very stiff (low force sensitivity, thickness > 4 µm) to avoid excessive cantilever bending due to residual stress gradients that can develop during film growth. Chand et. al. reported a process for the fabrication of high resonant

frequency and force sensitivity bilayer Au/Ti cantilevers with an integrated silicon tip [15]. The combination of high resonant frequency and force sensitivity was achieved by reducing the cantilever dimensions (13–40 µm long, and 100–160µm thick). These cantilevers were unusably bent upon initial release due to residual stress gradients caused by competitive grain growth, but the devices were straightened using rapid thermal annealing. Unfortunately this process only produced a 60% device yield.

All–metal AFM probes consisting of a single material will have tip radii limited by the fabrication procedure, possess superior device lifetime (independent of tip radii), and be immune to thermal expansion mismatch bending. In previous work [16], [17], we have shown that uncurled metal cantilevers can be fabricated from thin film metallic glasses. The uncurled nature of the cantilevers was attributed to the lack of grains and consequent differential stress induced by grain size gradients throughout the film thickness. Due to the specific thermodynamic properties of the alloys used, large solute content was needed in order to achieve the desired amorphous microstructure, which resulted in an undesirable loss in electrical conductivity [16], [17]. Moreover, chemical etching of these films proved difficult due to the high solute content, limiting fabrication to small thicknesses using a lift–off process. For these reasons we investigate the Cu–Hf system, since Cu-Hf is capable of forming glassy alloys in the bulk [18]. As expected, the range of amorphous compositions was much broader when it was deposited as a thin film, as it is vapour quenched during deposition. Also, since the best glass former is on the copper rich side, vapour quenching resulted in glassy films at very low hafnium concentrations.

The aim of this study is to design a thin film alloy to be used for the fabrication of all–metal AFM probes that can be fabricated to arbitrary size and geometry from a single structural material that posses metallic conductivity and reflectivity, and improved device lifetime. Our approach to meet these design constraints is by selecting a suitable alloy system and then tuning the composition for optimal material properties. The thin film alloy system chosen in this study is Cu–Hf, which has yet to be reported in literature to date,

therefore it was necessary to perform a systematic investigation of the Cu–Hf system in order to determine the optimal alloy composition to be used for the fabrication of all–metal AFM probes.

Cu–Hf films were characterized using x–ray diffraction (XRD), nanoindentation, four–point probe, and *in–situ* multi–beam optical stress sensing (MOSS). Metallic glass $Cu_{90}Hf_{10}$ films are found to posses an optimal combination of electrical resistivity (96 $\mu\Omega$cm), nanoindentation hardness (5.2 GPa), ductility, and incremental stress. Subsequently, a microfabrication process was developed to create $Cu_{90}Hf_{10}$ AFM probes. Uncurled, 1 µm thick cantilevers having lengths of 100–400 µm are fabricated, with tip radii ranging from 10–40 nm. As a proof of principle, these all–metal Cu–Hf AFM probes are mounted in a commercial AFM and used to successfully image a known test structure.

3.2 Experimental procedure

We deposited 1 µm nominally thick Cu-Hf films onto 4-inch (100) naturally oxidized silicon wafers using a DC-magnetron co-sputtering system (AJA International). Prior to sputtering the wafers were cleaned using a 3:1 mixture of 51% H_2SO_4 and 30% H_2O_2. Argon sputtering was maintained at 4.0 mTorr with base pressures of $\approx 2.0 \times 10^{-8}$ Torr, while substrate temperature was maintained at 18 °C. Deposition was done in a sputter-up configuration with continuous substrate rotation to ensure film uniformity. Films were deposited in roughly 10 at.% intervals. Film compositions were confirmed using electron dispersed spectroscopy (EDAX) mounted on a Hitachi S3000N SEM.

Electrical resistivity of the films are calculated by measuring the sheet resistance using a linear four point probe. Mechanical properties of the films were measured using a commercially available nanoindentation load-depth sensing instrument (Hysitron TriboIndenter), equipped with an AFM. All the tests were performed under identical conditions, using a Berkovich indenter tip and a target indentation depth of 100 nm. Each data point represents an average

value of 25 individual indentations; all indentations were separated by about 25 µm. The hardnesses and reduced moduli are determined from the load-depth curve using the method of Oliver and Pharr [19].

Evolution of film stress, was determined using an *in–situ* MOSS system [20]. The MOSS system used for the *in–situ* measurement of substrate curvature, was a commercial k–Space Associates Inc., attachment to the sputter system, which uses a 50 mW AlGaInP laser. Prior to deposition a flat reference of 25 data points was collected.

Film microstructure was analyzed using XRD, which was performed using a Bruker AXS D8 Discover diffractometer with a GADDS area detector was used. A Cu $K\alpha$ radiation source ($\lambda = 1.54056$ Å) collected the x-ray scans from a sample mounted on a two-axis rotation stage that also allowed for XYZ translation.

3.3 Material properties

3.3.1 Microstructure

Shown in figure 4.9 are the XRD curves of 1 µm thick Cu-Hf thin films ranging from pure Cu to pure Hf. As expected, the sputter-deposited pure copper film has a face-centered cubic (fcc) crystal structure and has ⟨111⟩ fibre texture normal to the substrate plane. Even small additions of hafnium results in a fundamental change in the microstructure; the XRD curves of $Cu_{90}Hf_{10}$ through $Cu_{30}Hf_{70}$ consist of a single broad peak. The presence of a single broad peak in an XRD curve is attributed to a lack on long range order in the microstructure, which can be either amorphous, extremely nanocrystalline, or combination of both [21]. Further addition of hafnium results in films having a hexagonal close packed (hcp) crystal structure.

As expected, vapour quenching greatly increases the range of amorphous/nanocrystalline

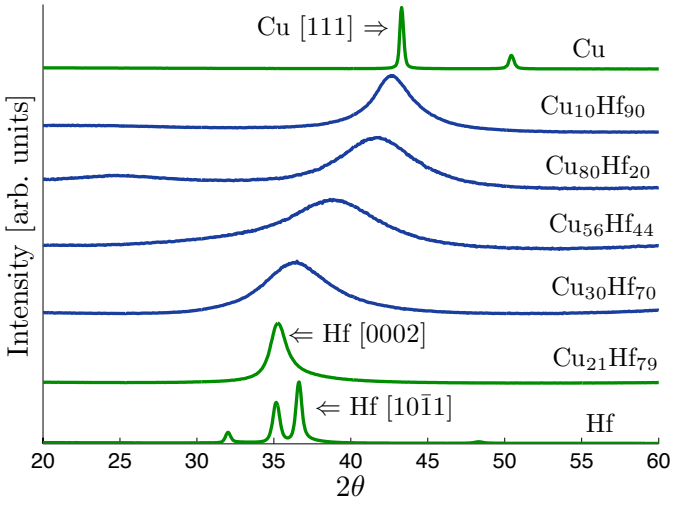

Figure 3.1: $\theta/2\theta$ XRD curves of 1 µm thick Cu–Hf films.

compositions in the Cu–Hf system [18], spanning ≈ 70 at.%. Determination of the exact structure of the alloys in this composition range requires the use of higher spatial resolution methods such synchrotron XRD coupled with reverse Monte Carlo simulation [22], due to the lack of any long range structure. Nonetheless, if any crystallites are present their size can be estimated using the Scherrer equation [23], which predicts the average crystallite size in $Cu_{90}Hf_{10}$ to be 2.5 nm in diameter. At higher hafnium concentration the Scherrer equation predicts average crystallite sizes less than 1.5 nm. This is a thermodynamically unlikely situation, and we can safely conclude that the structure in the composition range of $Cu_{90}Hf_{10}$ – $Cu_{30}Hf_{70}$ is largely amorphous. Therefore, these films can be thought to be homogenous throughout the film thickness, which is critical if uncurled AFM probes are to be fabricated for arbitrary geometries.

3.3.2 Electrical conductivity

The resistivity of Cu-Hf films as a function of hafnium concentration is shown in figure 3.2. As hafnium is added to copper, which has a measured resistivity of 2.5 $\mu\Omega$cm, the resistivity increases to a maximum of 194 $\mu\Omega$cm at $Cu_{42}Hf_{58}$.

Despite the order of magnitude increase in resistivity all film compositions remain metallically conductive.

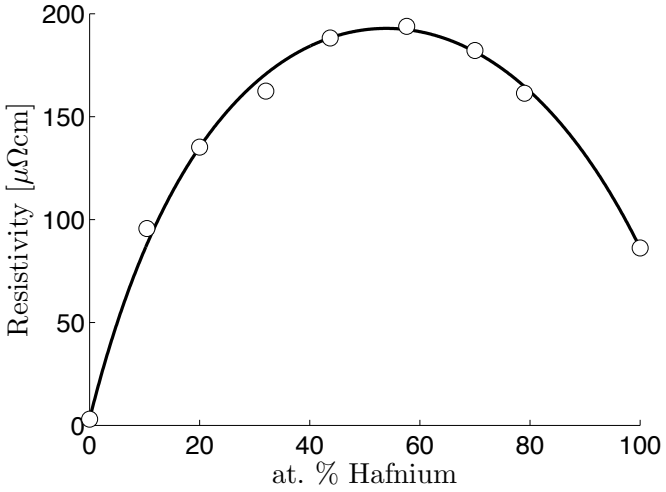

Figure 3.2: Measured electrical resistivity of 1 µm thick Cu-Hf thin films (◯). Best fit of equation 3.3.6 to the experimental resistivities (solid line).

Understanding the nature of electrical conduction in these Cu-Hf thin films is of significant interest, since it will guide our selection of optimal alloy composition, and future alloy design. As described by Bhatia and Thornton [24], in the long wavelength weak electron scattering approximation, the resistivity of a binary alloy with no superstructure is proportional to the sum of dynamic structure factors $S_{NN}(0)$, $S_{CC}(0)$, and $S_{NC}(0)$. These structure factors physically represent the mean square fluctuation in the number of particles in a volume V, mean square fluctuations in concentration, and correlation between fluctuation in number density and concentration respectively. From thermodynamic arguments it can be shown [24] that

$$S_{CC}(0) = nRT \Big/ \left(\frac{\partial^2 G}{\partial c^2}\right)_{T,P,n} \tag{3.3.1}$$

$$S_{NN}(0) = \frac{n}{V} RT\kappa_T + \delta^2 S_{CC}(0) \tag{3.3.2}$$

$$S_{NC}(0) = -\delta S_{CC}(0) \tag{3.3.3}$$

where n is the number of moles, R is the ideal gas constant, T is the absolute temperature, G is the Gibbs free energy, P is the pressure, V is the volume, and δ is the dilatation factor defined by,

$$\delta = \frac{v_A - v_B}{(1-x)v_A + xv_B} \tag{3.3.4}$$

where v_A and v_B are the partial molar volumes per atom of species A and B, and x is the concentration of species B. As shown by Singh and Sommer [25] the isothermal compressibility κ_T obeys a simple rule of mixtures if there is negligible volume expansion or contraction during mixing. Since the molar volumes of Cu and Hf are significantly different, the dilatation factor is on the order of unity and cannot be neglected. In such a case, it can be shown [24] that

$$S_{CC}(0) = \frac{x(1-x)}{1 + x(1-x)(\delta^2 + \frac{d^2 g(x)}{dx^2}/RT)} \tag{3.3.5}$$

where $g(x)$ is the excess Gibbs free energy of mixing.

Therefore to determine the resistivity, we must select an appropriate expression for the Gibbs free energy of mixing. Consistent with CALPHAD modeling of the Cu–Hf system [26] we assume a regular solution model, $g(x) = M_0 x(1-x)$, where M_0 is the binary interaction parameter. Substituting this expression into equation 3.3.5, and combining equations 3.3.2-3.3.3, we arrive at the following expression for the resistivity as a function of hafnium content x,

$$\rho(x) = K(1 - \delta + \delta^2)\frac{x(1-x)}{1 + x(1-x)(\delta^2 - 2M_0/RT)} + (1-x)\rho_{\mathrm{Cu}} + x\rho_{\mathrm{Hf}} \tag{3.3.6}$$

where K is a scaling constant. Despite the complex nature of equation 3.3.6, the shape of the resistivity vs. composition curve is entirely determined by a single parameter, which is the so-called 'alpha value' for regular solutions $\alpha = M_0/RT$. Shown in figure 3.2 is the best fit of equation 3.3.6 to the experimentally determined resistivities. The best–fit parameters to this non–linear equation are determined using a Monte Carlo L_1 norm minimization routine, yielding parameteres of $\alpha = -0.30$ and $K = 369$ $\mu\Omega$cm. Of noteworthy im-

portance is both the magnitude and sign of α. Firstly, it is on the order of unity, which is the correct order of magnitude for real systems. Secondly, it is negative, which must be the case since the Cu-Hf system has a negative deviation [26]. Having used only one fitting parameter to achieve an excellent fit for all data points, and having a physically interpretable and realistic value for the fitting parameter strongly underscores the validity of the above method of modeling the electrical conductance in Cu-Hf thin films.

From these results we see that change in electrical conductivity is strongly dominated by local fluctuations in concentration (solute scattering). The excellent agreement of this model not only confirms the disordered structure of these alloys, but underscores the importance of reducing the solute concentration if high electrical conductivity is desired.

3.3.3 Film hardness

The nanoindentation hardness of Cu–Hf films as a function of hafnium concentration is shown in figure 3.3. We see that there is a significant increase in hardness with the addition of small amounts of hafnium, with $Cu_{90}Hf_{10}$ showing a two–fold improvement over pure copper. As the hafnium content is further increased the hardness continues to increase, until a maximum hardness is reached at $Cu_{68}Hf_{32}$.

Inspection of figure 3.3 shows a compositional dependence on the hardness within the range of glassy alloys. Recently Zhang et. al.[27] have proposed a model explaining the origin of plasticity in metallic glasses, having important ramifications regarding alloy selection in this study. Motivated by the large compositional differences observed in certain metallic glasses, Zhang et. al.[27] show that atoms possessing icosahedral coordination environments are the least likely to participate in plastic flow events, since the icosahedral coordination environment has higher symmetry and packing, and more energetically stable than other coordination polyhedra. Consequently the amount of plasticity is mediated by the fraction of icosahedral coordination polyhedra.

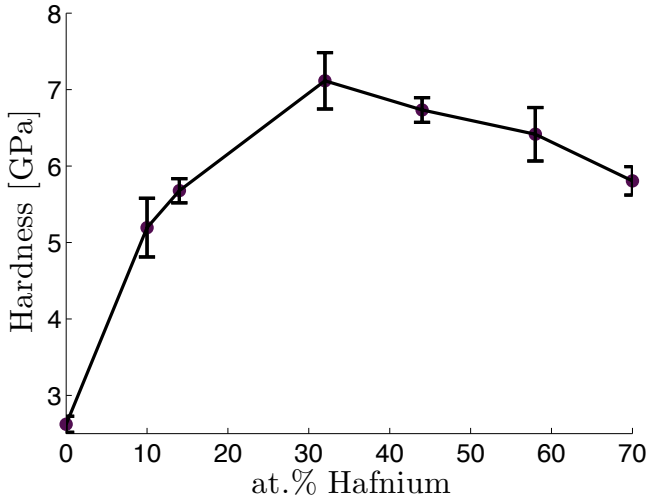

Figure 3.3: Nanoindentation hardness of 1 µm thick Cu-Hf thin films. Each data point is an average of 25 indentations, separated by $\sim$ 25 µm.

As outlined by the authors, a method for maximizing metallic glass plasticity can be accomplished by minimizing the solute concentration; when solute and solvent have significantly different atomic radii, the formation of icosahedral coordination is geometrically unfavorable at low solute concentrations. Furthermore, it is found that increased hardness and glass transition temperature correlates with decreased plasticity [27]. From this standpoint, we can understand the compositional variation of hardness observed in glassy Cu–Hf films is a result is changing coordination environments, with maximal icosahedral coordination occurring within the vicinity of $Cu_{68}Hf_{32}$. This is in excellent agreement with the maximum glass transition temperature of the bulk Cu–Hf system occurring at $Cu_{64}Hf_{36}$ [18].

3.3.4 Film stress

In–situ measurement of substrate curvature during deposition yields important information about the stress distributions in Cu–Hf films. Shown in figure 3.4 are the film force curves for Cu–Hf films. The film force curve is related to both the average stress the given by the Stoney equation, and the incremental

stress, which is the stress in the layer being added [28]. The average stress, $\langle\sigma\rangle$, is given by the slope of a line from the origin to any point on the film force curve

$$\langle\sigma\rangle = f/t \tag{3.3.7}$$

where f is the film force and t is the film thickness. The incremental stress is the slope of the film force curve

$$\sigma(t) = \frac{df}{dt} \tag{3.3.8}$$

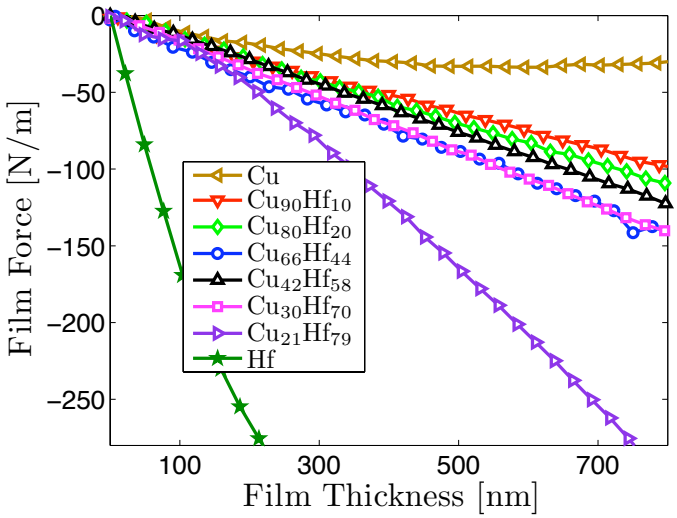

Figure 3.4: Film force evolving during deposition of Cu–Hf films.

Inspection of the film force curves shows significant differences between the crystalline Cu film and the amorphous Cu–Hf films. The amorphous films exhibit nearly linear force curves, which implies that there are no gradients in the incremental stress, i.e. the film stresses are uniform throughout the film thickness. In comparison, the slope of the Cu film force changes significantly throughout the film thickness due to the non-uniform microstructure, as a result of competitive grain growth [29]. The presence of internal stress gradients within the film will result in cantilever bending.

For a rectangular cantilever of thickness h, width W, and length L, subject to an internal axial moment M_x, it can be shown [30] that the beam will bend with a curvature of

$$\kappa_B = \frac{12M_x}{M_f W h^3} \tag{3.3.9}$$

where M_f is the biaxial film modulus, and M_x is the internal bending moment

$$M_x = \int_0^h W(t - h/2)\sigma(t)\, dt \tag{3.3.10}$$

A positive curvature indicates that the cantilever will bend away from the substrate. Now if we substitute equation 3.3.8 into equation 3.3.10 the internal bending moment is

$$M_x = W\left(\frac{h}{2}f(h) - \int_0^h f(t)\, dt\right) \tag{3.3.11}$$

Substituting this relation into equation 3.3.9 we arrive at an expression for the curvature κ_B, of a released cantilever fabricated from a film with a film force of $f(t)$

$$\kappa_B = \frac{12}{M_f h^3}\left(\frac{h}{2}f(h) - \int_0^h f(t)\, dt\right) = \frac{12}{M_f h^3} f_B \tag{3.3.12}$$

The term in brackets, f_B, has units of force, and is termed the bending force. Increased bending force results in a proportional increase in the bending of the released cantilever. Physically, as seen in equation 3.3.12, the bending force is simply the deviation from uniform stress. The bending force curves of Cu–Hf films are shown in figure 3.5.

3.4 Alloy selection

Based on the extensive characterization results of the previous section we are prepared to choose the optimal composition of Cu-Hf to be used for the fabrication of all–metal AFM probes.

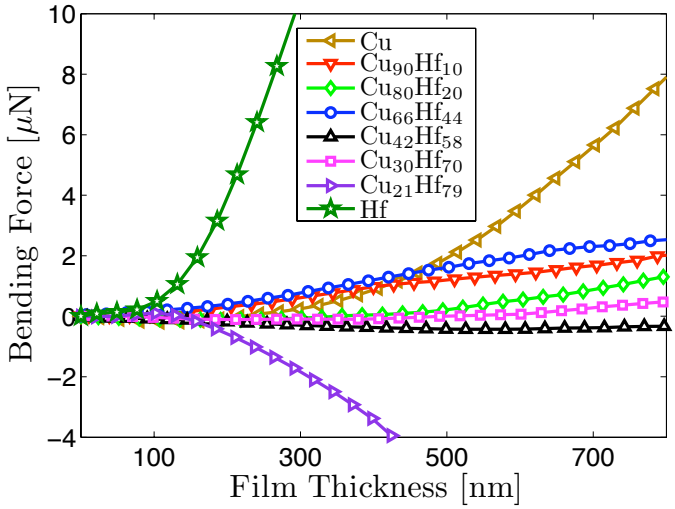

Figure 3.5: Bending force curves of Cu–Hf films. Large bending force will result in a proportionate increase in the bending of the release cantilever.

In order to fabricate probes to arbitrary size and geometry, it is necessary that the internal film stresses do not cause significant bending for a large range of lengths and thicknesses. The amount of cantilever bending, as a function of film thickness is predicted by equation 3.3.12 and plotted in figure 3.5. Inspection of figure 3.5 clearly reveals that the crystalline films (Cu, $Cu_{21}Hf_{79}$, Hf) are not suitable candidates, as the bending force curves increase rapidly and will result in unusably bent cantilevers. To confirm this prediction, pure copper cantilevers were fabricated. As seen in figure 3.6, Cu cantilevers undergo significant bending. In comparison, the bending force curves of the glassy films ($Cu_{90}Hf_{10}$–$Cu_{30}Hf_{70}$) are flat and slowly increasing, making them attractive candidates. Films of $Cu_{42}Hf_{58}$ exhibit an almost perfect uniform stress distribution, having near zero bending force at a thickness of 800 nm.

Reducing wear in metal coatings is typically accomplished by increasing the hardness of the coating [10]. Using this design principle, it is optimal to fabricate probes from $Cu_{68}Hf_{32}$, having a nanoindentation hardness of 7.1 GPa. Although, for glassy films an increase in hardness correlates with a reduction in ductility. Therefore a high hardness tip will maintain a sharp tip during operation, but undergo catastrophic shear banding failure. Alternatively low

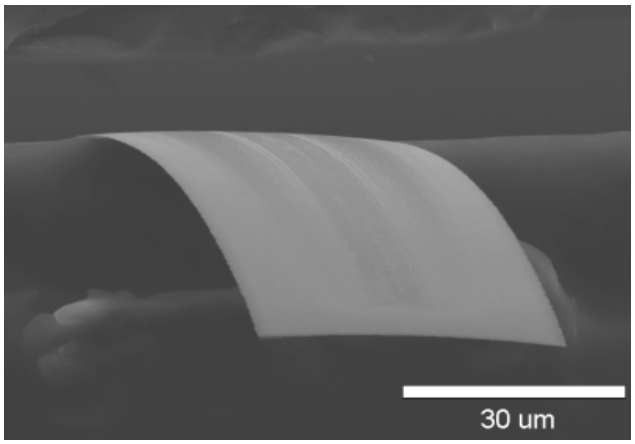

Figure 3.6: 100 µm × 50 µm × 1 µm copper cantilever. Due to internal stress gradients the cantilever exhibits significant curling upon release.

solute concentration glassy films will experience a somewhat gradual reduction in tip resolution while maintaining conductivity throughout, but will have a greatly enhanced total lifetime. From this perspective, $Cu_{90}Hf_{10}$ is an excellent compromise between hardness and ductility.

Film oxidization is also an important concern, which can degrade conductivity, mechanical properties and tip geometry. Moreover, strongly oxidizing films may have limited use in aqueous environments. To characterize film oxidation behaviour they were left in atmosphere for a period of 3 months then analyzed using EDAX. It was found that oxide content increased significantly with Hafnium concentration. The $Cu_{90}Hf_{10}$ film had the lowest oxide content of all alloy films, possessing 5 at.% oxygen concentration.

Finally we would like to maximize the conductivity of the probes, which is achieved by minimizing the solute content. Based on all of the above design constraints, it is found that $Cu_{90}Hf_{10}$ provides the best combination of internal stress gradients, hardness, ductility, oxidization, and conductivity.

3.5 Fabrication and testing of Cu–Hf AFM probes

3.5.1 Fabrication

Illustrated in figure 3.7 are the steps used for the microfabrication of $Cu_{90}Hf_{10}$ AFM probes. The fabrication procedure consists of four main steps: tip mould fabrication, film deposition and cantilever patterning, probe release, and block attachment.

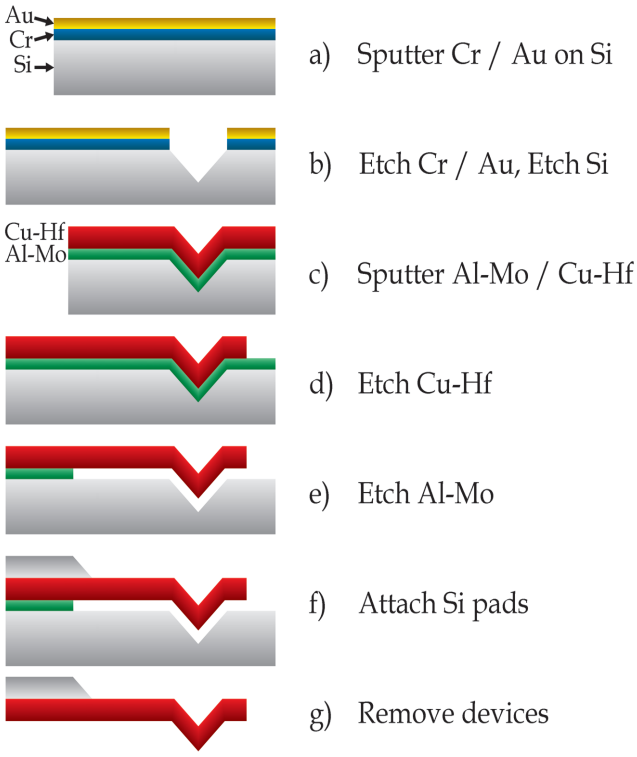

Figure 3.7: Process flow for the microfabrication of all–metal $Cu_{90}Hf_{10}$ AFM probes.

The starting point is the patterning of inverted pyramidal pits in a silicon wafer, which is to be used as mould for the probe tips. The pyramidal pits are

formed by potassium hydroxide (KOH) etching (33 wt.%, 70 °C) of exposed square areas. Prior to KOH etching, a 75 nm Au masking layer is deposited onto a ⟨001⟩ oriented Si wafer, with 15 nm Cr adhesion layer (figure 3.7(a)), followed by spin coating a 1.2 µm thick layer of positive HPR 504 resist. Using optical lithography an array of square holes are patterned in the Au masking layer figure 3.7(b)). The Au layer is etched using a mixture of 5% I_2 + 10% KI + 85%H_20 [31], and the Cr adhesion layer is etched using Cyantek CR–7 chromium etch [31].

The tip radius and subsequent spatial resolution of the AFM probes are significantly effected by knife–edging during the KOH etching procedure. During lithography the square openings used for KOH etching are oriented at 45° with respect to the wafer flat. As shown by Sarajlic et. al.[32] the knife–edge length at the tip of the pyramidal pits is minimized in this configuration. This was found to improve both tip radius and consistency across the entire wafer.

Once the tip mould has been machined, a film of $Cu_{90}Hf_{10}$ is deposited on the tip mould and patterned into cantilevers (figures 3.7 (c)–(d)). The $Cu_{90}Hf_{10}$ film is patterned using optical lithography and etched using Cyantek CR–7 chromium etch. To release the cantilevers from the substrate a sacrificial layer is deposited onto the mould prior to deposition of the $Cu_{90}Hf_{10}$ film.

Previously, we have performed a detailed investigation of aluminum–molybdenum thin films [16], [33], where it was found that small addition of Mo to Al resulted in a dramatic reduction of surface roughness. Therefore $Al_{94}Mo_6$ was chosen as a sacrificial layer, since it is rapidly etched by KOH and is much smoother than pure Al. A 200 nm thick layer of $Al_{94}Mo_6$ was found to provide both reasonable etch rates and tip radii.

Lastly, the patterned $Cu_{90}Hf_{10}$ probes are removed from the substrate with double sided adhesive tape. Small silicon blocks (1.6mm × 3.4mm) are cut by a diamond saw then bonded to the $Cu_{90}Hf_{10}$ film with the double sided adhesive tape. The $Cu_{90}Hf_{10}$ film is easily pulled off the surface due to the undercutting during the KOH etch of the $Al_{94}Mo_6$ sacrificial layer.

3.5.2 Characterization and testing of $Cu_{90}Hf_{10}$ probes

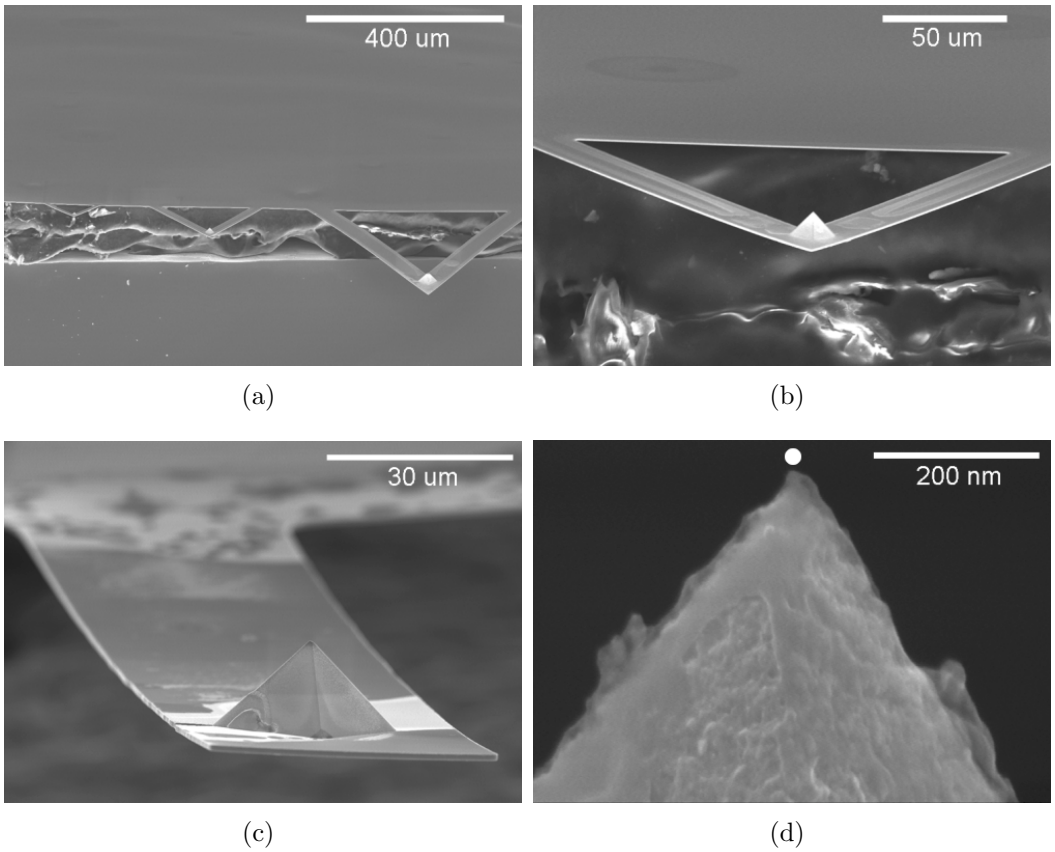

Figure 3.8: Series of SEM images characterizing the quality of 1 µm thick $Cu_{90}Hf_{10}$ AFM cantilevers and tips. (a) Set of three cantilevers with lengths of 100 µm, 200 µm, and 400 µm. The 100 µm and 200 µm long cantilevers are essentially flat, while the very long cantilever exhibits some bending. (b) Single 200 µm long cantilever. (c) 150 µm long cantilever that is slightly curved, but definitely usable in the AFM. (d) Close–up of a pyramidal tip, showing a sub 10 nm tip radius. For comparison a 10 nm radius dot is shown.

Using a Hitachi S–4800 SEM, both the quality of the tips and the amount of cantilever bending is characterized. Shown in figure 3.8 is a series of SEM images characterizing the quality of $Cu_{90}Hf_{10}$ AFM probes. In figure 3.8(a) a set of three cantilevers with lengths of 100 µm, 200 µm, and 400 µm is shown. The 100 µm and 200 µm long cantilevers are essentially flat, while the very long cantilever exhibits some bending. Zooming–in on a 200 µm long cantilever,

we see that is has zero curvature and appears to be sharp. Zooming–in even further on the apex of a tip, we see that it is quite sharp with a sub 10 nm tip radius. Of the 30 devices that were imaged, 70% appeared to be of sufficient quality to be used in an AFM. The average tip radius is estimated to be between 20 nm and 30 nm, comparing well to commercially available metal coated tips which typically have tip radii greater than 20 nm.

	E (GPa)	$\sqrt{E/\rho}$ (km/s)	k (N/m)	f_0 (kHz)
$\langle 100 \rangle$ Si	166	8.43	64	349
LPCVD Si_3N_4	143	6.81	47	282
$Cu_{90}Hf_{10}$	68	2.70	22	112

Table 3.1: Comparison of the mechanical properties of $Cu_{90}Hf_{10}$ to more common AFM materials (Si and Si_3N_4) for a cantilever 125 µm in length, 4 µm thick and 40 µm wide. Mechanical properties of Si and Si_3N_4 are those reported by Hall [34] and Albrecht et. al.[2].

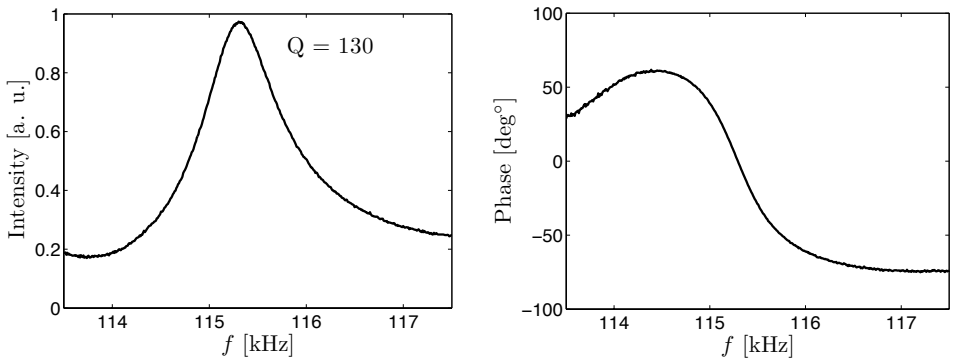

(a) (b)

Figure 3.9: Resonance characteristic of the 2nd harmonic of the 150 µm long, 1 µm thick and 50 µm wide $Cu_{90}Hf_{10}$ AFM probe used for imaging. (a) Amplitude. (b) Phase.

Shown in table 3.1 is a comparison of the mechanical properties of $Cu_{90}Hf_{10}$ to more common AFM materials (Si and Si_3N_4) for a cantilever 125 µm in length, 4 µm thick and 40 µm wide, which is a typical geometry for commercial tapping mode cantilevers. The elastic modulus of $Cu_{90}Hf_{10}$ is determined from nanoindentation and found to be $E \approx 68$ GPa. The speed of sound

$\nu_s = \sqrt{E/\rho}$, is calculated by using a rule of mixtures to estimate the density, giving a value of $\rho \approx 9.4 \times 10^3$ kg/m^3. The spring constant k, is estimated using $k = Eh^3W/4L^3$ [2], and the resonant frequency f_0, is calculated using the well known expression [35]

$$f_n = \frac{(\lambda_n)^2 h}{4\pi L^2}\sqrt{\frac{E}{3\rho}} \tag{3.5.1}$$

$$\lambda_n \approx 1.875, 4.694, 7.855, 10.996, 14.137. \tag{3.5.2}$$

The results of table 3.1 demonstrate that $Cu_{90}Hf_{10}$ cantilevers are intrinsically more compliant and possess lower resonant frequencies than those made from more common AFM materials, such as Si and Si_3N_4. As previously discussed, $Cu_{90}Hf_{10}$ cantilevers can be fabricated to arbitrary thicknesses, therefore if a specific application requires higher frequency $Cu_{90}Hf_{10}$ AFM probes, it is straightforward to achieve this by fabricating thicker cantilevers. Conversely, $Cu_{90}Hf_{10}$ AFM probes are particulary well suited to applications requiring a high force sensitivity.

As a proof of principle the fabricated $Cu_{90}Hf_{10}$ probes are mounted in a commercial AFM system (Dimension 3100 with Nanoscope IV controller, Veeco, Santa Barbara, CA), and used to image a known test structure. The test structure consisted of an array 1 µm × 1 µm squares. The AFM micrograph is acquired using a 150 µm long, 1 µm thick and 50 µm wide $Cu_{90}Hf_{10}$ probing in tapping mode operation. Using equation 3.5.2 and the constants listed in table 3.1 the resonant frequency of this cantilever is $f_0 = 19.4$ kHz. This fundamental frequency is undesirably low for tapping mode imaging, therefore imaging is performed using the 2$^{\text{nd}}$ harmonic, which has a resonant frequency of $f_1 = 121$ kHz according to equation 3.5.2. Shown in figure 3.9 is the resonance characteristic used for imaging, which has a Lorenztian amplitude response, linear phase, quality factor of 130 and center frequency of 115.3 kHz. The quality factor and center frequency are calculated by fitting the amplitude response to a Lorenztian profile.

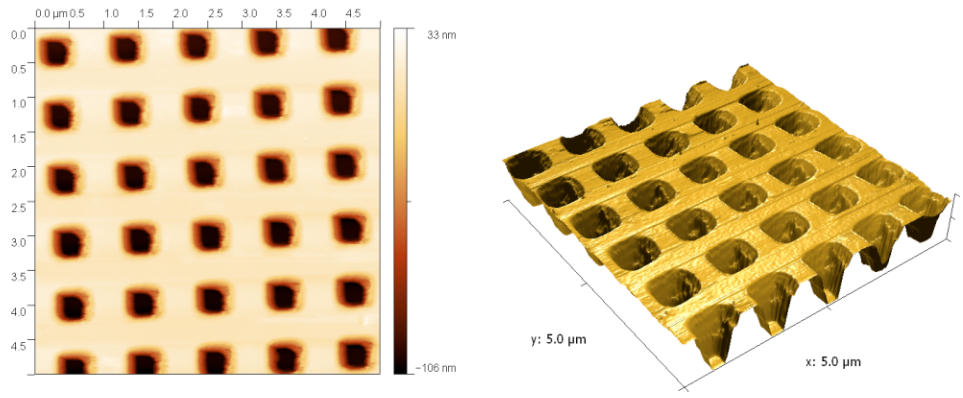

(a) (b)

Figure 3.10: AFM topograph of a known structure of 1 µm x 1 µm square pits imaged using a Cu-Hf AFM probe. (a) 2–dimensional height map (b) 3–dimensional topograph

Shown in figure 3.10 is a micrograph of the test structure acquired using the $Cu_{90}Hf_{10}$ probe. We see that the image quality is excellent, the image appears as expected reproducing the known structure. However, closer inspection of figure 3.10(b) reveals a minor imaging artifact at the edge of the holes, this is likely a result of the roughness on the tip faces, which can be seen in figure 3.8(c). The tip roughness is likely a consequence of incomplete etching of the sacrificial $Al_{94}Mo_6$ layer. By reducing the thickness of the sacrificial layer and increasing the subsequent etch time, tip uniformity is expected to improve. Although no direct study of tip wear was performed, it is noted that 6 images of the test structure were acquired with the same tip, none of which showed any noticeable signs of image degradation. Future work will focus on the wear of $Cu_{90}Hf_{10}$ probes.

3.6 Summary

Motivated by the growing demand for AFM applications requiring a conductive probe, all-metal AFM probes were investigated in this work. A detailed study of the Cu–Hf alloy system was performed in order to determine the

optimal alloy composition to be used for probe fabrication. Depositing Cu–Hf films using co–sputtering, it was found that films within the composition range of $Cu_{90}Hf_{10}$–$Cu_{30}Hf_{70}$ had a glassy microstructure. These glassy films were identified as excellent candidates for probe fabrication, as they possess high hardness and a uniform stress distribution. In order to maximize the conductivity and ductility the film with minimum solute content, $Cu_{90}Hf_{10}$, was chosen to be used for the fabrication of all–metal AFM probes.

A microfabrication process using optical lithography and chemical etching was developed for the fabrication of $Cu_{90}Hf_{10}$ AFM probes. Using this process, probes of several geometries are constructed. The cantilevers exhibit minimal curling, and tip radii are on average 20–30 nm. As a proof of principle a $Cu_{90}Hf_{10}$ probe is mounted in a commercial AFM system and was used to successfully image a known test structure.

References

[1] G. Binnig, H. Rohrer, C.H.. Gerber, and E. Weibel. Surface studies by scanning tunneling microscopy. *Phys. Rev. Lett.*, 49(1):57, 1982.

[2] T. R. Albrecht, S. Akamine, T. E. Carver, and C. F. Quate. Microfabrication of cantilever styli for the atomic force microscope. *J. Vac. Sci. Technol., A*, 8 (4):3386, 1990.

[3] S. Akamine, R. C. Barrett, and C. F. Quate. Improved atomic force microscope images using microcantilevers with sharp tips. *Appl. Phys. Lett.*, 57(3):316, 1990.

[4] D. Cavalcoli, M. Rossi, A. Tomasi, and A. Cavallini. Degeneracy and instability of nanocontacts between conductive tips and hydrogenated nanocrystalline si surfaces in conductive atomic force microscopy. *Nanotechnology*, 20(4), 2009.

[5] H. J. Mamin and D. Rugar. Thermomechanical writing with an atomic force microscope tip. *Appl. Phys. Lett.*, 61(8):1003, 1992.

[6] S. Yoshida, T. Ono, and M. Esashi. Conductive polymer patterned media fabricated by diblock copolymer lithography for scanning multiprobe data storage. *Nanotechnology*, 19(47):475302, 2008.

[7] F. Yang, E. Wornyo, K. Gall, and W. P. King. Thermomechanical formation and recovery of nanoindents in a shape memory polymer studied using a heated tip. *Scanning*, 30(2):197, 2008.

[8] O de Abril, A. Gundel, F. Maroun, P. Allongue, and R. Schuster. Single-step electrochemical nanolithography of metal thin films by localized etching with an afm tip. *Nanotechnology*, 19(32):325301, 2008.

[9] M. S. Johannes, D. G. Cole, and R. L. Clark. Three-dimensional design and

replication of silicon oxide nanostructures using an atomic force microscope. *Nanotechnology*, 18(34):345304, 2007.

[10] M. Palacio and B. Bhushan. Nanomechanical and nanotribological characterization of noble metal-coated afm tips for probe-based ferroelectric data recording. *Nanotechnology*, 19(10):105705, 2008.

[11] B. Bhushan, M. Palacio, and K. J. Kwak. Thermally-treated pt-coated silicon afm tips for wear resistance in ferroelectric data storage. *Acta Mater.*, 56(16): 4233, 2008.

[12] K. Birkelund, E. V. Thomsen, J. P. Rasmussen, O. Hansen, P. T. Tang, P. Moller, and F. Grey. New approaches to atomic force microscope lithography on silicon. *J. Vac. Sci. Technol., B*, 15(6):2912, 1997.

[13] M. Radmacher, J. P. Cleveland, and P. K. Hansma. Improvement of thermally induced bending of cantilevers used for atomic force microscopy. *Scanning*, 17: 117, 1995.

[14] J. Zou, X. F. Wang, D. Bullen, K. Ryu, C. Liu, and C. A. Mirkin. A mould-and-transfer technology for fabricating scanning probe microscopy probes. *J. Micromech. Microeng.*, 14(2):204, 2004.

[15] A. Chand, M. B. Viani, T. E. Schaffer, and P. K. Hansma. Microfabricated small metal cantilevers with silicon tip for atomic force microscopy. *J. Microelectromech. Syst.*, 9(1):112, 2000.

[16] Z. Lee, C. Ophus, L. M. Fischer, N. Nelson-Fitzpatrick, K. L. Westra, S. Evoy, V. Radmilovic, U. Dahmen, and D. Mitlin. Metallic nems components fabricated from nanocomposite al-mo films. *Nanotechnology*, 17:3063, 2006.

[17] E. Luber, R. Mohammadi, C. Ophus, Z. Lee, N. N. Fitzpatrick, K. Westra, S. Evoy, U. Dahmen, V. Radmilovic, and D. Mitlin. Tailoring the microstructure and surface morphology of metal thin films for nano-electro-mechanical systems applications. *Nanotechnology*, 19(12), 2008.

[18] G. Duan, D. H. Xu, and W. L. Johnson. High copper content bulk glass formation in bimetallic cu-hf system. *Metall. Mater. Trans. A*, 36A(2):455,

2005.

[19] W. C. Oliver and G. M. Pharr. Measurement of hardness and elastic modulus by instrumented indentation: Advances in understanding and refinements to methodology. *J. of Mater. Res.*, 19(1):3, 2004.

[20] A. L. Shull and F. Spaepen. Measurements of stress during vapor deposition of copper and silver thin films and multilayers. *J. Appl. Phys.*, 80(11):6243, 1996.

[21] W. Dmowski, T. Egami, K.E. Swider-Lyons, W. Yan, S. Dai, and S. H. Overbury. Local atomic structure in disordered and nanocrystalline catalytic materials. *Zeitschrift fur Kristallographie*, 222(11), 2007.

[22] H. W. Sheng, W. K. Luo, F. M. Alamgir, J. M. Bai, and E. Ma. Atomic Packing and Short-to-Medium-Range in Metallic Glasses. *Nature*, 439(7075):419, 2006.

[23] V. Drits, L. Srodon, and D. D. Eberl. Xrd measurement of mean crystalline thickness of illite and illite/smectite: Reappraisal of the kubler index and the scherrer equation. *Clays and Clay Miner.*, 45(3):461, 2007.

[24] A. B. Bhatia and D. E. Thornton. Structural aspects of the electrical resistivity of binary alloys. *Phys. Rev. B*, 2(8):3004, 1970.

[25] R. N. Singh and F. Sommer. Temperature-dependence of the thermodynamic functions of strongly interacting liquid alloys. *J. Phys. Condens. Matter*, 4: 5345, 1992.

[26] D. Liang and Y. Liu. Reevaluation of the cu-hf binary system. *J. Alloy Compd.*, 426(1):101, 2006.

[27] L. Zhang, Y. Q. Cheng, A. J. Cao, J. Xu, and E. Ma. Bulk metallic glasses with large plasticity: Composition design from the structural perspective. *Acta Mater.*, 57(4):1154, 2009.

[28] F. Spaepen. Interfaces and stresses in thin films. *Acta Mater.*, 48(1):31, 2000.

[29] C. V. Thompson and R. Carel. Stress and grain growth in thin films. *J. Mech. Phys. Solids*, 44(5):4657, 1996.

[30] S. D. Senturia. *Microsystem Design*. Springer+Business Media Inc., New York, NY, USA, 2001.

[31] K. R. Williams, K. Gupta, and M. Wasilisk. Etch rates for micromachining processing - part ii. *J. Micromech. Microeng.*, 12(6):761, 2003.

[32] E. Sarajlic, C. Yamahata, and H. Fujita. Towards wet anisotropic silicon etching of perfect pyramidal pits. *Microelectron. Eng.*, 84(5):1419, 2007.

[33] C. Ophus, N. N. Fitzpatrick, Z. Lee, E. Luber, C. Harrower, K. Westra, U. Dahmen, V. Radmilovic, S. Evoy, and D. Mitlin. Resonance properties and microstructure of ultracompliant metallic nanoelectromechanical systems resonators synthesized from al-32mo amorphous-nanocrystalline metallic composites. *Appl. Phys. Lett.*, 92(12), 2008.

[34] J.J. Hall. Electronic effects in the elastic constants of n-type silicon. *Phys. Rev.*, 161(3):756, 1967.

[35] R. Sandberg, W. Svendsen, K. Molhave, and A. Boisen. Temperature and pressure dependence of resonance in multi-layer microcantilevers. *Journal of Micromechanics and Microengineering*, 15(8):1454.

4

Solid–state dewetting mechanisms of ultrathin Ni films revealed by combining *in situ* time resolved differential reflectometry monitoring and atomic force microscopy *

4.1 Introduction

Many technologically important thin film/substrate systems are found to be unstable at temperatures well below their melting point, where the thin film breaks up into small islands [1–6]. This instability is know as dewetting or agglomeration, which is a result of minimizing the total system energy driven by differences in surface free energies of the film surface and the film/substrate interface.

Dewetting is a serious concern in microelectronics reliability as it is intimately linked to copper interconnect reliability [7–9]. Conversely, many applications utilize nanoparticles and nanoholes, which can be produced via solid–state dewetting, such as the fabrication of optoelectronic devices [10], subwavelength resonance focusing [11] and catalysis [12, 13]. As such, a fundamental and quantitative understanding of the mechanisms governing solid–state dewetting is of particular relevance.

*Material in this chapter has been published in:
► E. Luber, B.C. Olsen, C. Ophus and D. Mitlin. *Phys. Rev. B* **82**, 085497 (2010).

Theoretically the final morphology of the dewet state is governed by the so–called Rayleigh instability [14, 15], which leads to a characteristic particle spacing. However, the Rayleigh instability is rarely observed since the dewetting of polycrystalline films is strongly influenced by the presence of grain boundaries and grain boundary triple junctions [16]. As identified by Mullins[17] in 1957, thermal grooving is the origin of dewetting in the presence of grain boundaries. Using continuum methods, the stability of a periodic arrangement of identical grains was analyzed by Srolovitz and Safran[18] in 1986 , this was expanded upon by Rha and Park [19] in 1997. Recently, Pierre–Louis *et al* have employed Kinetic Monte Carlo simulations to elucidate the important role of faceting during dewetting [20]. However, a firm theoretical understanding of solid–state dewetting has been slow due to the complex and varied nature of a real arrangement of grains composing a film.

In recent years a few authors have made use of *in situ* and realtime techniques, which have expanded our understanding solid–state dewetting. The van der Pauw method has been used to monitor realtime changes in electrical resistance of Cu films on SiO_2 during *ex situ* heating [4]. Other authors have performed *in situ* electrical monitoring of dewetting Ni films [21]. Electrical monitoring provides quantitative kinetic information, however it cannot probe the significant morphological changes that occur beyond the percolation limit (electrical breakdown). Moreover, to avoid compositional changes during *in situ* four–point probe resistance measurements, the voltage and current leads must be fabricated from the same material as the film under investigation [21], which severely limits the class of materials that can be investigated in this way. Alternatively, *in situ* grazing incidence small angle x-ray scattering (GISAXS) has been utilized to probe morphological changes that occur during dewetting [1, 22] of Ni films. However, even when using synchrotron radiation GISAXS is only quasi–realtime with acquisition times on the order of $\sim$ 40 sec. Another limitation is the size of particles that can be studied [23] and does not provide quantitative kinetic information. Moreover, a complete morphological interpretation is fundamentally limited to model based inversion.

In this study we utilized *in situ* time resolved differential reflectometry (TRDR) coupled with atomic force microscopy (AFM) to investigate dewetting kinetics and morphological changes of Ni films on amorphous SiO_2. Dewetting of Ni films on SiO_2 is important for new flash memory technologies [24], growth of carbon nanotubes [12, 13, 25], and potential nanomagnetic properties [26]. TRDR is simple to implement, non-destructive, and can be used to probe dewetting of virtually any sample type. From these measurements we identify four sequential stages of dewetting Ni films on SiO_2 and measure activation energies of two kinetically limiting processes. Moreover, the observed optical response is understood via three–dimensional finite–difference time–domain (FDTD) simulation, using acquired AFM height maps as simulation inputs.

4.2 Methods

4.2.1 Experimental

The substrates used in this study were (100) oriented silicon wafers that were thermally oxidized in a wet environment using a custom built furnace (Tystar Inc.). Prior to oxidation, the Si wafers were cleaned using a 3:1 mixture of H_2SO_4:H_2O_2. The oxide thickness was grown to 124 and 365 nm, which was measured using a F50 spectral reflectance automated thickness mapper (Filmetrics Inc.) and subsequently cleaved into 1 cm $\times$ 1 cm chips, keeping only chips having SiO_2 thicknesses within ± 1 nm of each other. These chips were stored in a vacuum chamber at base pressures of $\sim 1 \times 10^{-7}$ Torr.

Ni films with thicknesses between 2.0 to 9.0 nm were deposited at a constant rate of 0.62 Å/sec using a DC magnetron sputtering system (AJA International) at UHV conditions (base pressure $< 9 \times 10^{-10}$ Torr). Argon sputtering was maintained at 4 mTorr and 100 W. Deposition rates were determined using a quartz crystal deposition monitor. Interfacial mixing during deposition is expected to negligible during deposition. As shown by Qiu *et al*[27], us-

ing both reflection high energy electron diffraction and transmission electron microscopy, there is no interfacial mixing that occurs during DC magnetron sputtering of Ni on SiO_2. Moreover, the equilibrium phase diagram shows that Ni and SiO_2 have negligible mutual solubility at all temperatures considered in this study.

Prior to deposition each chip was annealed in the UHV chamber at 500 °C for 2 hours and allowed to cool for $>$ 12 hours. Following deposition the films were vacuum heated at the desired ramp rate to 500 °C and held for 2 hours at this temperature. The temperature was measured using a thermocouple and was estimated to have an error of less than ±5 °C at temperatures above 150 °C.

During all stages of UHV chip proccessing (pre–deposition anneal, deposition and post–deposition heating) the optical reflectivity was monitored. TRDR is performed using a 660 nm s–polarized AlGaInP diode laser operating at 16 mW. The beam is incident upon the films 30 ° from the substrate normal. The specular beam intensity was measured using a ILT 1700 light meter (International Light Technology) using a silicon detector. The incident and reflected beam traveled through the vacuum chamber via transparent silica windows. The parameter of interest is the change in reflectivity R, with respect to the initial substrate reflectivity R_0 prior to deposition

$$\frac{\Delta R}{R} = \frac{R - R_0}{R_0} \tag{4.2.1}$$

The film morphologies were analyzed using a Multimode AFM (Veeco Instruments Inc.) operating in tapping mode. Films having large features were scanned with ACTA tips (AppNano) having a nominal tip radius of 6 nm using a E–type piezo element which allowed for 10 µm of horizontal scanning. Films having smaller features were scanned with ACTA–SS tips (AppNano) having a nominal tip radius of 2 nm using a A–type piezo element which allowed for 1 µm of horizontal scanning.

Film texture was analyzed using X–ray diffraction (XRD), which was performed using a Bruker AXS D8 Discover diffractometer with a GADDS area detector used. A Cu Kα radiation source ($\lambda = 1.54056$ Å) collected the x-ray scans from a sample mounted on a two-axis rotation stage that also allowed for XYZ translation.

4.2.2 Simulation

The optical changes of the films that occur during dewetting were analyzed using FDTD simulation. The FDTD calculations were performed using commercially available software from Lumerical Solutions Inc. For all simulations, experimentally acquired AFM heightmaps were used as inputs to correctly represent the morphology of the films. Shown in Fig. 4.1 is a representative schematic of the simulation geometry. Bloch boundary conditions were used in the x and y directions while perfectly matched layer was used in the z direction. A non-uniform mesh was used in z, whose spacing was determined by the index of the material. A uniform mesh spacing was used in the x and y directions, which was set to the resolution of the AFM heightmap (all AFM height maps were acquired at a resolution of 512×512 pixels^2, therefore the grid spacing used for a 2×2 µm^2 simulation volume was 3.9 nm). Within the Ni layer, a much finer mesh spacing of 0.25 nm was used in the z direction.

Broadband simulations were performed at normal incidence using a planewave source having a spectral range of 400 nm – 1400 nm. Dispersion within the Ni was modeled using an 8^{th} order polynomial fit to the experimentally determined dielectric constants in the Lumerical database. Simulations at a non–normal incidence of $\theta = 30\,^\circ$ were performed using a monochromatic s–polarized planewave source at 660 nm. Simulations were stopped when the electrical field dropped below a critical cutoff within the simulation volume.

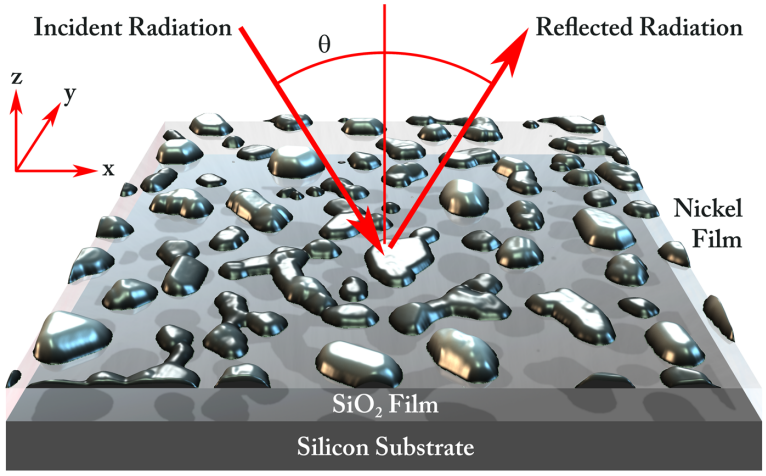

Figure 4.1: Geometry used for FDTD calculations of dewet Ni films on SiO_2.

4.3 TRDR characterization of dewetting

Figure 4.2 shows the TRDR response of Ni films (initial thicknesses ranging from 2.0 nm – 9.0 nm) on 124 nm of SiO_2, heated from room temperature to 500 °C at 5 °C/min, which was then held at 500 °C for 2 hours. We see that the TRDR response exhibits a rich behaviour, showing significant variation in both temperature (time) and initial film thickness. Importantly, all films within this thickness range exhibit a minimum in reflectivity (aside from the thinest film of 2.0 nm). The TRDR curve of a blank substrate was also measured, having negligible changes during heating. Given that the variation in TRDR response is intimately tied to changes in the Ni film, a detailed investigation of the relation between TRDR response and morphology was performed.

The TRDR signal during the deposition of a 7.0 nm thick Ni film on 365 nm of SiO_2 is shown in Fig. 4.3(a). Also shown is the theoretical TRDR signal, calculated using the characteristic matrix approach [28], which assumes the Ni layer is perfectly flat, uniform and utilizes bulk Ni optical constants. Both curves have the same characteristic behaviour where the initial addition of a the metal layer results in a *decrease* in reflectivity. However, the minimum reflectivity is experimentally determined to be at 4.0 nm of Ni, whereas the

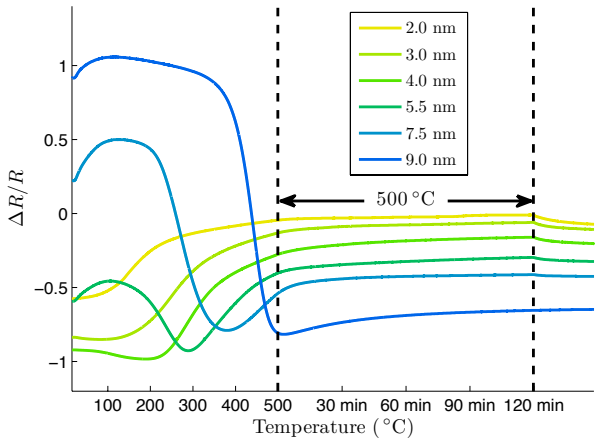

Figure 4.2: TRDR response of Ni films (initial thicknesses ranging from 2 nm – 9 nm) on 365 nm of SiO_2, ramped at 5 °C/min, which is then held at 500 °C for 2 hours.

characteristic matrix method predicts the minimum reflectivity to occur at a thickness of 1.9 nm. This important discrepancy is a result of the well established fact that inhomogeneities in the film (grain boundaries, voids, etc.) significantly affect optical properties in the visible–UV range [29].

The initial decrease of the TRDR signal during deposition illustrates the significance of a changing interference condition as the properties of the Ni film change. Simple two–beam interference is a useful conceptual tool for understanding many of the observed optical changes. Prior to the deposition of Ni, the SiO_2/Si stack is near a destructive interference condition for incident radiation at 660 nm and $\theta = 30\,°$, due to a half integer path length difference between the primary and secondary reflected beams. However, the amplitude of the primary beam is small in comparison to the secondary beam due to the low reflectivity of the vacuum/SiO_2 interface. The deposition of the Ni layer results in both an increase in the amplitude of the primary beam and a decrease in the amplitude of the secondary beam. As the amplitudes of the primary and secondary beams approach each other the destructive interference becomes more complete, which is the physical origin of the TRDR signal observed during deposition. This situation is much more complex dur-

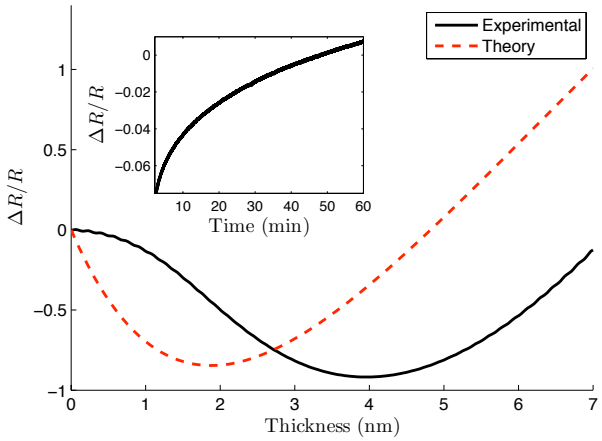

(a)

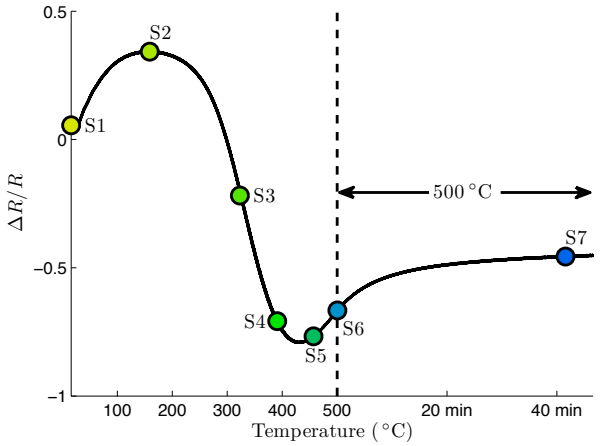

(b)

Figure 4.3: (a) Experimental and theoretical TRDR signals during the deposition of a 7.0 nm thick Ni film on 365 nm of SiO_2. Inset is the change in reflectivity after the deposition is stopped. (b) TRDR signal of a 7.0 nm film during heating at 10 °C/min. Points labeled S1–S7 indicate separate films that were prepared under identical conditions which were heated to the shown temperature then cooled back to room temperature. The respective AFM micrographs are shown in Fig. 4.4.

ing dewetting, nonetheless a changing interference condition due to changes in the Ni film topography is expected to significantly affect the TRDR signal.

Shown in Fig. 4.3(b) is the TRDR signal of a 7.0 nm Ni film during heating. The points labeled S1–S7 indicate separate films that were prepared under identical conditions which were heated to the shown temperature then cooled back to room temperature. The respective AFM micrographs are shown in Fig. 4.4. After an initial increase in reflectivity (this will be discussed in more detail later) there is a rapid and significant decrease in reflectivity. Inspection of micrographs S3–S4 reveal that this decrease in reflectivity is associated with the nucleation and growth of holes in the Ni film, exposing the bare SiO_2 interface. Eventually the reflectivity reaches a minimum, when the film is near the percolation limit (sample S5), followed by a much slower increase in reflectivity, where the film is completely broken up and consists entirely in isolated Ni particles (micrograph S7).

The most common methods used to interpret electromagnetic reflection data of discontinuous metal films are effective medium theories, such as the Maxwell–Garnett and Lorentz–Lorenz theories [30]. However, these methods are limited by the validity of the assumptions used and simplified geometry [31]. Importantly, these theories are not strictly valid near the percolation limit, nor do they provide significant physical insight beyond extracting some mean physical parameters within the framework of the theory. Therefore, to gain a more detailed understanding of the TRDR response during all stages of dewetting, FDTD simulations were performed. The experimentally measured AFM heightmaps of samples S3–S7 were utilized to directly set the film geometry in the simulation.

4.3.1 FDTD Simulation

In order to investigate transmission through a dewetting Ni layer, FDTD simulations of Ni films on a SiO_2 substrate were performed. Inset in Fig. 4.5(a) is the calculated spectral transmission at normal incidence of samples S3–S7. As

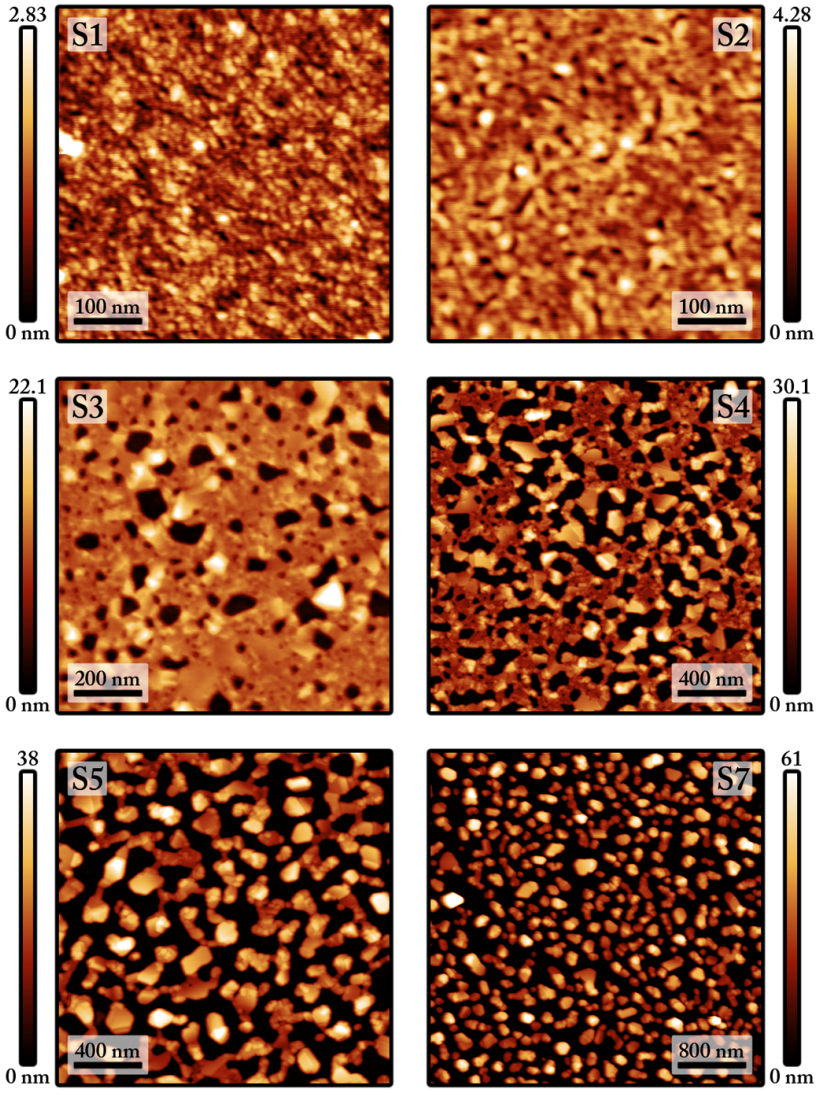

Figure 4.4: *Ex situ* AFM micrographs of a 7.0 nm thick Ni film during different stages of dewetting. The corresponding film temperature and reflectivity are shown in Fig. 4.3(b).

expected, transmission through the Ni layer increases as the dewetting process proceeds since more of the SiO_2 surface is being exposed to vacuum. However, the increase in transmission is much greater in the near–infrared than the visible portion of the spectrum. This indicates that the change in transmission is not simply in proportion to the area fraction of uncovered substrate.

When studying transmission through optically thick metal hole arrays, it is useful to normalize the transmission spectrum such that it can be interpreted as the effective transmission of the holes in the array [32]. The normalized transmission, or transmissivity η, is given by

$$\eta = \frac{T}{QT_{\text{sub}}} \tag{4.3.1}$$

where T is the measured transmission, Q is the area fraction of uncovered substrate and T_{sub} is the transmittance of the substrate. Using this normalization scheme, a transmissivity greater than unity indicates some extraordinary transmission, while a transmissivity less than unity indicates some energy loss as the radiation interacts with the aperture(s). However, we must generalize this definition due to the complication that the films used in this study are on the order of the skin depth, resulting in non–zero transmission through the Ni. The transmissivity is then redefined in the following manner

$$\eta(\lambda) = \frac{T(\lambda)}{\frac{1}{N}\sum_{i=1}^{N} T_i(\lambda)} \tag{4.3.2}$$

Where the average is taken over the field of illumination, divided into N locally homogeneous sub–domains. The transmission of each sub–domain is T_i, which is calculated using the characteristic matrix approach. We see that this definition reduces to equation 4.3.1 when the transmission through the metal layer is zero.

The transmissivity of samples S3–S7 are shown in Fig. 4.5(a). We see that transmissivity is generally increasing with wavelength for all samples, with S3 and S4 exhibiting transmissivities greater than unity. Enhanced transmis-

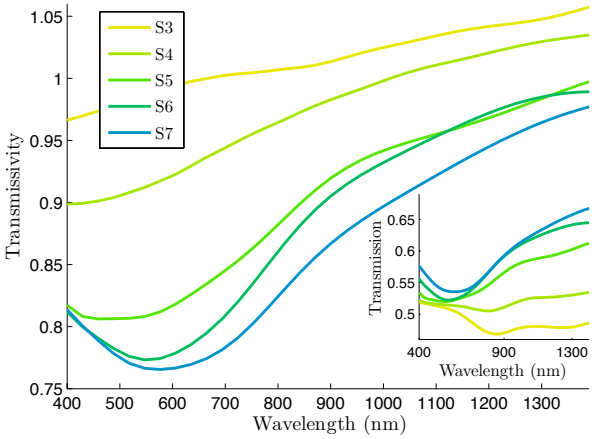

(a)

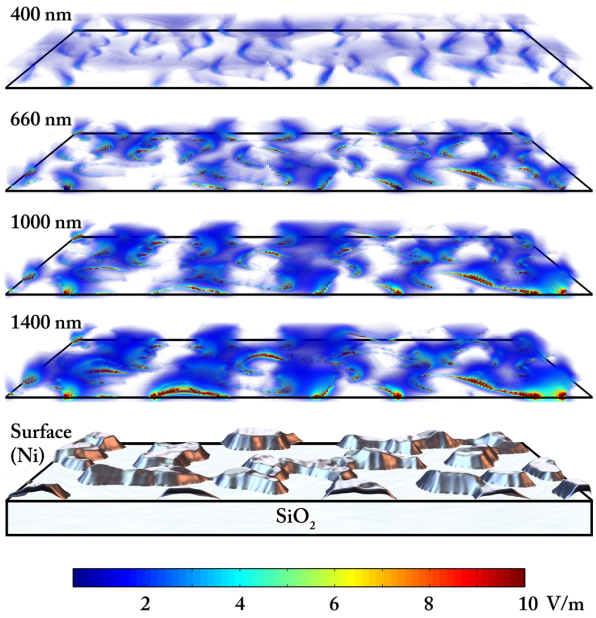

(b)

Figure 4.5: (a) FDTD calculation of the normalized spectral transmissivity (inset: un–normalized transmission) at normal incidence of samples S3–S7 on SiO_2 substrate during different stages of dewetting. (b) Steady state electric field intensity in a 1 µm × 1 µm region of sample S5 at incident wavelengths of 400 nm, 660 nm, 1000 nm and 1400 nm.

sion of subwavelength uncorrelated–random hole arrays has been observed for several different metals [32], where the enhanced transmission was attributed to so–called site resonances or localized surface plasmon resonance. More recently, detailed investigation on the role of site resonances in enhanced transmission for wavelength scale square holes has been investigated both theoretically [33] and experimentally [34]. It was found that the enhanced transmission was both spectrally broad and weak, with the peak transmission occurring at a wavelength roughly double the hole size.

Site resonances are a consequence of the oscillating radiation producing a force on the mobile electrons in the conduction band, the result of which is to induce a dipole moment in the particle/hole. Figure 4.5(b) shows the steady state electric filed intensity in a 1 µm × 1 µm region of sample S5 at incident wavelengths of 400 nm, 660 nm, 1000 nm and 1400 nm. We see the associated induced dipole fields at the edges of the particles due to site resonances, which become more intense at longer wavelengths. The observed increase in transmissivity with wavelength is a consequence of these increasingly intense site resonances. Moreover, the decrease in transmissivity as dewetting proceeds is likely a result of scattering from the wavelength scale particles/holes [35].

From these simulations we see that the total transmission increases significantly as dewetting proceeds. Investigation of the steady state electric field shows the presence of site resonances, however their contribution to transmission is small since the transmissivity is never much greater than unity. This is consistent with the transmission spectra of uncorrelated–random hole arrays [34]. Therefore, we find that the changes in transmission during dewetting are largely driven by ordinary transmission through the oxide and sub–skin depth Ni, and scattering from the Ni particles/holes.

From the above results it is not entirely clear why the TRDR signal exhibits a minima during dewetting, as seen in Fig. 4.3(b). The FDTD simulations show that the transmission increases monotonically as dewetting proceeds; therefore, from the perspective of two–beam interference it is expected that the reflectivity decrease monotonically, since the initial amplitude of primary

beam is larger than the secondary, and as dewetting proceeds these amplitudes approach each other. To understand this observed behaviour we performed FDTD simulations of samples S3–S7 replicating the experimental configuration (365 nm SiO_2 on a Si substrate with radiation of 660 nm incident at 30°).

The simulated TRDR signal is shown in Fig. 4.6(a). It agrees well with experiment, having the same characteristic behaviour. However, it should be noted that the absolute values of reflectivity are different from that in experiment, which is likely a consequence of the difference in dielectric constants between thin film and bulk [29]. Nonetheless, this result demonstrates that the shape of the TRDR curve can be understood within the set of assumptions used in the FDTD simulations. Shown in Fig. 4.6(b) is the temporal evolution of the average electric field intensity in a plane above the Ni surface, corresponding to the simulations in Fig. 4.6(a). This clearly shows both the primary reflection from the vacuum/Ni interface and the secondary reflection from the SiO_2/Si interface. As expected, the amplitude of the primary pulse continually decreases during dewetting, while the amplitude of the secondary pulse continually increases. As the ratio of the primary and secondary amplitudes approach unity, the destructive interference becomes more complete and the reflectivity is expected to decrease. However, close inspection of Fig. 4.6(a) shows that the arrival times of both pulses are changing during dewetting.

The time delay between the arrival of the primary and secondary pulses (which is simply taken to be the time difference between the peak amplitudes of each pulse) is inset in Fig. 4.6(b). We see that the time delay between pulse arrivals (or phase difference) reaches a maximum for sample S5. This is a manifestation of the effective Ni layer becoming more 'dielectric–like' than metallic, with respect to transmission. During the initial stages of dewetting very little SiO_2 is exposed, and the majority of the transmitted radiation travels through Ni regions. Since the average height of the Ni regions is increasing, the radiation takes longer to travel to the SiO_2/Si interface, due to the slower group velocity in the Ni regions. This results in a increase in the time delay between the primary and secondary pulse. However, as the dewetting process continues the

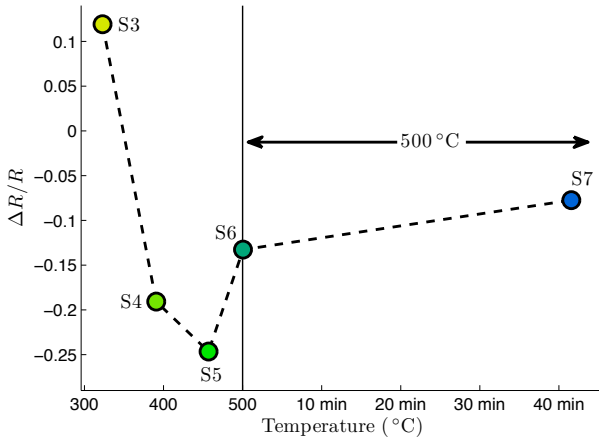

(a)

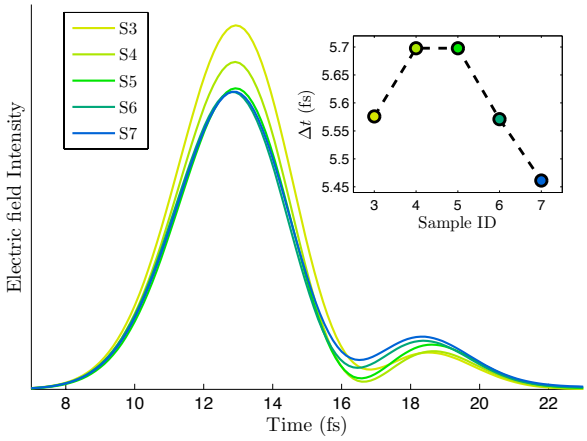

(b)

Figure 4.6: (a) FDTD simulation of TRDR signal during dewetting of 7 nm Ni film on 365 nm SiO_2 having a Si substrate with radiation of 660 nm incident at 30°. The simulations are performed using AFM heightmaps S3–S7. (b) Temporal evolution of the average electric field intensity in a plane above the Ni surface. Inset is the time delay between the peak amplitudes of the primary and secondary reflections.

amount of exposed SiO_2 continues to increase along with the average height of the Ni regions. Between samples S4 and S5 a critical amount of exposed SiO_2 is reached, where the majority of the transmitted radiation emerges from the SiO_2/vacuum interface (this is compounded by the fact that the average height of the Ni regions is becoming thicker and transmitting less radiation). This reduces the time delay between pulses, which causes the reflectivity to increase due to the change in interference condition. Inspection of Fig. 4.6(b) reveals that samples S4 and S5 have identical time delays but S5 has a lower reflectivity. This is explained by noting that the ratio of amplitudes between the primary and secondary beams of S5 is closer to unity than that of S4, resulting in more complete destructive interference. Likewise, S3 and S6 have identical time delays, but their differing amplitude ratios of the primary and secondary pulse produces different reflectances.

The connection between the TRDR signal and the morphology during dewetting has been more clearly elucidated from the FDTD simulations. It was found that transmission increased monotonically during dewetting, which was largely mediated by ordinary transmission through both the exposed SiO_2 and sub–skin depth regions of Ni. As dewetting proceeds the amount of exposed SiO_2 increases and the amount of sub–skin depth Ni regions decrease. This is seen as a decrease in measured reflectivity due to the more complete destructive interference as the ratio of amplitudes between the primary and secondary beams becomes closer to unity. However, as the dewetting continues a critical amount of exposed SiO_2 is reached where transmission through the effective Ni layer becomes more 'dielectric–like' than metallic, resulting in a reduction in the time delay between the primary and secondary reflected pulses. This is seen as an increase in the measured reflectivity, and the origin of the minimum observed in the TRDR signal. The minimum of the TRDR signal is expected to occur at different amounts of exposed SiO_2 for Ni films of different initial thicknesses, since the transition of the effective Ni layer from metallic to dielectric is clearly dependent on the initial Ni film thickness. Moreover, the minimum of the TRDR signal during dewetting of Ni films thinner than 7.0 nm should occur at smaller amounts of exposed SiO_2, since the initial ratio

of amplitudes between primary and secondary beams will be much closer to unity.

4.4 Dewetting Mechanisms

By analyzing the sequence of AFM micrographs S1–S7 in Fig. 4.4 in conjunction with the TRDR data, we can more rigorously understand the mechanisms of the dewetting process. Comparing micrographs S1 and S2 we clearly observe both grain growth and a high density of grain boundary grooves. Most grooves have a longish geometry with aspect ratios greater than unity, since they extend along the planar grain boundary/vacuum interface. As explained by Mullins [17], grain boundary grooving is mediated by surface diffusion and is a result of the interface evolving towards a constant curvature surface, constrained by an equilibrium dihedral angle at the grain boundary. Grain boundary grooving has previously been observed in Ni films of comparable thickness [21] and is generally accepted as the primary mechanism of hole nucleation in solid state dewetting [36]. Conversely, the effect of grain growth prior to the dewetting process has remained largely unexplored.

The average in–plane grain diameters of micrographs S1 and S2 are calculated using a watershed grain detection algorithm, which are found to be 14 ± 2 nm and 20 ± 2 nm respectively. Since the initial grain size is on the order of the film thickness normal grain growth is expected to stagnate [37], which is often attributed to the formation of grain boundary grooves pinning the grain boundaries [38]. It must be emphasized that grain growth is not stopped but it is simply slower than normal grain growth; moreover, it has been found [39] that grain growth of ultrathin columnar films is accelerated by the surface energy driving force, which scales strongly with the inverse film thickness [40].

The grain growth observed in AFM is further supported by the TRDR data. Inspection of the TRDR signal in Fig. 4.2 reveals that the reflectivity increases during the initial stages of heating (for films of initial thickness greater than

4.0 nm), which was found to be irreversible upon cooling. As previously mentioned, the optical constants of thin films are different than bulk samples due to inhomogeneities such as grain boundaries and vacancies. As seen in Fig. 4.3(a) the reflectivity of the 7.0 nm thick film is less than that predicted by the bulk optical constants. Therefore, an increase in grain size is consistent with the observed increase in reflectivity during the initial stages of heating, since the conductivity is expected to increase with grain size [41, 42] for nanoscale grains. Consequently, the optical constant of the film will approach that of the bulk values. Moreover, this effect was even detected at room temperature, as shown in Fig. 4.3(a) where the reflectivity is found to increase non-asyptotically after deposition.

From these data it is not necessarily clear if grain growth is the dominant mechanism responsible for the change in reflectivity. The annealing of other defects such as non–equilibrium vacancies and argon inclusions would produce similar effects [21]. However, this ambiguity is resolved by measuring the post-deposition TRDR signal of a discontinuous film at room temperature. The room temperature post–deposition measurement of reflectivity of the 2.0 nm thick film was constant found to be constant in time (within the resolution of the photodetector). This was distinctly different than all other films, which exhibited significant changes in reflectivity. It is emphasized that no detectable change in reflectivity was observed in the 2.0 nm sample, which was recorded for 2 hours. Conversely, all other films showed measurable post–deposition changes in reflectivity at room temperature within the first minute, and continued to change monotonically for all time scales measured (up to 13 hours). From four–point probe resistance measurements, it was found that the 2.0 nm as–deposited film was discontinuous, while films possessing thicknesses of 3.0 nm and greater were all found to be continuous. This sharp transition in the post–deposition changes in reflectivity cannot be explained by annealing of vacancies or argon inclusions, since these processes will occur independent of the film continuity [43]. Therefore it can be concluded that the post–deposition change in reflectivity is a result of grain growth.

Inspection of micrograph S3 reveals large holes exposing the SiO_2, which are nucleated when the grain boundary grooves reach the substrate. There is a wide distribution in hole size, which indicates that both hole growth and nucleation occur simultaneously. Hole growth and nucleation continues to expose greater amounts of the SiO_2 interface (micrograph S4) resulting in a further decrease in reflectivity. Eventually the percolation limit is reached (micrograph S5) where particles are connected by thin necks. Continued heating results in the necks pinching off (or particle coalescence), followed by complete break up of the film into isolated particles (micrograph S7). After the film break–up, we see that the reflectivity continues to increase, which is a result of the isolated particles coarsening via Ostwald ripening or Smoluchowski ripening [44].

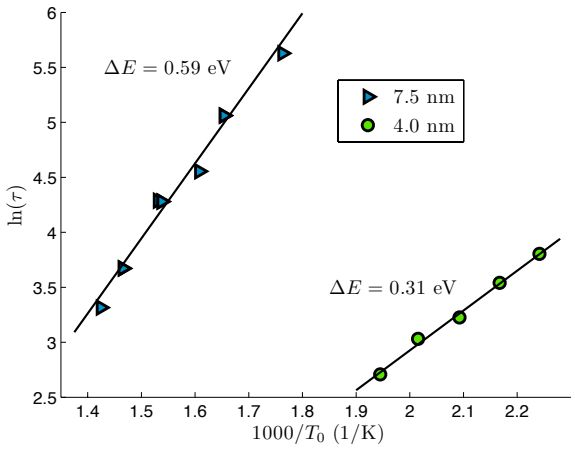

Figure 4.7: Arrhenius plots for the thermally activated processes characterized by the temperature T_0 corresponding to the minimum of the TRDR curve. Films of 4.0 nm and 7.5 nm thickness are used, and heating rates range from 1.0 °C/min to 15.0 °C/min

The kinetics of these dewetting mechanisms can be analyzed *quantitatively* using the measured TRDR signal acquired during dewetting. Given that these mechanisms are thermally activated, the time τ, to reach a characteristic temperature T_0, is given by

$$\tau = A \exp\left(\frac{\Delta E}{k_b T_0}\right) \tag{4.4.1}$$

where A is a proportionality constant, ΔE is the activation energy and k_b is the Boltzmann constant. The minimum of the TRDR curve represents a repeatable and identifiable system state, with characteristic temperature T_0. Since this characteristic temperature is dependent on the applied heat rate, we can apply equation refarrhen to determine the activation energy. Using the measured τ–T_0 pairs for heating rates ranging from 1.0 °C/min to 15.0 °C/min, and fitting to equation 4.4.1, activation energies of 0.31±0.04 eV and 0.59±0.06 eV are determined. Also, nearly identical activation energies of 0.33 ± 0.04 eV and 0.58 ± 0.06 eV were found when applying the Kissinger–Akahira–Sunose method, which is the more common method for determining activation energies of thermally activated processes during dewetting[4, 21, 45, 46].

To better understand the physical origin of these activation energies we first compare the morphologies of the 4.0 nm and 7.5 nm thick films at the minimum of the TRDR curve. As discussed in the previous section, for films of different initial thicknesses it is expected that the minimum of the TRDR signal will occur at different stages of the dewetting process. Comparing the AFM micrographs of A1 (Fig. 4.8) to S5 (Fig. 4.4) we see that this is indeed the case, as the morphologies are significantly different. A1 is in the early stages of dewetting where grain growth and grain boundary grooving are the prominent mechanisms of morphological evolution. Grain boundary grooving is unlikely to be the rate limiting step, as the we would expect the activation barrier to be at least high as that found for surface mass diffusion along the low index planes of Ni. Ondrejcek *et al*[47] have measured an activation barrier of 0.65 eV for surface mass diffusion on the (111) planes of Ni, while Bonzel and Latta[48] found a value of 0.76 eV on the (110) planes. This strongly suggests that the measured activation energy of 0.31 eV corresponds to the rate–limiting process during grain growth in 4.0 nm thick Ni films on SiO_2 at temperatures of $\sim$ 500 K.

By direct measurement of grain size in SEM, an activation energy of 0.25 eV was measured during annealing of Ni thin films [49]. The 4.0 nm thick Ni films were deposited using e–beam evaporation onto a mica substrate, and were

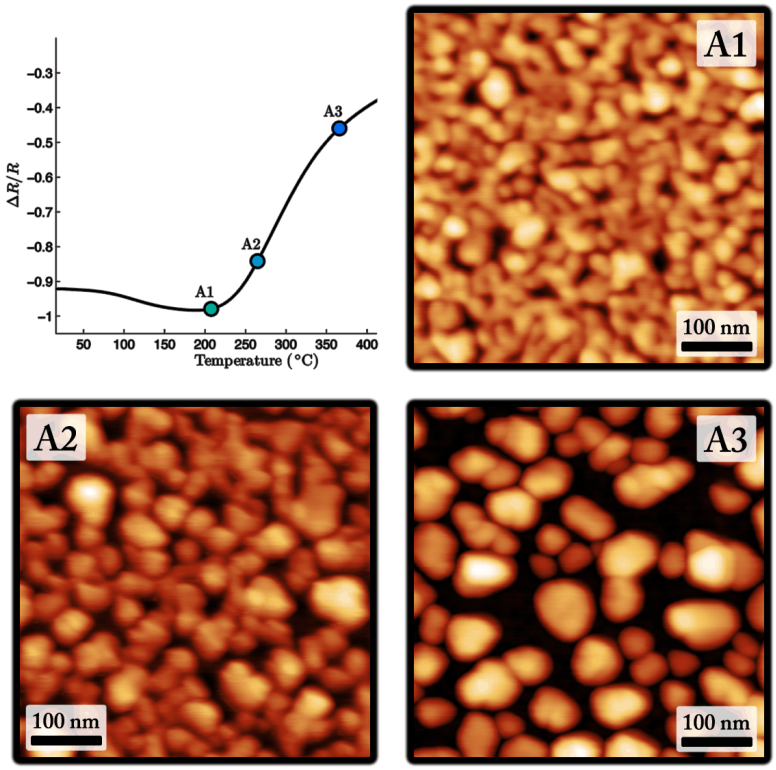

Figure 4.8: *Ex situ* AFM micrographs of a 4.0 nm thick Ni films during different stages of dewetting. The corresponding positions on the TRDR curve are shown.

annealed at temperatures ranging from 90 °C – 420 °C. This agrees well with our measured value of 0.31 eV, where the 0.06 eV difference is possibly due to the different substrate and deposition method used in this study. Also, as already discussed in significant detail, both the TRDR and AFM data strongly suggest that grain growth occurs during the initial stages of dewetting. We therefore propose that the measured activation energy of 0.31 eV corresponds to the rate–limiting mechanism of Ni grain growth at $\sim$ 500 K. Other reports on grain growth in FCC metal films performed at these temperatures also find similar activation energies.

From TEM measurements of grain size, the measured activation energy during grain growth in Au thin films was found to be 0.14 eV [50], 0.36 eV for thin films of Cu [51] and 0.274 eV for thin films of Ag [52]. These reported activation barriers for grain growth are typically attributed to the additional driving force provided by interface [53] and surface energy minimization [40] for thin films. It has also been suggested that the high density of defects, such as dislocations and twins contribute significantly to the driving force[51, 54].

Next we turn our attention to the measured activation energy of 0.59 ± 0.06 eV. Inspection of micrographs S3–S5 (Fig. 4.4) reveals that hole growth is the dominant mechanism of film break–up during this stage of dewetting. During hole growth the film locally thins via retraction of the hole edge, consequently there must be local film thickening within the interior region of the film. This suggests that the activation energy of 0.59 eV corresponds to either the rate–limiting process during local film thinning, mass transport across the Ni surface, or local film thickening.

The local thickening effect can be seen in micrographs S3–S5, where large faceted particles are observed. It is also found that the number of faceted particles increases as dewetting proceeds, as does the average particle size and height. Using KMC simulations, Combe *et al*[55] have investigated the mechanism of shape change for isolated, defect–free, faceted nanoparticles. It was found that the rate limiting step to particle relaxation was the nucleation of 2D islands on the facets. As estimated by Mullins and Rohrer[56], the nucleation

rate of 2D islands is negligible for particles $\gtrsim$ 1.0 nm. This extremely large nucleation barrier has also been confirmed by other authors[57, 58], where the nucleation barrier is generally found to be proportional to the particle size.

However, recent investigations into faceted nanoparticle agglomeration have revealed a much richer and complex behaviour than single particle shape change[59–61] . In these studies, it has been found that the coalescence rate is strongly influenced by the particle orientation. Specifically, McCarthy and Brown have shown that 2D nucleation is not required for a pair of coalescing FCC particles intersecting at the (111) plane. This is because step–flow growth of the (111) layers is possible on these favorably oriented particles, making a continuous stepped morphology across the neck region. Moreover, the activation barrier to coalescence was found to be independent of size for (111) oriented particles, and the rate–limiting step was due to surface mass diffusion.

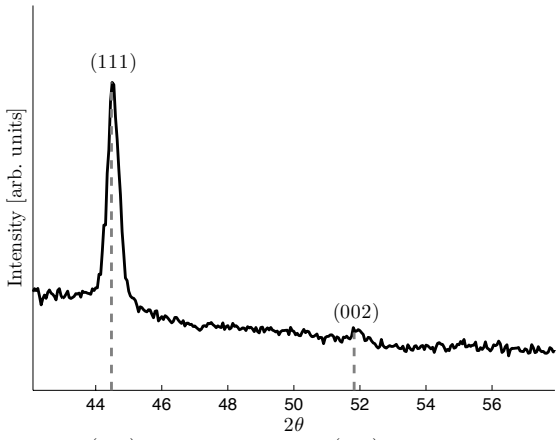

Figure 4.9: XRD scan of 7.5 nm thick Ni film during dewetting (sample S4, see Fig. 4.4). This shows that the Ni films are heavily (111) textured during this stage of dewetting.

Despite the idealized scenario of faceted particle coalescence, we expect the mechanism of local film thickening during latter stages of dewetting to occur in a similar manner. Specifically, local thickening proceeds by surface diffusion on the Ni surface, where favorably oriented faceted grains are able to coalesce via

a heterogenous nucleation mechanism. In this scenario, the rate–limiting step is surface diffusion along the planes of favorably oriented coalescing grains. From XRD data (Fig. 4.9) we see that the Ni films are strongly (111) oriented during dewetting. This strong (111) texture is a result of preferential orientation during deposition[62] and grain reconfiguration during annealing [63]. Therefore, we expect that the local thickening of the Ni films during dewetting is limited by surface diffusion along the (111) planes.

Likewise, Ni surface diffusion is also expected to be the mechanism of local film thinning. Inspections of micrographs S3–S5 shows that most holes in the film are not completely bounded by facets. Therefore, the classical mechanism of hole–edge retraction is expected to be valid in these regions[36]. Due to the larger curvature at the hole boundary, the driving force for local film thinning is provided by curvature induced surface diffusion.

Therefore, we find that the processes of local film thickening, mass transport across the Ni surface, and local film thinning are all limited by surface self diffusion along the Ni(111) planes. Recently, the activation energy for surface mass self diffusion on the Ni(111) surface was measured to be 0.65 ± 0.1 eV[47], which agrees very well with our measured activation energy of 0.59 ± 0.06 eV. In light of the above discussion, this strongly suggests that the rate–limiting step during the later stages of dewetting Ni is surface self diffusion along the (111) planes.

From the kinetic analysis we have measured activation energies of 0.31 ± 0.04 eV and 0.59 ± 0.06 eV, which are found to correspond to grain growth and hole growth via surface mass self–diffusion along the Ni(111) planes. It should be noted that these activation energies were measured from films of different thicknesses. Looking at the sequential dewetting AFM micrographs of both the 7.0 nm film (Fig. 4.4) and the 4.0 nm film (Fig. 4.8) the processes of grain growth and hole growth can both be clearly identified. It is therefore expected that both of these processes will occur as rate–limiting steps in this thickness regime. However, at higher film thicknesses, a (001) texture can often be found in FCC metal films[40]. This may significantly impact the process of

hole growth, due to the importance of grain orientation on the local thickening film. Likewise, at extremely small thicknesses, the density of grain boundary grooves may be sufficiently high such that Ni surface diffusion on the SiO_2 substrate becomes rate–limiting during hole growth. Further investigation is required to understand what the rate–limiting mechanisms are outside of the studied thickness regime.

4.5 Conclusions

We studied the dewetting of 2.0 nm – 9.0 nm thick Ni thin films on amorphous SiO_2 using TRDR, which is a real–time technique and was performed *in situ*. This was combined with *ex situ* AFM. FDTD simulations, which used the experimentally acquired AFM heightmaps as inputs, were used to better understand the observed TDRD signal and its connection to morphological changes during dewetting. FDTD simulations revealed a monotonic increase in transmission during the dewetting process and the existence of hole/particle site resonances. The site resonances become increasingly intense with wavelength, resulting in weak extraordinary transmission in some cases. However, it was found that transmission is dominated by ordinary transmission through the SiO_2 and sub–skin depth regions of Ni, and the scattering from the Ni particles/holes. Furthermore, FDTD simulation revealed that the observed minimum of the TRDR signal during dewetting is a consequence of a transmission through the effective Ni layer becoming more 'dielectric–like' than metallic. During this transition the ratio of amplitudes between the primary and secondary pulses approach unity, while the trend in time delay between pulses reverses. This extremum in time delay between pulses is the origin of the minimum observed in the TRDR signal.

Analysis of the the *ex situ* AFM micrographs revealed the sequential processes of grain growth, grain boundary grooving, hole growth and particle coarsening. The presence of grain growth was further substantiated by the TRDR data; after deposition, all continuous films ($\geq$ 3.0 nm) exhibited a non-asymptotic

monotonic change in reflectivity. Conversely, the discontinuous 2.0 nm film did not show any detectable changes in reflectivity post–deposition. The dewetting literature has typically neglected grain growth in ultrathin films prior to hole nucleation. However, grain growth is particularly important since the final particle density is critically determined by the initial grain boundary density.

Lastly, the TRDR data was used to identify two kinetic pathways during dewetting of Ni on SiO_2. These kinetic pathways were found to have activation energies of 0.31 ± 0.04 eV and 0.59 ± 0.06 eV. From these data we proposed that the physical origin of these activation energies are a result of Ni grain growth, and surface mass self–diffusion on Ni(111) respectively. The measurement of two distinct rate limiting steps during the dewetting of Ni thin films are reported in this work for the first time.

References

[1] C. Boragno, F. Buatier de Mongeot, R. Felici, and I. K. Robinson. Critical thickness for the agglomeration of thin metal films. *Phys. Rev. B*, 79(15): 155443, 2009.

[2] K. Thürmer, E. D. Williams, and J. E. Reutt-Robey. Dewetting dynamics of ultrathin silver films on si(111). *Phys. Rev. B*, 68(15):155423, 2003.

[3] Bin Yang, Pengpeng Zhang, D. E. Savage, M. G. Lagally, Guang-Hong Lu, Minghuang Huang, and Feng Liu. Self-organization of semiconductor nanocrystals by selective surface faceting. *Phys. Rev. B*, 72(23):235413, 2005.

[4] R. Saxena, M. J. Frederick, G. Ramanath, W. N. Gill, and J. L. Plawsky. Kinetics of voiding and agglomeration of copper nanolayers on silica. *Phys. Rev. B*, 72(11):115425, 2005.

[5] Y.J. Oh, C.A. Ross, Y.S. Jung, Y. Wang, and C.V. Thompson. Cobalt Nanoparticle Arrays made by Templated Solid-State Dewetting. *Small*, 5(7):860.

[6] D. Kim, A.L. Giermann, and C.V. Thompson. Solid-state dewetting of patterned thin films. *App. Phys. Lett.*, 95(25):251903, Dec 2009.

[7] F. Fillot, Z. Tőkei, and GP Beyer. Surface diffusion of copper on tantalum substrates by Ostwald ripening. *Surface Science*, 601(4):986, 2007.

[8] I. Lazić, P. Klaver, and B. Thijsse. Microstructure of a cu film grown on bcc ta (100) by large-scale molecular-dynamics simulations. *Phys. Rev. B*, 81(4): 045410, 2010.

[9] A. Hashibon, A. Y. Lozovoi, Y. Mishin, C. Elsässer, and P. Gumbsch. Interatomic potential for the cu-ta system and its application to surface wetting and dewetting. *Phys. Rev. B*, 77(9):094131, 2008.

[10] S. H. Lim, D. Derkacs, and E. T. Yu. Light scattering into silicon-on-insulator waveguide modes by random and periodic gold nanodot arrays. *J. Appl. Phys.*, 105(7):3101, 2009.

[11] M. A. Seo, H. R. Park, S. M. Koo, D. J. Park, J. H. Kang, O. K. Suwal, S. S. Choi, P. C. M. Planken, G. S. Park, N. K. Park, et al. Terahertz field enhancement by a metallic nano slit operating beyond the skin-depth limit. *Nat. Photonics*, 3:152, 2009.

[12] G.D. Nessim, A.J. Hart, J.S. Kim, D. Acquaviva, J. Oh, C.D. Morgan, M. Seita, J.S. Leib, and C.V. Thompson. Tuning of Vertically-Aligned Carbon Nanotube Diameter and Areal Density through Catalyst Pre-Treatment. *Nano Lett.*, 8 (11):3587, 2008.

[13] G.D. Nessim, M. Seita, K.P. OBrien, A.J. Hart, R.K. Bonaparte, R.R. Mitchell, and C.V. Thompson. Low Temperature Synthesis of Vertically Aligned Carbon Nanotubes with Electrical Contact to Metallic Substrates Enabled by Thermal Decomposition of the Carbon Feedstock. *Nano Lett.*, 9(9):3137, 2009.

[14] L. Rayleigh. On the stability of liquid jets. *Proc. London Math. Soc*, 10(4), 1878.

[15] M.E.T. Molares, A. G. Balogh, T. W. Cornelius, R. Neumann, and C. Trautmann. Fragmentation of nanowires driven by Rayleigh instability. *Appl. Phys. Lett.*, 85(22).

[16] A. E. B. Presland, G. L. Price, and D. L. Trimm. The role of microstructure and surface energy in hole growth and island formation in thin silver films. *Surf. Sci.*, 29(2):435.

[17] W. W. Mullins. Theory of thermal grooving. *J. Appl. Phys.*, 28(3):333, 1957.

[18] D. J. Srolovitz and S. A. Safran. Capillary instabilities in thin films. I. Energetics. *J. Appl. Phys.*, 60(1):247, 1986.

[19] J. J. Rha and J. K. Park. Stability of the grain configurations of thin filmsA model for agglomeration. *J. Appl. Phys.*, 82(4):1608.

[20] O. Pierre-Louis, A. Chame, and Y. Saito. Dewetting of ultrathin solid films. *Phys. Rev. Lett.*, 103(19):195501, 2009.

[21] J. Petersen and S. G. Mayr. Dewetting of Ni and NiAg solid thin films and formation of nanowires on ripple patterned substrates. *J. Appl. Phys.*, 103(2): 023520.

[22] R. Felici, N. M. Jeutter, V. Mussi, F.B. de Mongeot, C. Boragno, U. Valbusa, A. Toma, Y.W. Zhang, C. Rau, and I. K. Robinson. In situ study of the dewetting behavior of Ni-films on oxidized Si (001) by GISAXS. *Surf. Sci.*, 601 (18):4526.

[23] R. Lazzari, G. Renaud, C. Revenant, J. Jupille, and Y. Borensztein. Adhesion of growing nanoparticles at a glance: Surface differential reflectivity spectroscopy and grazing incidence small angle x-ray scattering. *Phys. Rev. B*, 79(12):125428.

[24] J. Dufourcq, P. Mur, M. J. Gordon, S. Minoret, R. Coppard, and T. Baron. Metallic nano-crystals for flash memories. *Mater. Sci. Eng. C*, 27(5):1496.

[25] A. Romo-Negreira, D.J. Cott, S. De Gendt, K. Maex, M.M. Heyns, and P.M. Vereecken. Electrochemical Tailoring of Catalyst Nanoparticles for CNT Spatial-Dimension Control. *J. Electrochem. Soc.*, 157(3):K47.

[26] Y.T. Jeon, J.Y. Moon, G.H. Lee, J. Park, and Y. Chang. Comparison of the magnetic properties of metastable hexagonal close-packed Ni nanoparticles with those of the stable face-centered cubic Ni nanoparticles. *J. Phys. Chem. B*, 110 (3):1187.

[27] H. Qiu, G. Safran, B. Pecz, P.B. Barna, A. Kosuge, H. Nakai, S. Yugo, and M. Hashimoto. Structural and electrical properties of Ni films grown on Si (100) and SiO2 by dc bias sputtering. *Thin Solid Films*, 229(1):107, 1993.

[28] S. Larouche and L. Martinu. OpenFilters: open-source software for the design, optimization, and synthesis of optical filters. *Appl. Opt.*, 47(13):219, 2008.

[29] D. E. Aspnes. Optical properties of thin films. *Thin Solid Films*, 89(3):249.

[30] M. Gilliot, A. En Naciri, L. Johann, J. P. Stoquert, J. J. Grob, and D. Muller.

Optical anisotropy of shaped oriented cobalt nanoparticles by generalized spectroscopic ellipsometry. *Phys. Rev. B*, 76(4):045424.

[31] R. Lazzari and I. Simonsen. A software for calculating thin-layer dielectric properties and Fresnel coefficients. *Thin Solid Films*, 419(1):124, 2002.

[32] K. L. van der Molen, K. J. Klein Koerkamp, S. Enoch, F. B. Segerink, N. F. van Hulst, and L. Kuipers. Role of shape and localized resonances in extraordinary transmission through periodic arrays of subwavelength holes: Experiment and theory. *Phys. Rev. B*, 72(4):045421, 2005.

[33] A.F.J. García, J. J. Sáenz, I. Campillo, and J. S. Dolado. Site and lattice resonances in metallic hole arrays. *Opt. Express*, 14(1):7, 2006.

[34] T. Matsui, A. Agrawal, A. Nahata, and Z.V. Vardeny. Transmission resonances through aperiodic arrays of subwavelength apertures. *Nature*, 446(7135):517, 2007.

[35] M. Born and E. Wolf. *Principles of Optics, 7$^{\text{th}}$edition.* Cambridge, 1999.

[36] E. Jiran and C.V. Thompson. Capillary instabilities in thin, continuous films. *Thin Solid Films*, 208(1):23, 1992.

[37] C. V. Thompson. Grain growth in thin films. *Annu. Rev. of Mater. Sci.*, 20 (1):245, 1990.

[38] W. W. Mullins. The effect of thermal grooving on grain boundary motion. *Acta Met.*, 6(6):414, 1958.

[39] R. A. Ristau, K. Barmak, K. R. Coffey, and J. K. Howard. Grain growth in ultrathin films of CoPt and FePt. *J. Mater. Res*, 14(8), 1999.

[40] C. V. Thompson. Grain Growth in Polycrystalline Thin Films of Semiconductors. *Interface Sci.*, 6(1):8, 1998.

[41] J.M. Camacho and A. I. Oliva. Surface and grain boundary contributions in the electrical resistivity of metallic nanofilms. *Thin Solid Films*, 515(4):1881, 2006.

[42] A. F. Mayadas and M. Shatzkes. Electrical-resistivity model for polycrystalline films: the case of arbitrary reflection at external surfaces. *Phys. Rev B.*, 1(4): 1382, 1970.

[43] Z. Zhou and B. Jóos. Vacancy annealing kinetics in finite monolayer patches. *Surf. Sci.*, 323(3), 1995.

[44] P.A. Thiel, M. Shen, D.J. Liu, and JW Evans. Coarsening of Two-Dimensional Nanoclusters on Metal Surfaces. *J. Phys. Chem. C*, 113(13):5047, 2009.

[45] M. J. Starink. The determination of activation energy from linear heating rate experiments: a comparison of the accuracy of isoconversion methods. *Thermochim. Acta*, 404(1):163.

[46] M.J. Frederick, R. Goswami, and G. Ramanath. Sequence of Mg segregation, grain growth, and interfacial MgO formation in Cu–Mg alloy films on SiO during vacuum annealing. *J. of Appl. Phys.*, 93:5966, 2003.

[47] M. Ondrejcek, M. Rajappan, W. Swiech, and C. P. Flynn. Step fluctuation studies of surface diffusion and step stiffness for the Ni (111) surface. *Phys. Rev. B*, 73(3):35418, 2006.

[48] H. P. Bonzel and E. E. Latta. Surface self-diffusion on Ni (110): Temperature dependence and directional anisotropy. *Surf. Sci.*, 76(2):275, 1978.

[49] V. Starı and K. Sefcik. Electrical resistivity and structure of thin nickel films–effect of annealing. *Vacuum*, 31(8-9):345, 1981.

[50] N. Mancini and E. Rimini. Annealing of polycrystalline Au and Au-Ag thin films. *Surf. Scie.*, 22(2):357, 1970.

[51] S. Simões, R. Calinas, M. T. Vieira, M. F. Vieira, and P. J. Ferreira. In situ TEM study of grain growth in nanocrystalline copper thin films. *Nanotechnology*, 21(14):145701, 2010.

[52] R. Dannenberg, E. A. Stach, J.R. Groza, and B.J. Dresser. In-situ TEM observations of abnormal grain growth, coarsening, and substrate de-wetting in nanocrystalline Ag thin films. *Thin Solid Films*, 370(1):54, 2000.

[53] E.A. Holm and S.M. Foiles. How Grain Growth Stops: A Mechanism for Grain-Growth Stagnation in Pure Materials. *Science*, 328(5982):1138, 2010.

[54] C. Detavernier, S. Rossnagel, C. Noyan, S. Guha, C. Cabral Jr, and C. Lavoie. Thermodynamics and kinetics of room-temperature microstructural evolution in copper films. *J. of Appl. Phys.*, 94:2874, 2003.

[55] N. Combe, P. Jensen, and A. Pimpinelli. Changing shapes in the nanoworld. *Phys. Rev. Lett.*, 85(1):110, 2000.

[56] W. W. Mullins and G. R. Rhorer. Nucleation barrier for volume-coarsening shape change of faceted ctystals. *J. Am. Ceram. Soc.*, 83(1):214, 2000.

[57] A. La Magna. Nanoisland shape relaxation mechanism. *Surf. Sci.*, 601(2):308, 2007.

[58] K. Thurmer and N.C. Bartelt. Nucleation-Limited Dewetting of Ice Films on Pt (111). *Phys. Rev. Lett.*, 100(18):186101, 2008.

[59] J. Rankin and B.W. Sheldon. Surface roughening and unstable neck formation in faceted particles: I, Experimental results and mechanisms. *J. Am. Ceram. Soc.*, 82(7):1868, 1999.

[60] L.J. Lewis, P. Jensen, and J.L. Barrat. Melting, freezing, and coalescence of gold nanoclusters. *Phys. Rev. B.*, 56(4):2248, 1997.

[61] D.N. McCarthy and S.A. Brown. Evolution of neck radius and relaxation of coalescing nanoparticles. *Phys. Rev. B.*, 80(6):64107, 2009.

[62] Y. Golan, L. Margulis, and I. Rubinstein. Vacuum-deposited gold films:: I. Factors affecting the film morphology. *Surf. Sci.*, 264(3):312, 1992.

[63] M. J. Rost, D. A. Quist, and J. W. M. Frenken. Grains, growth, and grooving. *Phys. Rev. Lett.*, 91(2):26101, 2003.

5 Conclusions

5.1 Thesis Summary

In this thesis the use of thin metal films in NEMS/MEMS was investigated. Chapters 2 and 3 were focused on optimizing materials properties for specific NEMS/MEMS applications, through microstructural design. Chapter 4 studied the phenomenon of solid-state dewetting of Ni thin films of SiO_2.

In chapter 2 the microstructure and subsequent material/mechanical properties of metallic nanoscale cantilevers were tailored by co-sputtering Ni-Mo thin films at different compositions. Films were sputtered in roughly 10 at.% intervals and were characterized using XRD, TEM, SEM, AFM, nanoindentation and resistivity measurements. It was found that films with compositions ranging from Ni-34 at.%Mo to Ni-69 at.% had an amorphous -nanocrystalline microstruture. Films within this composition range possessed a unique combination of mechanical and material properties, having hardnesses of $\sim$ 10 GPa, resistivity of $\sim$ 100 µΩcm and $\sim$ 1 nm RMS roughness. The origin of roughness in these amorphous surfaces was understood through modelling using a Langevin-type stochastic rate equation. It was found that a growth instability develops as a result of the competition between surface diffusion and self-shadowing. Due to the higher thermal energies of sputtering, surface diffusion is dominant, explaining the exceptionally smooth films. Lastly, NEMS cantilevers fabricated from amorphous nanocrystalline Ni-44 at.% Mo were fabricated. These uncurled 50 nm thick and 2-6 µm had MHz resonant

frequencies and quality factors ranging from 200-900.

In chapter 3 all-metal AFM probes were fabricated from Cu-Hf thin films. Again, in order to determine the optimal composition from probe fabrication. a detailed characterization procedure of XRD, nanoindentation, resistivity and *in situ* stress measurements were performed. In order to predict the amount of bending a released cantilever would exhibit, a continuum model was developed, with utilized *in situ* stress measurements as inputs. From these characterization and modelling results, $Cu_{90}Hf_{10}$ was identified as the optimal candidate for probe fabrication. Next a microfabrication procedure was developed for AFM probe fabrication, which utilized tip moulding, lithographic definition, sacrificial etching and final transfer and bonding to a Si block. The cantilevers were found to possess minimal bending, with average tip radii of 20–30 nm. Lastly as a proof of principle, AFM probes fabricated from $Cu_{90}Hf_{10}$ were mounted in a commercial AFM used to successfully image a known test structure.

In chapter 4 the fundamental mechanisms of solid-state dewetting of thin Ni films on SiO_2 was investigated. The dewetting processes was monitored *in situ* in a UHV environment using time resolved differential reflectometry. The connection between the TRDR signal and morphological changes were interpreted within the framework of FDTD simulations, where AFM heightmaps were used as inputs. It was found that transmission increases monotonically during dewetting, while extraordinary transmission due to site resonances was negligible. From the FDTD it was found that the minimum in the TRDR signal represents the transition of the thin Ni film from metallic to dielectriclike. From AFM characterization the sequential processes of grain growth, thermal grooving, hole growth and particle coarsening were observed. The processes of grain growth is further substantiated by the post-deposition TRDR data, which is of critical importance, because the final particle density of the dewet film is critically determined by the pre-dewet grain boundary density. Lastly, from the TRDR data, two kinetic pathways during dewetting of Ni on SiO_2 are identified. These mehcanisms have activation energies of 0.31 ± 0.04 and 0.59 ± 0.06 eV, which are proposed to correspond to Ni grain growth and

surface mass self-diffusion on Ni(111), respectively.